Second Law Analysis of a Liquid Cooled Battery Thermal Management System for Hybrid and Electric Vehicles

By

Lokendra Ramotar

A Thesis Submitted in Partial Fulfillment

of the Requirements of the Degree of

Master of Applied Science in Automotive Engineering

Faculty of Engineering and Applied Science

University of Ontario Institute of Technology

August 2010

ACKNOWLEDGEMENTS

This thesis would not have been possible if it were not for my supervisor, Dr. Greg Naterer. He gave me the unique opportunity to complete my degree in a field that I am passionate about. His knowledge and kindness are second to none and I could not have asked for a better supervisor or experience while at UOIT. I will be forever grateful.

I am also grateful to Dr. Greg Rohrauer, who gave me a chance to be part of the UOIT EcoCAR team, where I learned what it takes to build electric vehicles. He is the most knowledgeable professor I have ever met working in the automotive field.

To my family who supported me along the way, there is no price you can put on encouragement.

To my friends, old ones and those I made along the way while at UOIT, your friendship and support I will never forget.

Financial support of this research from the Canada Research Chairs program is gratefully acknowledged.

ABSTRACT

As hybrid and electric vehicles continue to evolve there is a need for better battery thermal management systems (BTMS), which maintain uniformity of operating temperature of the batteries in the vehicles. This thesis investigates the use of an indirect liquid cooled system, which can be applied to hybrid and electric vehicles. The design is modeled as part of the UOIT EcoCAR. The predominant focus of this indirect liquid cooled system is the entropy generation in each of the components within the system, as well as a total system analysis. Four main components of the system are the battery module, heat exchanger, pump, and throttle. The battery module coolant tubes and the entire heat exchanger model are developed. Various parameters are changed in each component, leading to a decrease in entropy generation depending on the variable changed. Of the four components identified, the heat exchanger produced the majority of entropy generation, which leads to an overall increase in system entropy generation. There are many factors to consider when designing a liquid cooled BTMS. The new model shows a unique ability to improve system performance by reducing the entropy generation in the BTMS.

Keywords: Entropy, Second law, Heat transfer, Electric vehicle, Battery

TABLE OF CONTENTS

LIST OF TABLES

LIST OF FIGURES

NOMENCLATURE

A	Total heat transfer surface area for the heat exchanger (m^2)
A_0	Free flow area on one side of the heat exchanger (m^2)
$A_{c,core}$	Cross-sectional area of core (m)
$A_{c,tube}$	Cross-sectional area of tube (m)
A_{fr}	Frontal area of heat exchanger (m^2)
a_{e-t}	Battery edge to tube distance (m)
C	Heat capacity rate (J/Ks)
C_p	Specific heat (kJ/kgK)
$D_{h,core}$	Hydraulic diameter of core
D_{tube}	Diameter of tube (m)
f	Friction factor
g	gravitational acceleration (m/s^2)
G	Core mass velocity (kg/m^2s)
h	Heat transfer coefficient (W/m^2K)
H_{mic}	Microhardness (Pa)
H_p	Horsepower of the pump (HP)
H_{rad}	Height of heat exchanger (m)

j	Colburn factor
K_b	Loss coefficient through a bend
L_{batt}	Length of the battery (m)
L_{curve}	Length of curve in tubing (m)
L_{fin}	Total length of individual fin (m)
$L_{fin,side}$	Length of one side of fin (m)
L_{str}	Length of tube straight section (m)
$L_{tube,layer}$	Total length of tubing on one battery layer (m)
$L_{tube,total}$	Total length of tubing for entire battery module (m)
$\dot{m}$	Mass flow rate (kg/s)
m	Fin parameter (m^{-1})
N_{curve}	Number of curved sections on cooling layer
N_s	Non-dimensional entropy generation number
N_{space}	Number of spaces between tubing straight sections
N_t	Number of cores
Nu	Nusselt number
N_{tubes}	Number of tubing straight sections
P_{bm}	Pressure for the battery module (Pa)
Pw_p	Power of the pump (W)

Pw_e	Electrical power of the pump (W)
Q	Heat generation (W)
Q_p	Flow rate of the pump (GPM)
r_{cur}	Radius of curve for tubing (m)
Re	Reynolds number
$r_{h,core}$	Hydraulic radius of core (m)
S	Entropy (J/K)
$\dot{S}_{gen}$	Entropy generation rate (J/Ks)
s_r	Combined rms surface roughness (m)
s_s	combined mean absolute surface slope (–)
T	Temperature (K)
U	Overall heat transfer coefficient (W/m^2K)
U_{core}	Perimeter of core (m)
V	Velocity (m/s)
W_{batt}	Width of the battery (m)
W_{rad}	Width of heat exchanger
X_{c-c}	Tube centre-to-centre spacing (m)
X_{des}	Exergy destruction
X_l	Longitudinal spacing of cores (m)

X_t	Transverse spacing of cores (m)
$X_{w\text{-}w}$	Tube wall-to-wall spacing (m)

Greek Letters

α	Surface area density (m^2/m^3)
δ	Cell separation distance (m)
Δ	Difference
ε	Effectiveness of the heat exchanger
η	Fin efficiency
η_p	Pump efficiency
ρ	Density (kg/m^3)
ν	Kinematic viscosity (m^2/s)
π	Pi (3.14159)
μ	Dynamic viscosity (kg/ms)
σ	Ratio of free flow area to frontal area

Superscripts

*	Dimensionless ratio

Subscripts

a	air
f	fluid
in	inlet
out	outlet

Acronyms

BTMS	Battery thermal management system
ECS	Environmental control system
EV	Electric vehicle
EREV	Electric range extended vehicle
HEV	Hybrid electric vehicle
ICE	Internal combustion engine
NTU	Number of heat transfer units
ZEV	Zero emission vehicle

CHAPTER 1 - INTRODUCTION

1.1 Overview

The world relies heavily on fossil fuels to meet its power demands, from electricity production to the many types of transportation. The fuel used in the majority of vehicles is a product of oil, which accounts for approximately 34.4% of the world's total energy consumption [1]. The burning of petroleum based fuels over the past few decades has led to a growing number of problems for the planet, most noticeably the effects on air quality around the world, and global warming. Burning of fossil fuels contributes to the release of harmful gases, such as carbon monoxide (CO), carbon dioxide (CO_2), sulfur oxides (SOx) and nitrous oxides (NOx) into the atmosphere, which have an adverse impact on human health. The Environmental Protection Agency (EPA) has shown that air pollution can lead to adverse health effects such as respiratory problems, nervous system complications, cancer, and premature death [2].

Global warming is the result of accumulated greenhouse gases in the atmosphere, which raises the Earth's overall temperature. The effects of global warming are observed through the melting of the polar ice caps, rising sea level, and different seasonal climate compared to previous years. The main way to reduce the effects of global warming would be to decrease the amount of fossil fuels used.

A related problem is a depletion of oil reserves, which leads to "Peak Oil", where consumption outruns the rate of reserves new oil discovery. Peak Oil has the potential to create a severe liquid fuel problem for the transportation industry [3], amidst a higher demand for fuels which increases fuel prices [3]. Due to global climate change and potential oil shortages, world organizations and leaders are

coming together to create a plan on how to cope with these issues. The transportation arena is a key industry in these discussions. This has led to an increased focus on conservation of energy and "green" technologies in the automotive and transportation fields.

Lowering the emissions from automobiles, and increasing vehicular fuel efficiency, are some of the ways the automotive industry can reduce the harmful impact on air quality and oil consumption. Technology advancement rate for the internal combustion engine (ICE) may have peaked, but there is no other propulsion system available at this time to completely replace the ICE. A new system needs to be designed that not only is more efficient than the ICE, but must also meet or exceed the capabilities of the current ICE. There are alternative propulsion systems being developed, namely electric vehicles (EV) and fuel cell vehicles (FCV), which are generating more interest due to the demand for greener technology. Hybrid electric vehicles (HEV) have already been on the market for a number of years. They have been proven to get better fuel economy than a conventional ICE, however, there is still much room for improvement in HEVs. The knowledge gained from HEVs can also lead to better EV designs.

At this time, EVs are further along in the development stage than fuel cells, with some vehicles ready to be released to the public. EVs have the potential to slowly replace the ICE over time, or until more advanced technology and infrastructure are developed for fuel cell vehicles. In order for EVs to be accepted in the consumer market, the vehicle must offer the same capabilities and performance as conventional vehicles, while proving to be a reliable mode of transportation. With new technology, reliability cannot be measured in one to two years; it must be proven over many years. This means that before EVs are released to the market, more

investment in research and development must be made to ensure that these vehicles operate as designed. Otherwise, negative public acceptance could keep the technology from required growth. As with all new technology there will be a learning process for EVs, which improves on the initial design over time, and engineering research will advance the technology. Creating new vehicles that break the conventional mould must have proper design methodology in place. This ensures development for the next generation vehicles which builds upon the successes, and learns from the failures and shortcomings of the past.

1.2 Background

In the automotive market, there is currently no system that can completely replace the ICE. There is ongoing development of hybrid electric and full electric systems that are available to the public, however, the volume of vehicles produced is not high compared to conventional engines. There are advantages and disadvantages to each system, which will be explained in further detail later. When designing either of these systems, an analysis of the entropy generation can help identify areas of a system that should be improved, which in turn can lead to a more efficient system. The benefits of analyzing entropy generation will also be discussed later in this chapter.

1.2.1 Hybrid Vehicles

Hybrid vehicles are not entirely new, but in the past few years, they have generated increasing interest due to the green technology shift. Hybrids are typically called Hybrid Electric Vehicles (HEVs) because of their vehicle architecture. They operate with an electric motor and battery module, which helps to increase the fuel economy

[3] in addition to the ICE in the vehicle [4]. With the addition of the electric motor, the ICE is able to operate more efficiently. At lower speeds and loads, the vehicle is actually powered by electricity from the battery cells, rather than the ICE [4]. The battery module is comprised of many individual batteries which are not the typical lead acid variety used to start up ICEs. Batteries commonly used in current HEVs are either nickel metal hydride (NiMH) or lithium ion (LiIon). When the vehicle is driving, the ICE is typically used to propel the wheels when the battery power is not enough, or it turns a generator to recharge the battery [4]. The battery is also charged through a process called regenerative braking. Instead of loosing energy through the braking system in the form of heat, the kinetic energy is used by the electrical motor/generator to recharge the battery module.

Comparing HEVs and convention vehicles in the small car segment, typically fewer fill-ups are required and the ICE in the HEVs operates more efficiently overall. The average fuel economy for small HEVs is around 50 miles per gallon (MPG) or 4.7 L/100km of fuel [4]; about 35% efficiency compared to conventional vehicles. This also provides about six times the range of fully electric vehicles available in the market [4]. In terms of emissions, HEVs emit fewer tailpipe pollutants, mainly due to their electric powertrains and efficient ICEs. In conventional vehicles, ICEs are designed to generate maximum power requirements (i.e., climbing high grades or acceleration). HEVs on the other hand, use smaller engines which are lighter, cleaner and designed for efficient operation, while meeting average power needs; since the batteries provide the extra power when needed [4].

The United States Department of Energy states [4]: “So far, five-year maintenance costs for HEVs have been lower than those for conventional vehicles. A

great deal of progress has been made in improving the batteries so they will last for a vehicle lifetime of 150,000 miles or more. The main disadvantage of HEVs is their purchase price. To be commercially viable, hybrids should make up for their extra upfront cost in fuel savings over three years; manufacturers are working toward this goal. Quite a few HEVs are on the market today: Toyota, Honda, Nissan, Ford, General Motors offer small, mid-size, and sport utility vehicle (SUV) models. Some buses and trucks combine diesel and electric technologies." Table 1.1 shows some additional advantages and disadvantages of HEVs [4].

Table 1.1 - Advantages and Disadvantages of HEVs [4]

Advantages of HEVs	Disadvantages of HEVs
• Uses less fuel, better gas mileage, costs less to operate • Provide a quieter, better ride quality • Have more efficient engines • Emit fewer pollutants • Emit fewer greenhouse gases that contribute to global warming • Reduce dependency on foreign oil	• Initial purchase price is higher • Expensive batteries that may not last the life of the vehicle • Potential safety risk due to the battery pack (high voltage poses risk to mechanics and safety workers) • Creates hazardous waste (batteries need to be disposed in an environmentally friendly manner)

1.2.1.1 Series HEV Architecture

A series HEV architecture means that the ICE does not directly connect to the driving wheels. Instead, the ICE turns a generator which drives the wheels or recharges the battery module. Figure 1.1-1.4 [5] shows schematics of a series hybrid architecture in various operating modes.

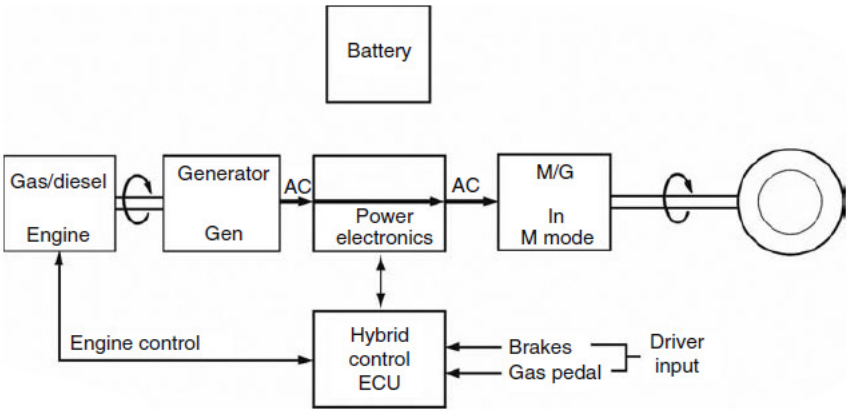

Figure 1.1 - Series hybrid architecture in cruising mode [5]

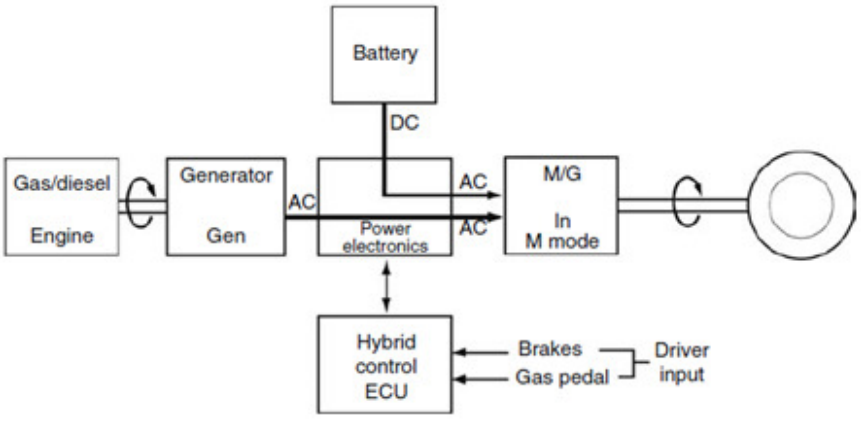

Figure 1.2 - Series hybrid architecture with acceleration uphill [5]

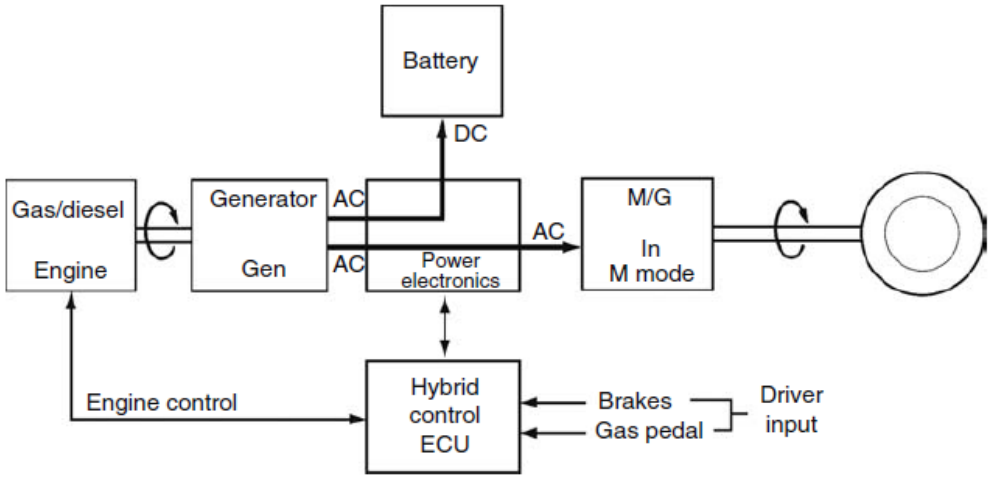

Figure 1.3 - Series hybrid architecture while charging the batteries [5]

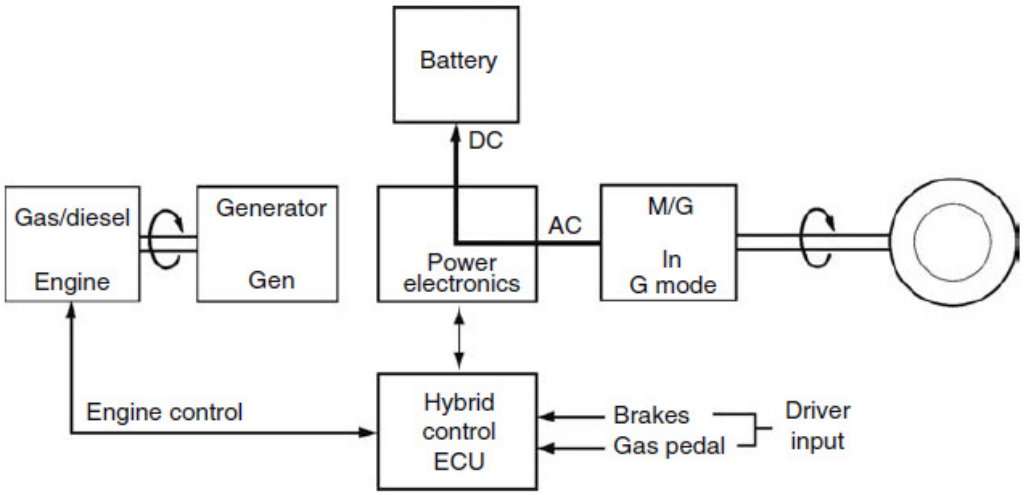

Figure 1.4 - Series hybrid architecture with regenerative braking [5]

As seen in Figure 1.1, the ICE turns a generator which is linked to the electric motor/generator (M/G), which then turns the wheels. The battery module in this case is not operating, but it would connect to the power electronics, then the M/G for added power assist when needed as shown in Figures 1.2. Figure 1.3 and 1.4 show how the battery module is charged, either from the ICE or the braking system.

1.2.1.2 Parallel HEV Architecture

In a parallel hybrid architecture, the ICE is attached to a transmission which directly powers the driving wheels. The battery module also supplies power to the driving wheels. Figures 1.5-1.8 [5] show schematics of various operating conditions for an HEV parallel architecture.

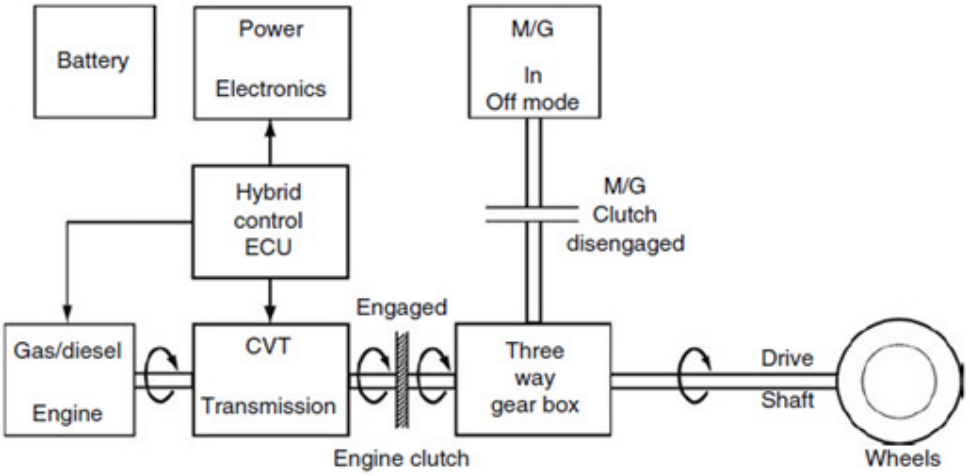

Figure 1.5 - Parallel architecture under normal cruising conditions [5]

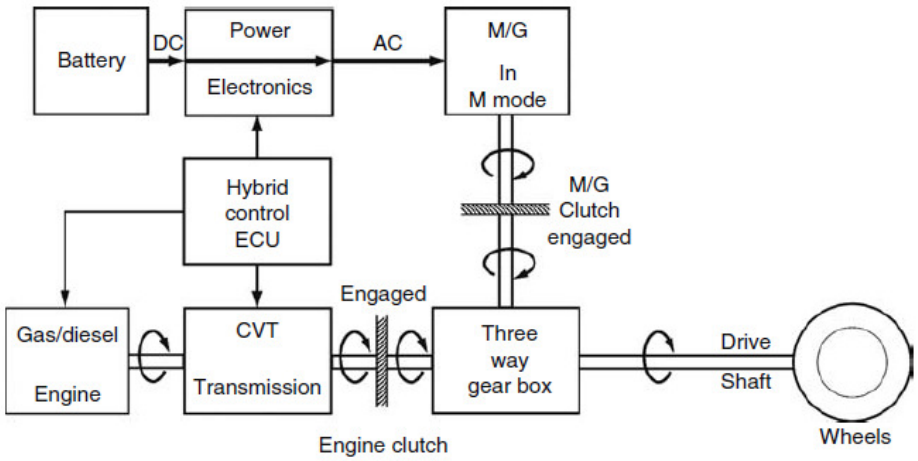

Figure 1.6 - Parallel architecture under acceleration [5]

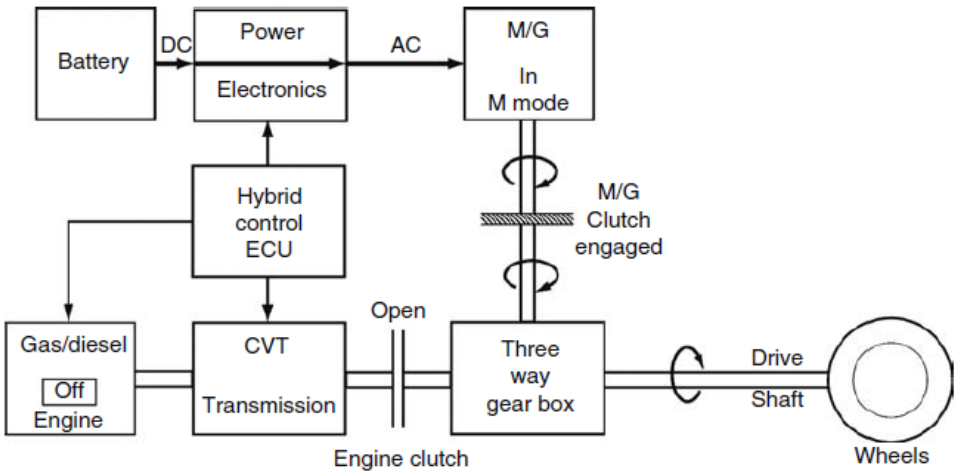

Figure 1.7 - Fully electric mode [5]

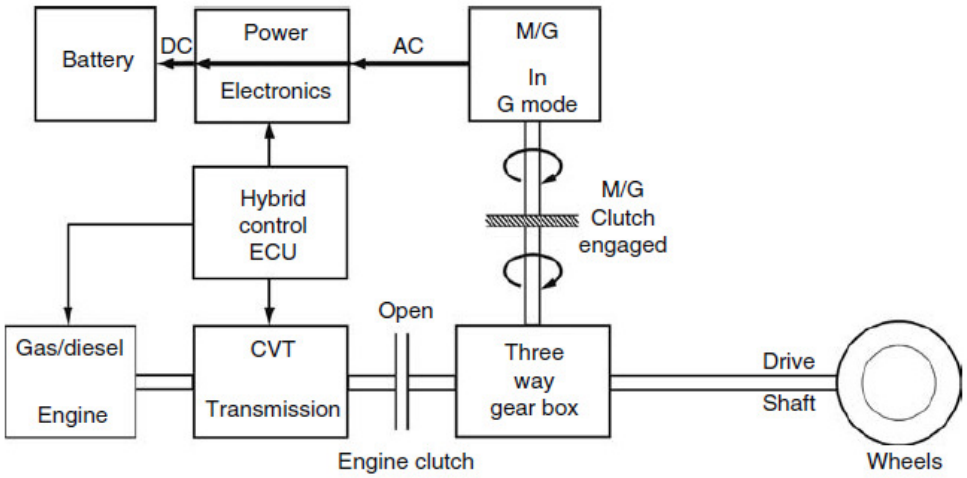

Figure 1.8 - Parallel regenerative braking [5]

From Figures 1.5-1.8, it can be seen that the main difference between the parallel and series systems is the addition of a transmission, clutches and a three way gear box, which add complexity and are a disadvantage to the parallel setup. However, the ability for parallel HEVs to operate with only the ICE, or electric only, or both simultaneously, is a key advantage to the architecture. In addition to the extra

components, the ICE can't be controlled solely along the most efficient operation line as with a series setup, which leads to higher emissions.

1.2.2 Electric Vehicles

Electric vehicles have been around since the early 1900's. In the year 1900, out of the 4,200 vehicles sold, 40% were steam powered, 38% were electric, and 22% were gasoline [6]. However, EVs have had varying degrees of interest since inception. With the whole world focusing on greener and cleaner modes of transportation because of air pollution and global warming, EVs are re-gaining more attention in the 21st century. While an HEV can help improve overall fuel economy and lower emissions, an EV completely eliminates the ICE and fuel tank, and replaces it with an electric motor/generator and battery module. This means that EVs are zero emission vehicles [at the tailpipe] and the batteries are charged by plugging the vehicle into a standard wall outlet, or a specifically designed charging station. The ICE has been the dominant propulsion system due to the fuel, which has a greater energy density than any battery. But with advancing battery technology in the 21st century, EVs are making more economical and practical sense. Figure 1.9 [7] is an example of an EV drive train.

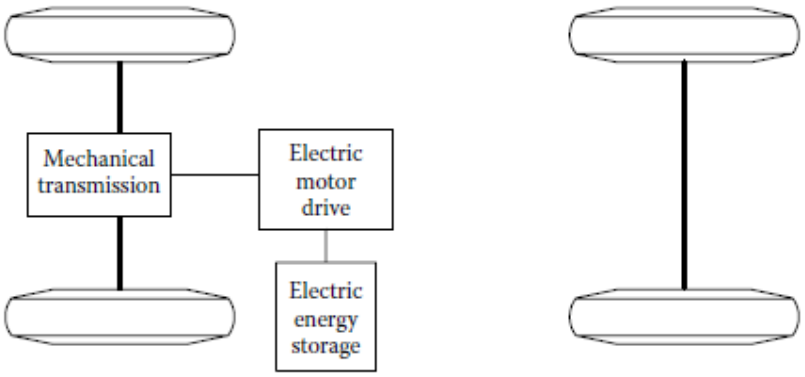

Figure 1.9 - Simplified illustration of EV drivetrain [7]

There are several EV configurations due to the difference in propulsion characteristics and energy sources. Some of the potential configurations are outlined below [7], with reference figures in Figure 1.10 [7]:

a) The ICE is replaced by an electric propulsion system. Components include an electric motor, clutch, gearbox and a differential unit. The gearbox helps to maintain given load and speed requirements. The differential unit is the same as a conventional vehicle and enables the wheels to be driven at different speeds when the vehicle runs along a curved path.

b) The multispeed gearbox can be replaced in this system when an electric motor with a wide speed range is used. This means that the gearing is fixed at one ratio, and there is no need for a clutch system. This helps reduce weight and also helps with part consolidation.

c) This is a similar setup to b) with the electric motor, fixed gearing, and differential. However, it is mounted transversely, which simplifies and compacts the design further.

d) The differential is removed and replaced by a motor and fixed gearing at each wheel. Each wheel can operate at a different speed when negotiating turns.

e) The drive train is further simplified by putting the motor in the wheel. This arrangement is called a “wheel-motor”. A planetary gear set may be employed to reduce the motor speed and enhance the torque, allowing the motor to run at high speed.

f) The motor is directly connected to the wheels without any other supplementary system. For this setup, the motors need to have high torque to get the vehicle moving.

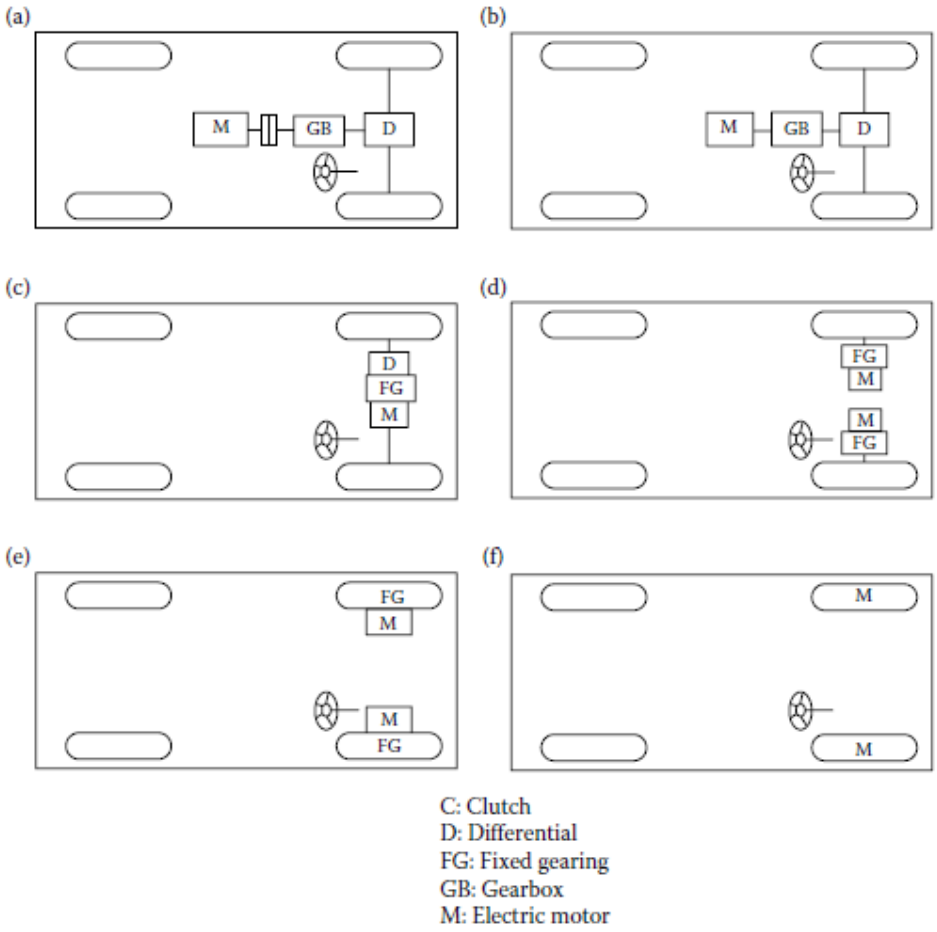

Figure 1.10 - Various EV configurations [7]

1.2.3 Battery Thermal Management

Much like an ICE needs a cooling system, the battery modules in EVs and HEVs need a cooling system as well. Battery performance influences the availability of power when starting or accelerating, energy, and charging characteristics [8]. Varying temperature affects battery life, amd has an impact on the overall fuel economy and operating range [8-10]. It is desired that the batteries operate at a specific temperature, and that temperature is dependent on the electrochemistry of the battery [8]. While a battery manufacturer may specify a battery operating temperature range,

the overall operating temperature range for a vehicle is much higher. This is where thermal management of the battery system is required, either to cool or heat the batteries outside of the manufacturer's specified battery temperature operating range. Even with a known overall temperature range, there is still a risk of uneven temperature distribution throughout a battery module, which can lead to unbalanced electrical performance [8]. To solve the issues related to battery thermal management, certain questions need to be considered:

- What type (electrochemistry) of batteries will be used?
- What temperatures will the battery module be subjected to in the vehicle?
- How much heat needs to be rejected from the battery module?
- What are the costs associated with the design(s)?
- What type of cooling system will be used (air or liquid)?

The thermal management system must also be designed to suit automotive criteria, which includes:

- Lightweight, compact, reliable and cost effective;
- Easy assembly and placed in an appropriate position in the vehicle;
- Easy access for maintenance;
- Low parasitic power loses;
- Offer ventilation for potentially harmful gases emitted from the batteries.

1.2.3.1 Air Cooling

When using air to cool a battery module, it flows though the pack and heat is removed by forced convection. The air system can either be classified as passive or active cooling. A passive system means that only the ambient environment is used to supply

air, which is either from outside the vehicle, or from the air in the cabin of the vehicle, as shown in Figure 1.11 [8].

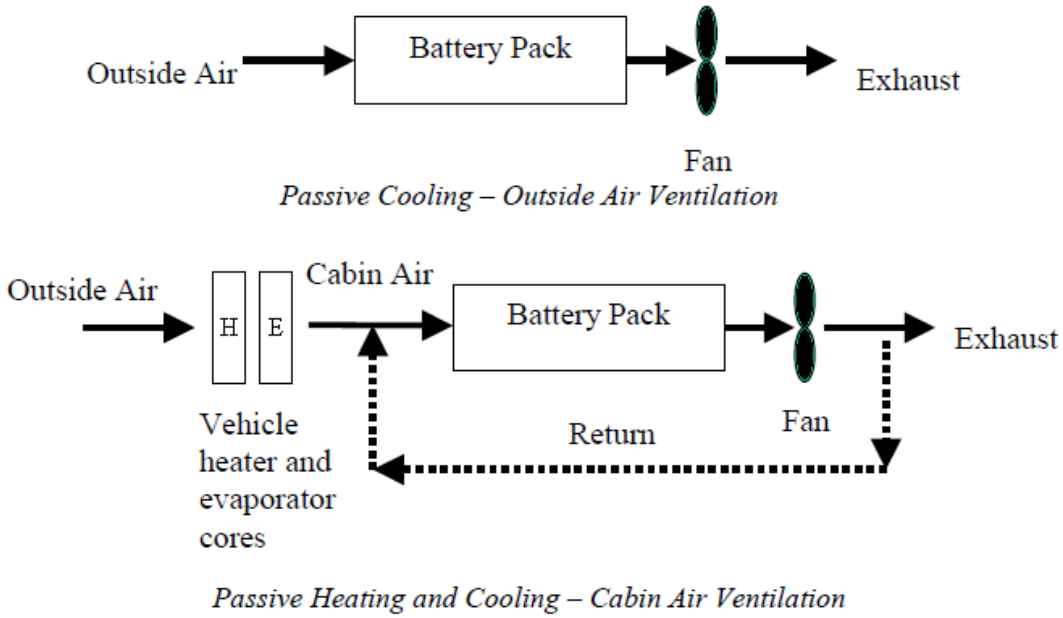

Figure 1.11 - Passive air system from outside and cabin air [8]

An active system is a built-in system designed to provide heating and/or cooling as shown in Figure 1.12 [8].

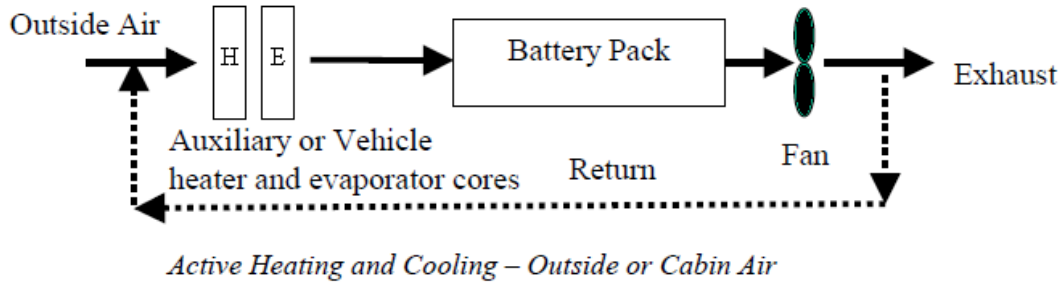

Figure 1.12 - Active air system [8]

.

Air cooled systems can be seen in HEVs currently on the market. Figure 1.13 is an example of a passive air cooled system in a Lexus hybrid SUV [11] inside the vehicle. The fans can be seen on the right side of each battery module, which moves the air through the channels between each individual cell stack.

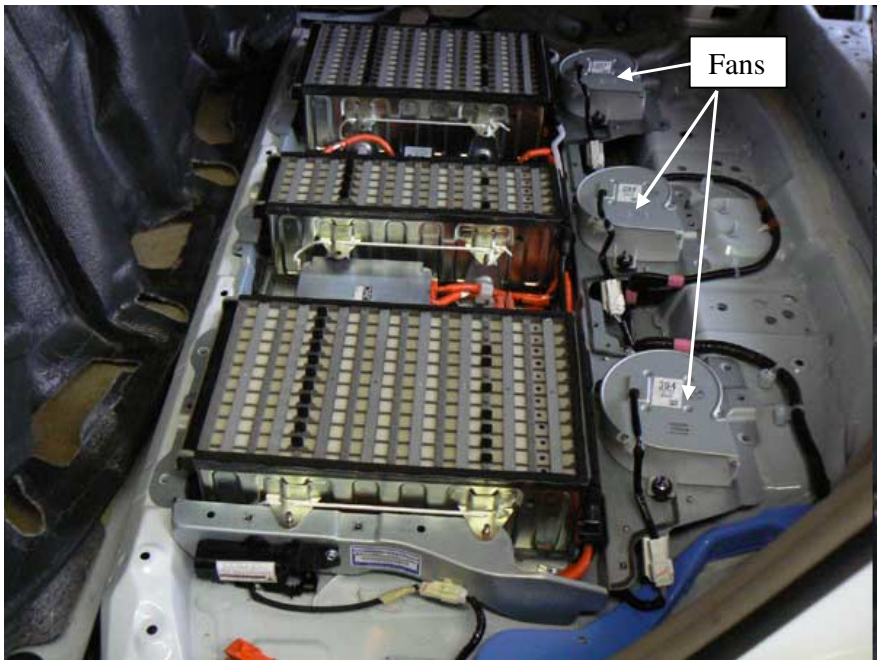

Figure 1.13 - Air cooled system installed in a hybrid Lexus SUV [11]

1.2.3.2 Liquid Cooling

Liquid cooling of the battery module involves submerging the batteries directly in a liquid bath, or liquid flowing through jackets which cool the cells by way of conduction. If the batteries are directly submerged into a liquid, the fluid used in this process must be a dielectric fluid, like mineral oil, otherwise, the indirect fluid requires jackets that are not electrically conductive and fluids like water/ethylene glycol mixtures are used [8]. Like the air cooled systems, liquid cooled systems can be passive or active, and the definitions of passive and active remain the same. For

heating and cooling of a battery module, the fluid that leaves the module can be cooled by flowing through the automotive radiator or through the AC unit. For heating, the fluid exiting the module would pass through a liquid coupled heat exchanger (with the other fluid being the engine coolant), which heats the fluid before reentering the module. A pump is needed to circulate the fluid through the battery pack and a fan or pump is required on the heat exchanger/evaporator side. A fan would be used with a passive system with outside air, and a pump would be required when there is another circulating fluid [8]. Figure 1.14 [8] is a simplified schematic of a liquid cooled system. The grey box around the battery pack indicates the fluid in the pack (whether direct or indirect).

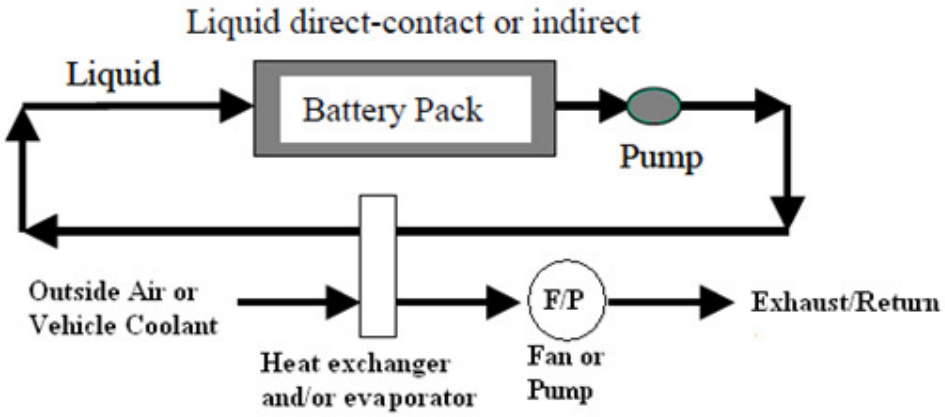

Figure 1.14 - Liquid cooled battery module schematic [8]

This system is more complex than an air cooled system. An air cooled system may be an easier approach than liquid cooling, but it is much less capable of heat transfer than liquid systems. Determining the heat transfer capabilities of a liquid system depends greatly on the material properties of the module wall, jacket tubing, and thermal properties of the fluid and flow rate. For a direct contact liquid system,

the heat transfer rate for fluids, such as oil, are much higher than air due to fluid properties such as thermal conductivity [8].

Fluid viscosity is higher for oil than air, which means greater pumping power is needed to move the fluid through the pack. Even if the flow rate for oil is lowered, it still offers a 1.5 - 3 times higher heat transfer coefficient than air [8]. When using an indirect liquid cooling process, liquids like water and ethylene glycol have a lower viscosity and higher thermal conductivity, when compared with oils, which leads to excellent heat transfer capabilities. But since these fluids are not in direct contact with the batteries, conduction through the jacket walls reduces the heat transfer capabilities [8]. In the current automotive market, there are no HEVs using direct liquid cooling for the battery module. However, the high priced Tesla Roadster EV and the upcoming Chevrolet Volt extended range electric vehicle (EREV) have indirect liquid cooled battery modules.

1.2.4 Entropy Generation

Entropy is governed by the Second Law of Thermodynamics, which can be explained by two statements [12].

The Kevin-Planck Statement: It is impossible to construct a device that will operate in a cycle and produce no effect other than the raising of a weight and the exchange of heat with a single reservoir.

The Clausius Statement: It is impossible to construct a device that operates in a cycle and produces no effect other than the transfer of heat from a cooler body to a hotter body.

Entropy generation is a measure of the irreversibilities in a system, whether for a control mass or control volume. Entropy is generated by friction of flowing fluids and heat transfer processes [13-16]. It characterizes the potential work lost in a system, so a reduction in entropy can lead to a better overall system [16].

1.2.5 Entropy Generation Minimization

There have been numerous studies on how to reduce the generation of entropy in flow systems to improve efficiency [13-15, 17-20]. Entropy Generation Minimization (EGM) involves the analysis of various system configurations to find an optimal design point. Even if an optimal design point is found, it may not always be the best solution, because the optimal point may not be achievable in a practical application. Bejan has reported many studies in the area of entropy generation minimization, on a broad range of topics including fluid flow and heat transfer [21].

1.2.6 Exergy

Exergy destruction (X_{des}) is equal to the entropy generation (S_{gen}) and surrounding temperature (T_0).

$$X_{des} = (T_0)(S_{gen}) \tag{1.1}$$

Like entropy generation minimization, it is used to evaluate a system's performance from a thermodynamic frame of reference based on the Second Law of Thermodynamics [22]. To the author's knowledge, there has not been a comprehensive exergy based analysis of automotive systems, although the aviation industry has compiled various entropy/exergy based studies (to be described below).

1.2.6.1 Scramjet Configurations

Scramjet is an acronym for Supersonic Combustion Ramjet, which is a type of hypersonic air-breathing propulsion system [23]. Amati et al. [23] analyzed a fuelling method based upon the different aspects of various scramjet configurations. The intention of such analysis was to identify an ‘‘optimal’’ configuration and an ‘‘optimal’’ fuel, both from a thermodynamic and engineering point of view. Optimal is in quotations because the term applies to an optimal configuration for a scramjet, under the required operation, not a universal optimal solution. Amati states that a ‘‘system approach’’ was adopted and an analysis was performed on the scramjet engine, as if it was composed of several ‘‘black-boxes’’ that represent individual components. The vehicle is viewed as a ‘‘Large Complex Energy System’’. Amati et al. used black boxes and a large energy system shown in Figure 1.15 [23].

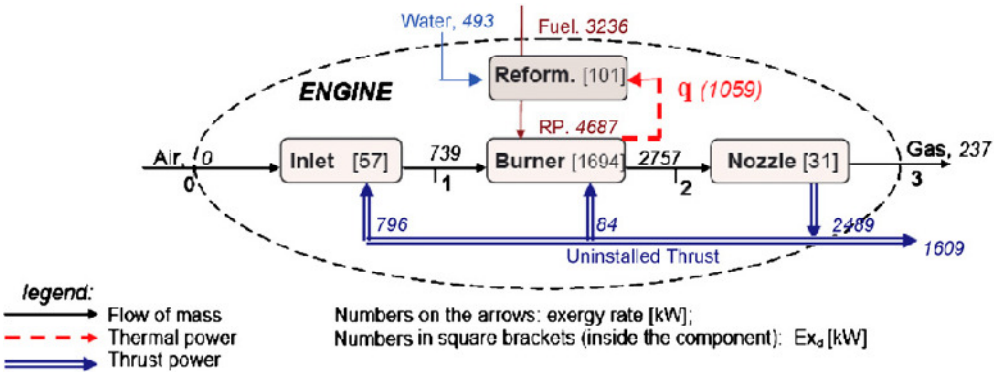

Figure 1.15 - Scramjet exergy block diagram [23]

1.2.6.2 Aircraft Environment Control System

Ordonaz and Bejan [24] discuss a concept called constructal design, which is the link between the maximization of performance and the generation of optimal architecture in flow systems, in engineered or natural systems. Thermodynamic optimization is necessary to identify ways, both features and procedures, which allow a system to fulfill its functions and perform at the highest thermodynamic level possible. On an aircraft, there are many systems and processes that contribute to the ultimate destruction of exergy supplied by the fuel. Figure 1.16 [24] shows the distribution of exergy losses in the aircraft, explained by Ordonaz and Bejan.

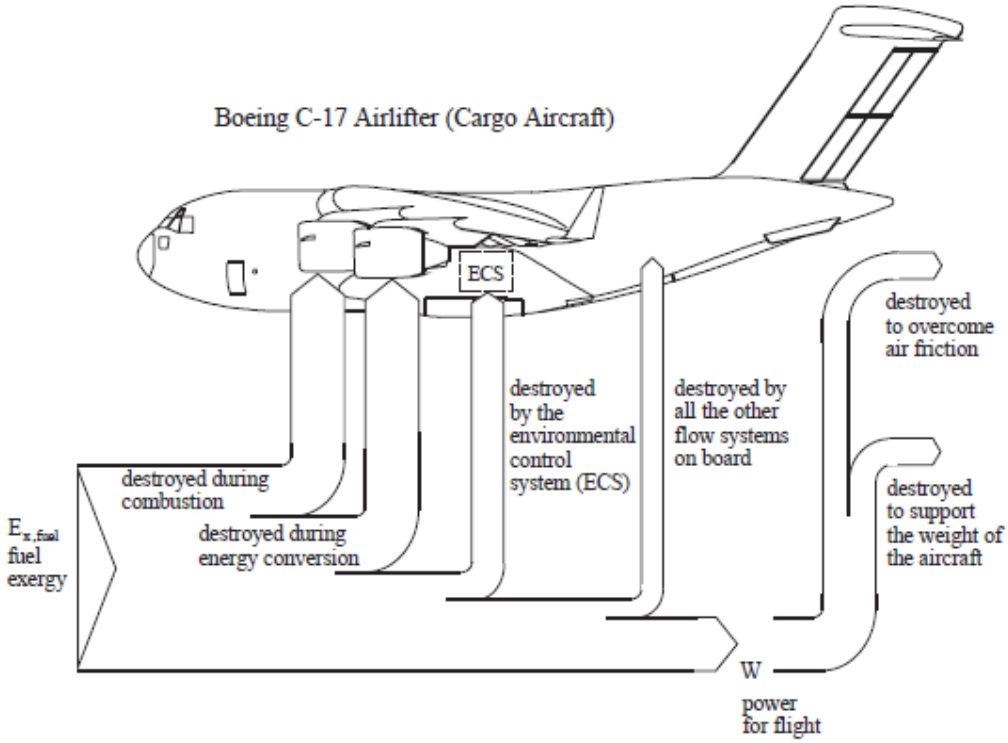

Figure 1.16 - Aircraft exergy diagram [24]

For the amount of fuel used to power the aircraft, the first loss occurs during the combustion process. Exergy destruction is then experienced in the irreversible

operation of the engines due to energy conversion. The remaining exergy destruction occurs in the power consumed by the engine to operate all of the subsystems within the aircraft. The power for flight (W) is principal among all functions required to maintain the flight. The destruction of W is due to the turbulent flow around the aircraft, to overcome air friction and supports the weight of the aircraft. The paper also states: "The minimization of the flying power requirement leads to a prediction of the optimal cruising speed, which agrees well with the observed characteristic speeds of insects, birds and aircraft: the optimal cruising speed is proportional to the mass of the flying body raised to the power 1/6. The rest of the power generated by the engine is destroyed in the auxiliary systems, which are numerous" [24]

One of the larger sections of the plane contributing to exergy destruction is the environmental control system (ECS), which is responsible for creating and maintaining adequate air quality throughout the aircraft. The ECS system is composed of various components. Ordonez and Bejan investigated a way to find the minimum power required, while maintaining functionality, from a thermodynamic point of view. To maintain the air quality within the aircraft cabin, the ECS system follows what is called the "bootstrap air cycle". The function is described as follows:

- Air is bled from the engine compressor;
- Air from the compressor enters a secondary compressor driven by its own turbine;
- Air is processed through a crossflow heat exchanger;
- Air flows through a turbine and into the cabin at the correct temperature.

A figure of the "bootstrap air cycle" is shown in Figure 1.17 [24].

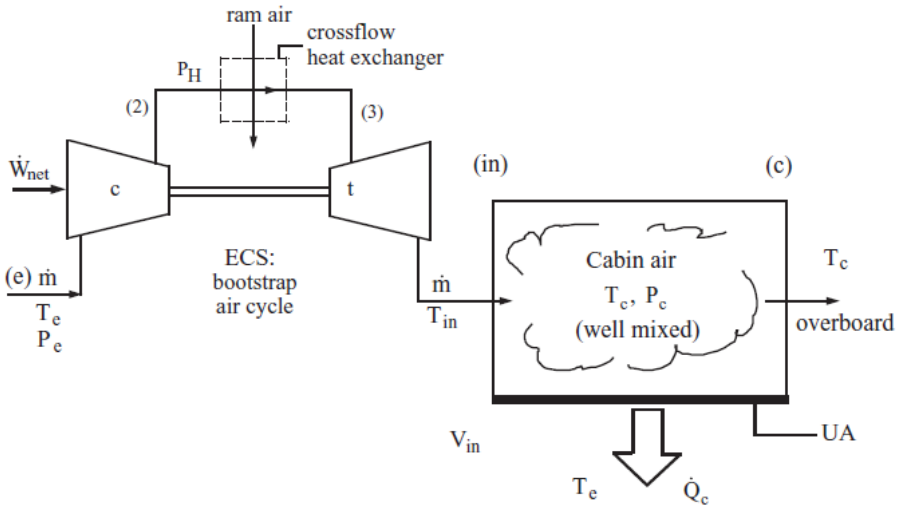

Figure 1.17 - Bootstrap air cycle [24]

By reducing the power consumed and optimizing the components within the ECS system, the losses associated with the ECS are reduced when the overall exergy destruction for the aircraft is reduced. Perez-Grande and Leo [25] further analyzed the ECS system, focusing on the minimization of weight and entropy through geometric optimization of the heat exchangers. They analyzed the entire ECS system as a whole unit, rather than individual components.

1.2.6.3 Exergy Due to Lift

Paulus and Gaggioli [26] stated that aircraft energy systems are unique because exergy is required not only for the systems to operate, but it is also responsible for the power to lift and hold the aircraft in the sky. For any exergy analysis to be completed, exergy flow diagrams must be created and with successful exergy flow diagrams, exergy can be used to link various systems during the design process. Paulus and Gaggioli developed a model to demonstrate the importance of exergy during lift-off

and during coasting of a small aircraft. The exergy flow diagram for the small aircraft is shown in Figure 1.18 [26].

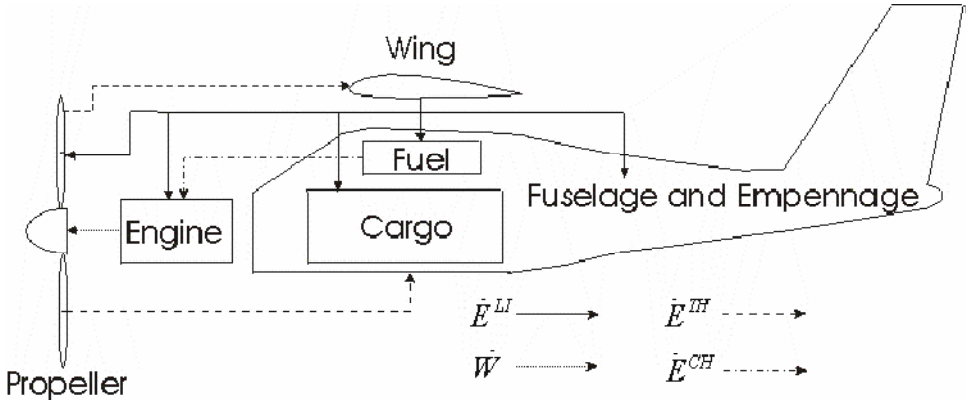

Figure 1.18 - Exergy flow diagram [26]

1.2.7 UOIT EcoCar

EcoCAR: The NeXt Challenge is a three-year collegiate advanced vehicle technology engineering competition, established by the United States Department of Energy (DOE) and General Motors (GM). It is managed by Argonne National Laboratory. There are 16 teams across North America competing to build vehicles that will help reduce the environmental impact in the transportation sector, by minimizing a vehicle's fuel consumption and emissions, while retaining the vehicle's performance, safety and consumer appeal. Students use real-world engineering processes to design and integrate their advanced technology solutions into a GM-donated vehicle.

The 16 competing teams are tasked with designing and building advanced propulsion system that are based on vehicle categories from the California Air Resources Board (CARB) zero emissions vehicle (ZEV) regulations. Some of the advanced vehicle architectures in the competition include full-function electric, range-extended electric, hybrid, plug-in hybrid and fuel cell technologies. Other vehicle

innovations are vehicle weight reduction and advanced materials, improved aerodynamics and alternative fuel types, such as ethanol and hydrogen.

UOIT is the only team in the competition to design a full function electric vehicle. The team is supervised by Dr. Greg Rohrauer and this thesis is based on a portion of the EcoCAR design. An introduction to the vehicle being designed at UOIT will be briefly explained in the following section.

1.2.7.1 Base Vehicle

The base vehicle is a 2009 Saturn VUE XE, which is a front wheel drive cross-over vehicle designed to offer both the fuel economy of a sedan and the spatial interior of a SUV. The VUE is powered by an ECOTEC 2.4L I4 engine and a Hydra-Matic 4T45 four-speed front wheel drive electronically controlled automatic transaxle with overdrive. The 2.4 liter DOHC I4 engine is equipped with Variable Valve Timing (VVT) technology, which offers greater power, improved fuel efficiency and emissions reduction. The ECOTEC engine is rated at 169 hp @ 6200 rpm and 161 lb-ft @ 5100 rpm. The UOIT team uses PSAT (Powertrain System Analysis Toolkit) V6.2 SP1 for the model development and model simulation. PSAT is a well known for evaluating and estimating a vehicle's performance. The following Table 1.2 [27] is the drivetrain configuration as modeled in PSAT with the competition vehicle.

Table 1.2 - Base Saturn VUE PSAT Model [27]

Specification	**Requirement**		
EcoCAR	**Production Vue**	**PSAT**	**Competition**
Accel 0-60	10.6 s	11.5 s	≤14 s
Accel 50-70	5 s	5.9 s	≤10 s
Quarter Mile	18.7 s	19.1 s	TBD
Towing Capacity	680 kg (1500 lb)	680 kg (1500 lb)	≥680 kg @ 3.5%, 20 min @ 72 kph (45 mph)
Cargo Capacity	.83 m^3	.83 m^3	TBD
Passenger Capacity	5	5	≥4
Braking 60 - 0	38 m- 43 m (123 -140 ft)	38 m- 43 m (123 - 140 ft)	< 51.8 m (170 ft)
Mass	1758 kg (3875 lb)	1743 kg (3843 lb)	≤ 2268 kg* (5000 lb)
Starting Time	≤ 2 s	≤ 2 s	≤ 15 s
Ground Clearance	198 mm (7.8 in)	198 mm (7.8 in)	≥178 mm (7 in)

From Table 1.2, it can be seen that the PSAT model of the Saturn VUE is very close to the published performance data by General Motors.

1.2.7.2 UOIT Electric Vehicle Background

As previously mentioned, UOIT's EcoCAR team proposed to build a full function electric vehicle. Five OEM electric pick-up trucks, two electric buses, and a minivan which were built in the original CARB ZEV era, are currently at a lab facility in Uxbridge, Ontario. Each of the electric vehicles has been refurbished, either by rebuilding the battery pack, repairing faulty controls or power electronics, chargers and / or mechanical elements of the drive system [28]. The experience from working

on this ZEV fleet has been applied to the EcoCAR competition. UOIT is conducting many experiments on alternative vehicle technology, and the EcoCAR competition is another way to strengthen UOIT as an advanced vehicle technology leader. One of the projects is application of different battery chemistries for the conversion of a conventional SUV into a Plug-in Hybrid. The EcoCAR team has gained experience with lithium polymer batteries, while designing and building a lithium polymer pack and battery management system for a PHEV-60 Chrysler Pacifica. The APS electric buses, for example, have 116 kWhr SAFT NiCad battery packs, and 40 KW, 3 phase 575 volt chargers [28]. UOIT has chosen to build a full function electric vehicle and the team is equipped to develop an electric Saturn VUE.

1.2.7.3 UOIT EcoCAR Architecture

UOIT's full function electric vehicle requires all pre-existing ICE mechanical and fuel systems to be removed so the electric motor and battery system can be implemented. The electric architecture is the simplest architecture to implement, because is no overly complex powertrain configuration and control scheme. The final specifications of the electric vehicle powertrain are shown in Table 1.3 [29]. Table 1.4 [30] is a PSAT simulation summary to show that the designed electric vehicle architecture will meet the requirements of the EcoCAR competition. Figure 1.19 [28] and Figure 1.20 [28] depict how the electric motor and batteries will be adapted to the Saturn VUE.

Table 1.3 - Final Powertrain Configuration of UOIT EcoCAR [29]

Components	Supplier
Motor / Drive (peak / continuous)	Delphi S-10EV (110 / 40) KW
Inverter Drive	MES-DEA TIM 600 80 - 450 Volts input, 236/400 A cont/max
Battery	Kokam SLPB (Li-Poly)
Cell Weight	4.9 kg (pouch)
Battery Management	REAP systems, Li-BMS-14, (7 networked modules)
Number of Cells	92
Cell nominal voltage	3.7 V (2.7 V Min - 4.25V Max)
System voltage (min / nominal / max)	250 / 340 / 388 V
Volume Packing Factor	1.2
Available energy (100% DOD)	85 KWh (80 KWh nominally @ 95% DOD cycling)
Cell Energy Density	190 Wh/kg
Battery Ah	250 Ah (typical)
Battery Rint per cell	0.43 mΩ (typical)
Battery Cycle Life	>1500 cycles @ 100% DOD, >3400 @ 80% DOD
Vehicle Curb Weight	2091 kg (lighter battery box & motor assembly)
Frontal Area	2.641 m^2
Drag Coefficient	0.376
Tire	235/65R16
Tire rolling resistance	0.0068

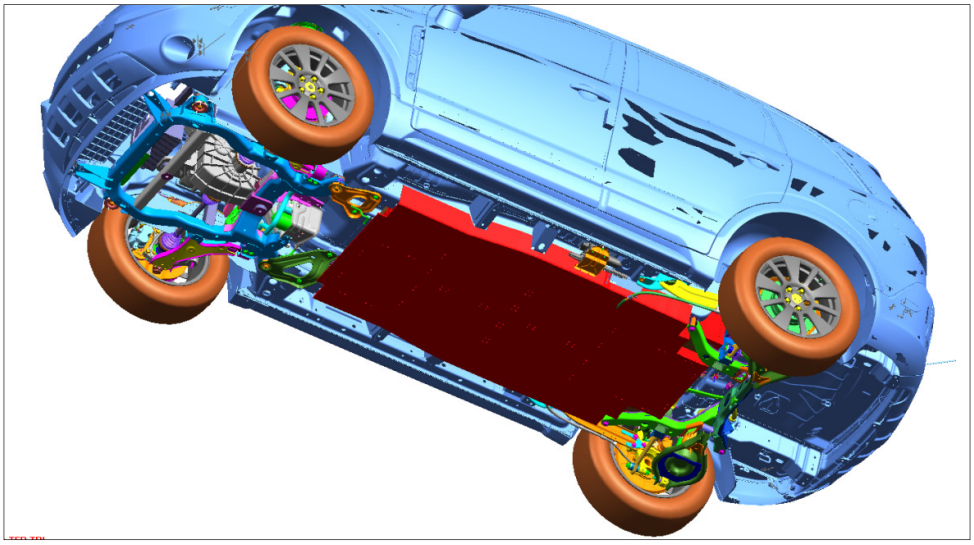

Figure 1.19 – Underside battery module (red box in photo) [28]

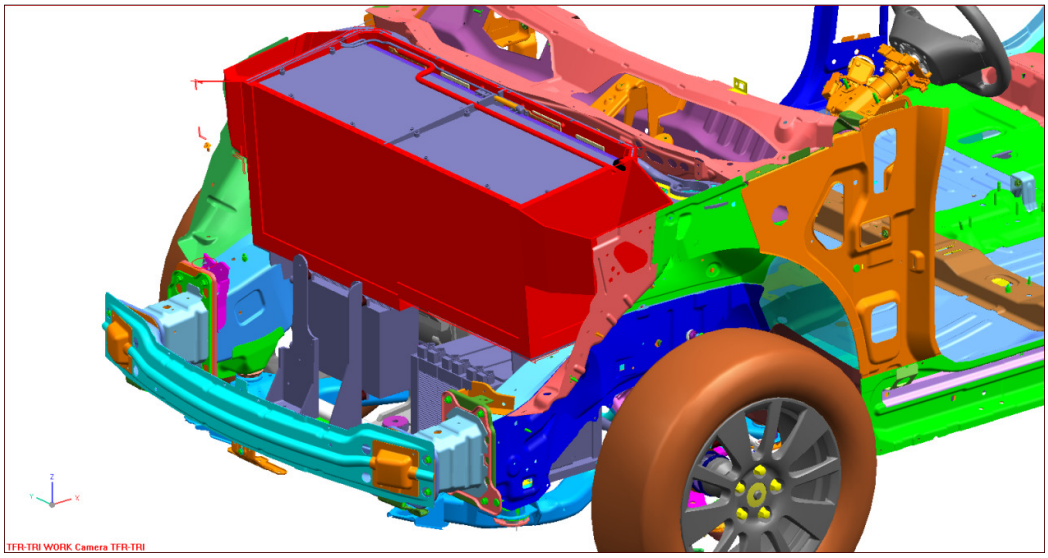

Figure 1.20 - Engine bay with front battery (red box) and EV1 drivetrain [28]

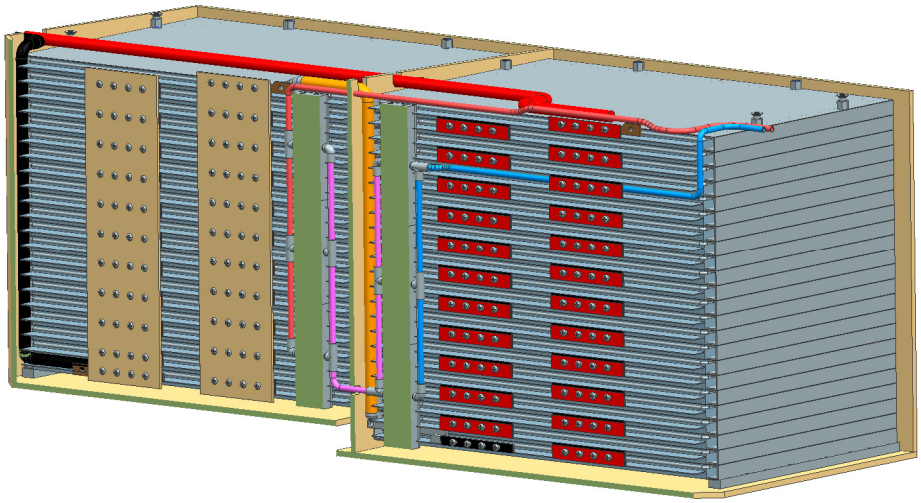

Figure 1.21- Cell stacks in front battery box [28]

Table 1.4 - Vehicle Technical Specifications [30]

Specification	Competition		Team
EcoCAR	**Production VUE**	**Competition Requirement**	**VTS**
Accel 0-60	10.6 s	≤14 s	13.5 s
Accel 50-70	7 s	≤10 s	7.5 s
UF Weighted FE *	8.3 l/100 km (28.3 mpgge)	7.4 l/100 km (32 mpgge)	2.67 l/100km (88 mpgge)
GHG emissions*	246 g/km	217 g/km	165 g/km
Towing Capacity	680 kg (1500 lb)	680 kg @ 3.5%, 20 min @ 72 kph (45 mph)	≥680 kg @ 3.5%, 20 min @ 72 kph (45 mph)
Cargo Capacity	.83 m^3	Height: 457 mm (18”) Depth: 686 mm (27”) Width: 762 mm (30”)	Stock configuration
Passenger Capacity	5	≥4	5
Braking 60 - 0	38 m- 43 m (123 -140 ft)	< 51.8 m (170 ft)	51.8 m (170 ft)
Mass	1758 kg (3875 lb)	≤ 2268 kg* (5000 lb)	2130 kg
Starting Time	≤ 2 s	≤ 15 s	≤ 2 s
Ground Clearance	198 mm (7.8 in)	≥178 mm (7 in)	190 mm (7.5 in)
Range (UF=.971)	> 580 km (360 mi)	≥ 320 km (200 mi)	402 km (250 mi)

1.3 Objectives of Thesis

With electric drivetrains gaining attention as an alternate propulsion system to the ICE, there is extensive electric vehicle development being conducted at UOIT. A UOIT team is building a full function electric vehicle for "EcoCAR the Next Challenge" competition. This thesis analyzes a liquid indirect active cooling system, which can be implemented on the UOIT EcoCAR, or used for new EVs and HEVs with a focus on entropy generation to improve system performance. The objectives of this thesis are listed as follows:

- There are several components needed to create an indirect cooling system. Therefore, all critical system components will be identified and a new flexible entropy-based design model will be created for those with multiple configurations.
- In order to evaluate the entropy generation in the system, entropy generation will be calculated for each component in the system. This will help determine optimal operating conditions, which minimizes power consumption and maximizes system efficiency.
- To evaluate the overall entropy generation in the system, the entropy generation for each component is added together. This thesis will model how the total entropy of the system is affected by different operating conditions of critical components. Entropy Generation Minimization for battery thermal management systems (BTMS) can be based on the models developed in this thesis.

CHAPTER 2 - SYSTEM COMPONENTS

2.1 Introduction

A passive liquid cooling system is not a common, and no known vehicles incorporate it into their BTMS. A fully operational system requires the following components.

- Battery Module – Consists of multiple cells which supply power to the vehicle.
- Pump – The pump circulates the fluid throughout the system.
- Heat Exchanger (Radiator) – Used to remove heat from the cycling fluid.
- Hoses – Carry fluid throughout the system.
- Battery Management System (BMS) – Software used to control and monitor battery temperature/voltages and overall functionality.
- Temperature Sensors – Manage the individual battery temperature in the module and send information to the BMS in the event of an individual battery failure.

In this thesis, only the first four items in the above list will be considered. When the batteries, pump, heat exchanger and lines are connected, the system model is shown in Figure 2.1.

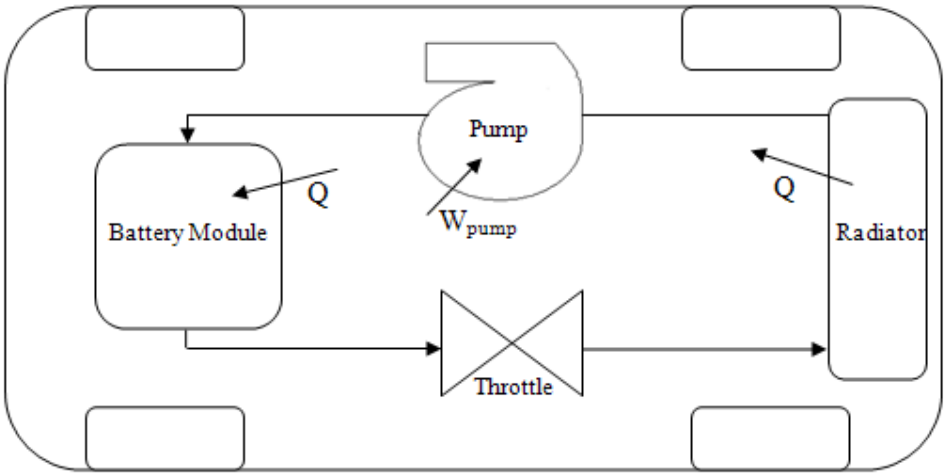

Figure 2.1 - Active liquid cooling system

Complete descriptions of each component shown in Figure 2.1 are explained in this chapter.

2.2 Battery Module

The battery module is the main power source of the vehicle, for propulsion and accessory power. The number of batteries and the physical size for the module are dependent on the type of battery, required power output, and space available. For this model, the battery design is based on the batteries used by the EcoCAR team, which are lithium polymer batteries supplied by Kokam Co., Ltd. This is pictured in Figure 2.2.

Figure 2.2 - Kokam lithium polymer cell (L = 445mm, W = 292mm, H = 16mm)

From Figure 2.2, it can be seen that the batteries are relatively flat (1.6 cm thick) with a large heat transfer area. The theory outlined in this chapter applies to any battery type and geometry, even though the model is based on a particular Kokam cell. These cells are used for their high energy output, and low temperature displacement under maximum load, due to very low internal resistance. This thesis is based upon a battery module which has a total of 48 cells, 2 stacks of 24 cells, and approximates the configuration used for the front battery box on the UOIT EcoCAR. In order to have the appropriate cooling fluid flowing through the battery module, there will be tubing carrying the fluid which is sandwiched between each battery layer. Figure 2.3 shows how this tubing will be routed on each layer. Figure 2.4 is an example of a sandwiched layer. In a practical application, the tubing will be attached to a frame, then placed in between the cells.

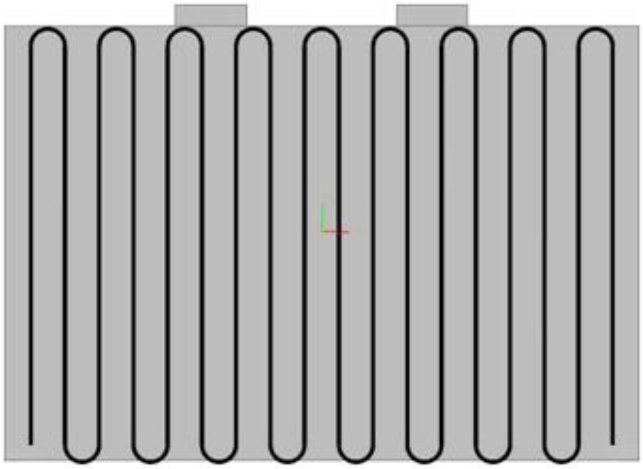

Figure 2.3 - Battery with tubes

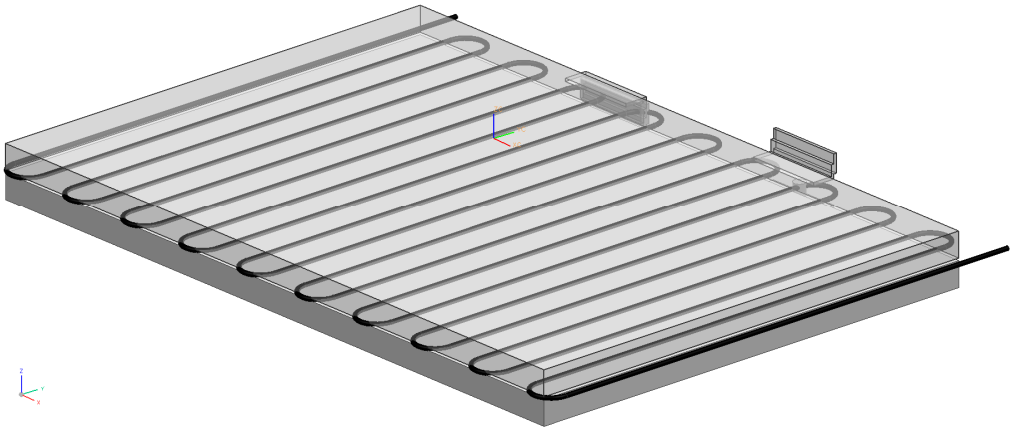

Figure 2.4 - Sandwiched cooling loop layer

The tubing is designed to cover the surface area of a cell. The analysis for the tubing length is covered in the next chapter. All of the heat in this cooling system is generated from the battery module, denoted as Q in Figure 2.1. The Q value is based upon the maximum temperature difference between the cell, mass of the cell, and specific heat of the cell. Properties are either given by the manufacturer, or found through experiments. To analyze the entropy generation within the module, it is modeled as a control volume (CV), shown in Figure 2.5.

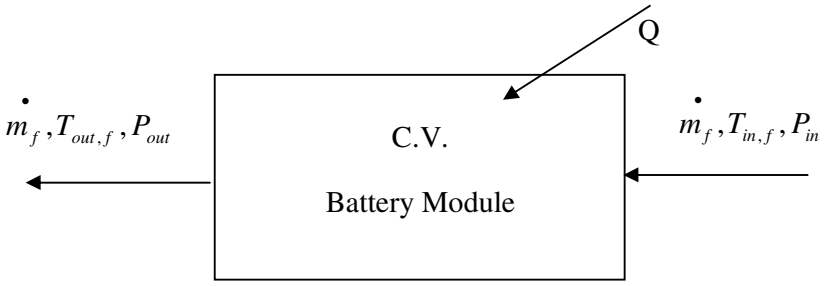

Figure 2.5 - Battery module as a control volume process

2.3 Throttle

The throttle represents a combination of all connecting hoses between components. There is no heat or work produced in this component. It is approximately a constant enthalpy process [31]. A linear pressure is assumed through the throttle to simplify the process. The control volume model is shown in Figure 2.6.

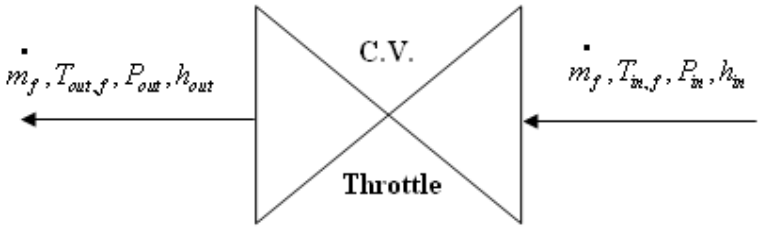

Figure 2.6 - Throttle modeled as a control volume

In reality these components have surface area and also act to radiate/absorb heat.

2.4 Pump

The pump is a key component for circulating the cooling fluid through the system, and power to drive the pump and add pressure to the system. The size of the pump is

completely dependent on the required flow rate and pressure. Once the actual pump is selected, mechanical data for the pump needs to be obtained, either directly from the manufacturer, or through interpolation of data from the pump characteristic curve [31]. The pump data will be discussed in upcoming chapters. Like the battery module and throttle components, the entropy generation will be found for the pump as well. If the pump can operate at ideal conditions while maintaining a low entropy generation, this benefits the entire system. The pump is modeled as a control volume process, as shown in Figure 2.7.

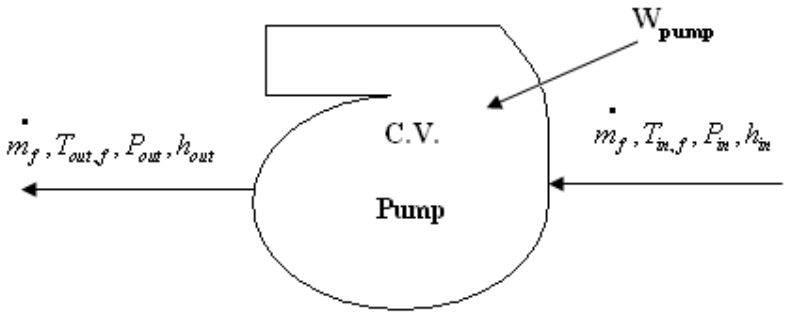

Figure 2.7 - Pump as a control volume

2.5 Heat Exchanger (Radiator)

The heat exchanger, also called a radiator in the automotive industry, is the most complicated component to design. The main purpose is to reject heat gained in the cooling fluid from the battery module. Ideally, the heat exchanger should reject the same about of heat generated in the battery module, to ensure the system is operating properly. Unlike the previous components which have a single input and output, the radiator has two fluids that pass through it. The first fluid is the hot fluid exiting the battery module. It enters the radiator and passes through multiple cores in the radiator made of metal. As the hot fluid passes through the cores convection and conduction

helps to disperse heat in the fluid. The cores have an extended finned surface to increase the heat transfer surface area of the radiator, which helps cool the fluid faster. Photos of the radiator modeled in this thesis are shown in Figures 2.8 – 2.10.

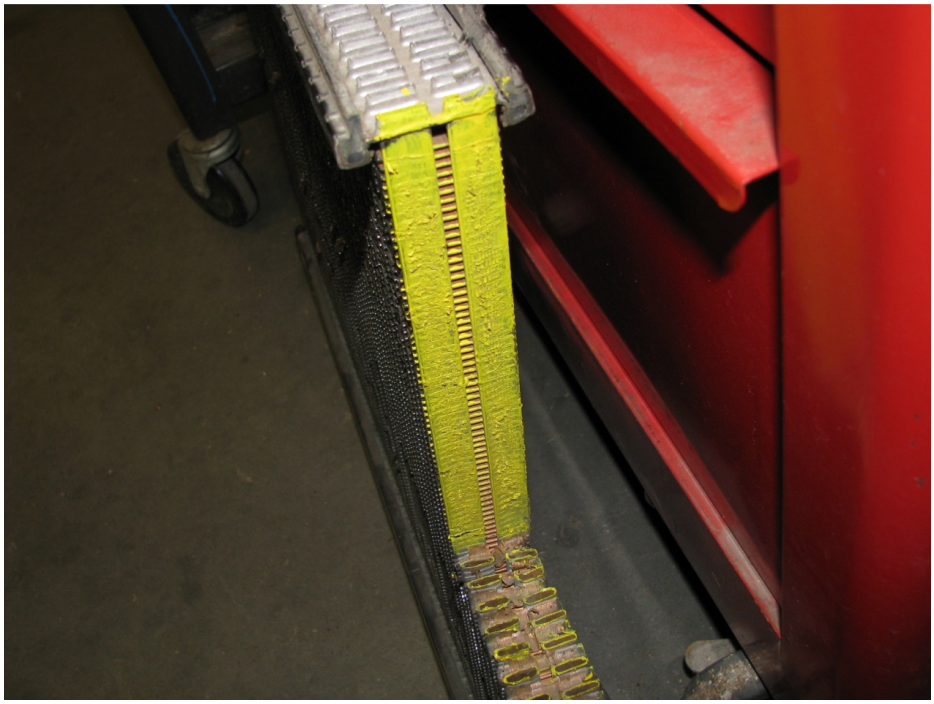

Figure 2.8 - Typical radiator cross-section

Figure 2.9 - Radiator header design

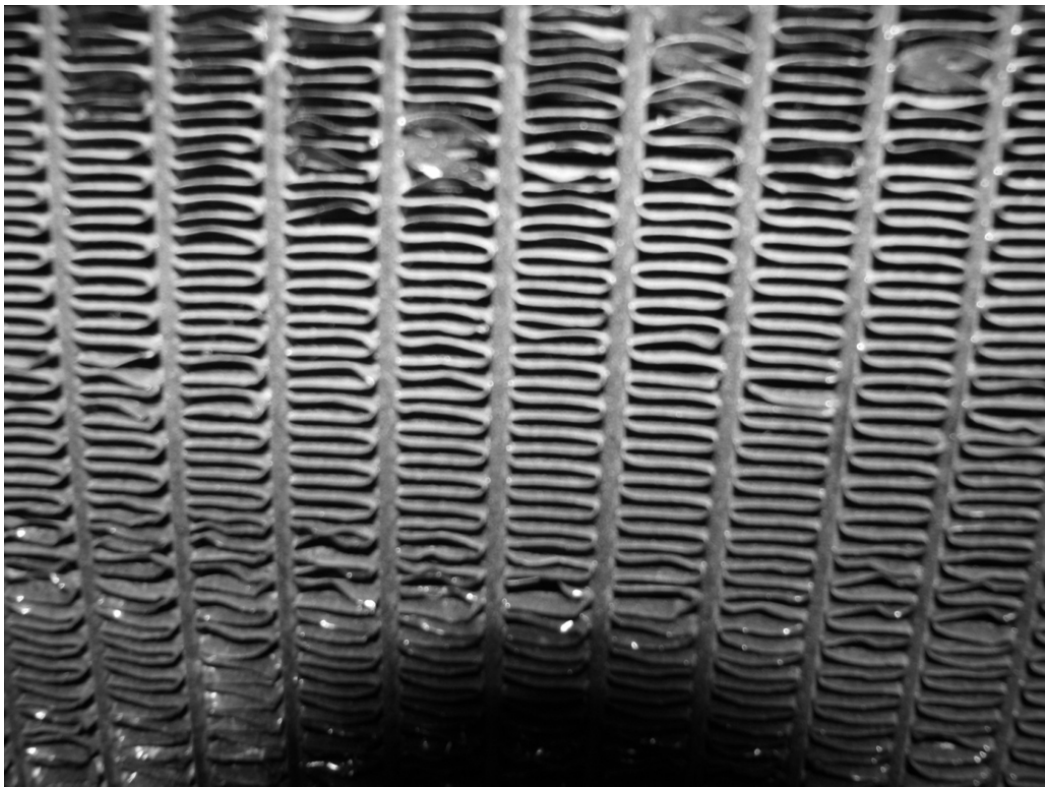

Figure 2.10 - Radiator fin and tube configuration

The fins are normally brazed/soldered to the cores, and the cores are brazed/soldered to the header plate. The second fluid passing through the radiator is air, which flows perpendicular to the hot fluid flow. The air passes over the radiator cores and fins, by means of a fan or air entering the grill of the vehicle, while it is travelling to transfer heat away and to the atmosphere. To find the entropy generation for the radiator, the change in entropy must be evaluated on the air and fluid sides. The control volume model in Figure 2.11 shows how the entropy change will be found for each fluid passing through the radiator.

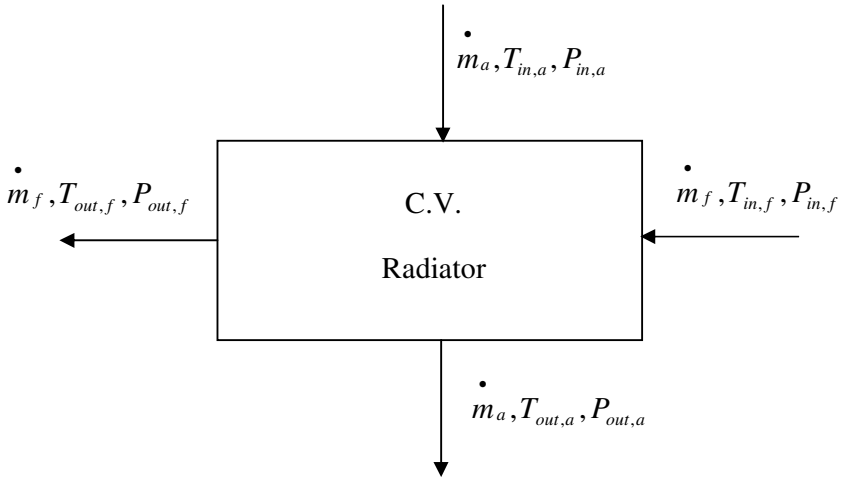

Figure 2.11 - Radiator control volume model

CHAPTER 3 - HEAT TRANSFER ANALYSIS

3.1 Battery Module Model Development

In the battery module, a key design component is the length and sizing of the tubing between each battery. The first section of this model outlines the process to find the total length of tube required for the battery module. For this model, the battery is a high energy 240Ah Kokam lithium polymer battery, shown in the previous chapter. The model can be adapted to any battery with a flat surface area, but the length and width of the surface area must be known, where the tubing will be placed, as shown in Figure 3.1. Figure 3.1 also explains key design parameters, in order to solve for the total length of tubing and the overall layout of the tubing.

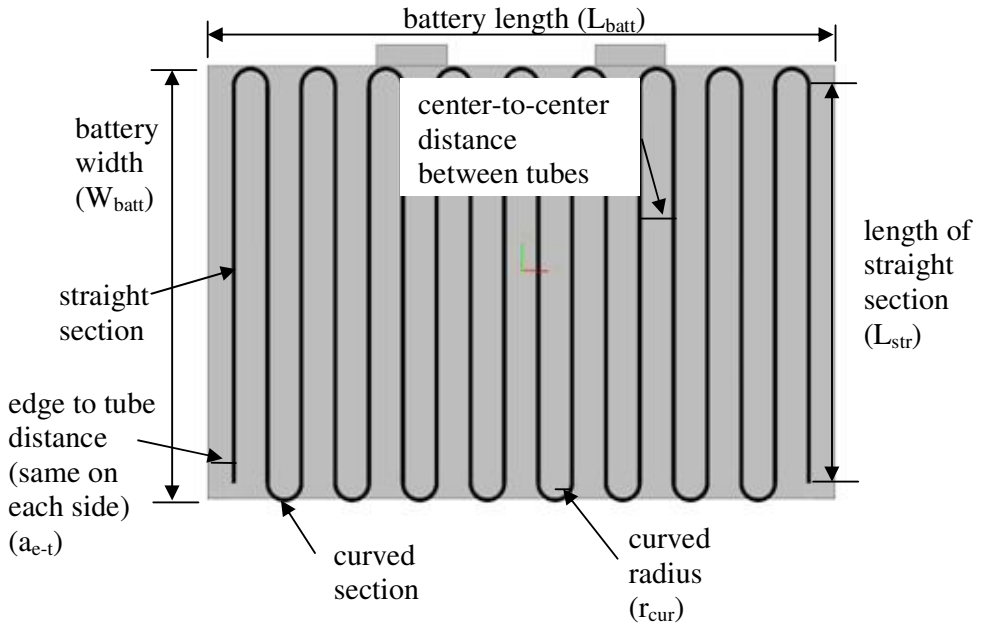

Figure 3.1 - Tubing layout between each battery and design parameters

For the Kokam cell and tubing, the dimensions are:

$L_{batt} = 445mm;$

$W_{batt} = 292mm;$

$D_{tube} = 2mm.$

Since the cooling loops are a series of straight and curved sections, the number of straight sections can be calculated, therefore leading to the number of curved sections. Certain parameters will be assumed based upon the design, specifically the spacing between tubes from wall to wall (X_{w-w}). For the battery module in this thesis, X_{w-w} will be 24mm. This means that the center-to-center tube distance (X_{c-c}) is given by:

$$X_{c-c} = X_{w-w} + D_{tube} \tag{3.1}$$

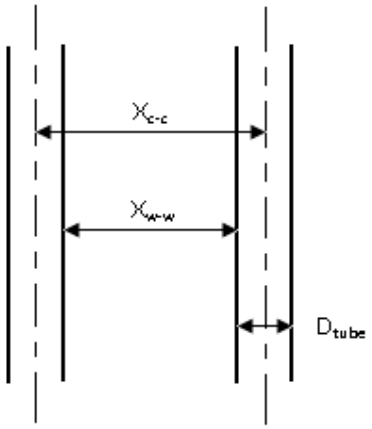

Figure 3.2 - Tube spacing parameters

Before calculating the number of straight sections, the battery edge to tube (a_{e-t}) distance needs to be selected. In this thesis, a_{e-t} will be 12mm.

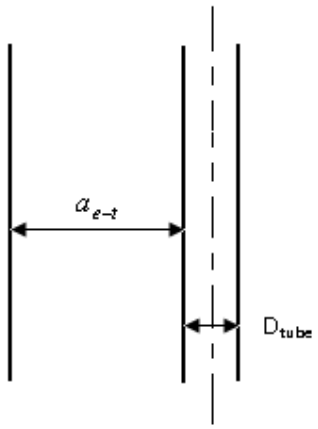

Figure 3.3 - Edge of battery to tube wall dimension

Since the overall length of the battery is known, this implies:

$$L_{batt} = (2 \times a_{e-t}) + (N_{tubes} \times D_{tube}) + (X_{w-w} \times N_{space}) \tag{3.2}$$

Equation (3.2) can be rearranged to solve for N_{space}, where N_{space} is the number of spaces between each straight section of tube, excluding the battery edge to tube spacing. N_{space} should be an odd number to ensure that the inlet and outlet of pipe will be arranged as shown in Figure 3.1. The number of straight tubing sections (N_{tube}) can be calculated by rearranging Equation (3.2) or Equation (3.3), because N_{tube} is typically 1 more than the N_{space}.

$$N_{tube} = N_{space} + 1 \tag{3.3}$$

With N_{tube} found, the number of curved paths (N_{curve}) in the cooling loop must be calculated.

$$N_{curve} = N_{space} - 1 \tag{3.4}$$

Now the total length of tubing on one layer for the battery module can be calculated by:

$$L_{tube,layer} = (N_{tube} \times L_{str}) + (N_{space} \times L_{curve}) \tag{3.5}$$

Where L_{curve} is the arc length of a single curved path with respect to the circumference (C) and radius (r_{curve}) of the curve:

$$L_{curve} = \frac{C}{2} \tag{3.6}$$

$$C = 2\pi\left(\frac{W_{c-c}}{2}\right) \tag{3.7}$$

The total length of tubing required for the entire battery module is dependent on the length of tubing on each layer and the number of cooling layers (N_{layer}) in the module.

$$L_{tube,total} = N_{layers} \times L_{tube,layer} \tag{3.8}$$

The assumptions made for the cooling fluid and battery module are given as follows.

- Each cooling layer is connected to a fluid distribution line (manifold) and not inter-connected with each other.
- Each layer of tubing has the same mass flow, therefore a common mass flow rate can be applied to the total length of tubing ($L_{tubing,total}$).
- Constant inlet temperature, density, specific heat, and kinematic viscosity is applied to the total length of the tube.

- The velocity of the fluid through the tubing is assumed based on the manifold design.
- Pressure loss through the curves must be found when calculating the overall pressure change in the tubing.
- Heat loss externally from the overall system is neglected (considered adiabatic).
- Inlet pressure into the battery module is assumed when it is the first component designed in the system.
- The internal surface of the tubing is assumed to be smooth.

Calculating the pressure drop in the battery module is important to analyze the fluid flow. The pressure drop in the battery module is denoted as ΔP_{bm}. ΔP_{bm} is determined by:

$$\Delta P_{bm} = f \frac{L_{total,tube}}{D_{tube}} \frac{V_f^{\,2}}{2g} + 2K_b \frac{V_f^{\,2}}{2g} \tag{3.9}$$

Where V_f is the assumed or known velocity of the fluid in the tube, g is gravity and f is the frictional factor. In SI units, g is equal to 9.81 m/s^2 or 32.3 $lbm.ft/s^2$ for English units. K_b is the loss coefficient through a bend. Depending on the type of bend, the corresponding K_b value can be found in a fluid mechanics textbook. In this thesis, all curves undergo a smooth 180^o bend. To calculate K_b, the ratio of the bend radius to the diameter of pipe must be found [32-33].

$$\frac{r}{D} = \frac{W_{c-c}}{D_{tube}} \tag{3.10}$$

With the ratio of r/D found, the corresponding value of K_b is found from either a graph or table in a fluid mechanics textbook. For this thesis, each curve is comprised of two 90° bends; therefore, for each curve, the K_b value must be doubled. If $P_{in,bm}$ is initially assumed or known from the design of a previous component (outlet pressure of the pump, refer to Figure 2.1), then $P_{out,bm}$ can be found from the following equation.

$$\Delta P_{bm} = P_{in,bm} - P_{out,bm} \tag{3.11}$$

The mass flow rate of the fluid can be found from the relation of fluid density, cross sectional area, and fluid velocity, shown in the following equation.

$$\dot{m}_f = \rho_f A_{c,tube} V_f \tag{3.12}$$

The value for the fluid density is found at the inlet temperature of the fluid into the battery module. $A_{c,tube}$ is the cross-sectional area of the selected tubing, which is found by

$$A_{c,tube} = \frac{1}{4}\pi D_{tube}{}^2 V_f \tag{3.13}$$

The frictional factor, *f*, is found by two methods, either laminar or turbulent flow through the tubes. If the flow is laminar, the Reynolds number is less than 3,000 which yields the following equation for *f* [34]:

$$f = \frac{64}{\mathrm{Re}} \qquad (\text{Laminar flow where } 0 < \mathrm{Re} < 3000) \tag{3.14}$$

For turbulent flow through tubes, the Reynolds number is greater than 3,000 and this yields the following equation for f [34]:

$$f = (0.790 \ln \mathrm{Re} - 1.64)^{-2} \text{ (Fully turbulent flow where } 3000 < \mathrm{Re} < 5 \times 10^6) \tag{3.15}$$

In both laminar and turbulent flow, the Reynolds number is calculated by:

$$\mathrm{Re} = \frac{D_{tube} V_f}{v_f} \tag{3.16}$$

Since the flowing fluid in the battery module will be gaining heat through convection from the batteries, the rate of heat transfer, Q, must be known or calculated through battery experiments. Once Q is found, the outlet temperature of the fluid from the module can be calculated by rearranging the energy equation.

$$Q = \dot{m}_f C_{p,f} \Delta T \tag{3.17}$$

$$Q = \dot{m}_f C_{p,f} (T_{out,f} - T_{in,f}) \tag{3.18}$$

$$T_{out,f} = T_{in,f} + \frac{Q}{\dot{m}_f C_{p,f}} \tag{3.19}$$

The calculation of the pressure drop and outlet temperature is necessary to find the entropy generation of the battery module. For a control volume of the system at steady-state, steady-flow, the rate of entropy generation is determined by:

$$\dot{S}_{gen} = -\sum \frac{\dot{Q}_{cv}}{T} + \sum \dot{m}_e s_e - \sum \dot{m}_i s_i \geq 0 \tag{3.20}$$

Where T is the ambient temperature, and s_e and s_i are the entropy at the exit and inlet, respectively. For internal flow through a channel, the entropy generation of a cross-section can be written as [31-35]

$$\dot{S}_{gen} = \frac{q\Delta T}{T^2} + \frac{\dot{m}}{\rho T}\left(-\frac{dP}{dx}\right) \tag{3.21}$$

Applying Equation (3.21) to the entire length of tubing through the battery module, the entropy generation becomes

$$\dot{S}_{gen} = \frac{Q(T_{out,f} - T_{in,f})}{T^2} + \frac{\dot{m}_f \Delta P}{\rho_f T_{in}} \tag{3.22}$$

With the equations outlined in this section, an entropy analysis can now be performed for the battery module. In this thesis, Table 3.1 outlines the initial parameters that will be used in the results chapter. For the fluid, all properties are found at the inlet temperature of the fluid. The Q value represents what one layer of tubing experiences under different battery loads. The total heat generation within the battery is not used because each layer of tubing is assumed to be experiencing the heat generation of one cell.

Table 3.1 - Initial Parameters

Item	Value
Tubing – Nylon, smooth surface	2 mm internal dia. 2.3 mm outside dia.
Tubing Conductivity	0.25 W/mK
Fluid – 50/50 Ethylene Glycol	-
a_{e-t}	12 mm
X_{w-w}	23 mm
X_{c-c}	25 mm
L_{str}	260 mm
Inlet pressure (assumed)	303975 Pa
Inlet Temperature (assumed)	298 K
Ambient Temperature (assumed)	305 K
Velocity	0.5 m/s
Q (4 scenarios)	3.5 Watts
	7.5 Watts
	15 Watts
	30 Watts

3.2 Heat Exchanger (Radiator)

The majority of automotive radiators are classified as a cross-flow unmixed tube-fin heat exchanger, which implies the two fluids flow perpendicular to each other and the fluids never have direct contact with each other. There are 2 types of configurations for the tubes (also called cores) in heat exchangers for automotive use, these are staggered and inline. As the names imply, a staggered tube arrangement means the tubes are offset from one another, whereas inline tube arrays have perfect rows and columns. The fins, which are classified as an extended surface area, can either be a continuous flat fin or waved fins. Before the analysis can be conducted, the following assumptions are made about the heat exchanger.

1. The heat exchanger operates under steady-state conditions, which means that the flow rate and temperature at the inlet of the heat exchanger are independent of time.

2. The heat exchanger operates under adiabatic conditions, therefore the heat loss to the surroundings is negligible. This includes no heat loss from the header tanks and hoses.
3. The fluid temperature is uniform over each cross section of the heat exchanger and classified as unmixed.
4. The thermal resistance of the tube and fin material is uniform over the entire heat exchanger.
5. Longitudinal conduction is negligible in the tube wall and fluid.
6. Heat transfer coefficients (individual and overall) are constant and independent of time, temperature and position.
7. Specific heat values and other fluid properties are assumed constant throughout the heat exchanger.
8. The extended surface efficiency, n_o, is uniform and constant across the entire exchanger.
9. The velocity and temperature are uniform and constant throughout the exchanger.
10. Inlet temperatures of both fluids are assumed or known.

This thesis will investigate the use of an inline tube array with waved fins. For the heat exchanger analysis, variables will be calculated on both fluid sides, with the fluids being air and a 50/50 solution of ethylene glycol and water. The method used to analyze the heat exchanger design is the number of heat transfer units method (NTU method). This analysis will allow for the heat exchanger effectiveness (ε) to be

found, which is important because with the heat exchanger effectiveness, the outlet temperatures of the two fluids can be found, given their inlet conditions.

3.2.1 Heat Exchanger Geometry

Descriptions of all geometrical parameters are described in this section. The parameters will be used in subsequent sections to complete the analysis. The orientation of the radiator and fluid flow in the vehicle is shown in Figure 3.4.

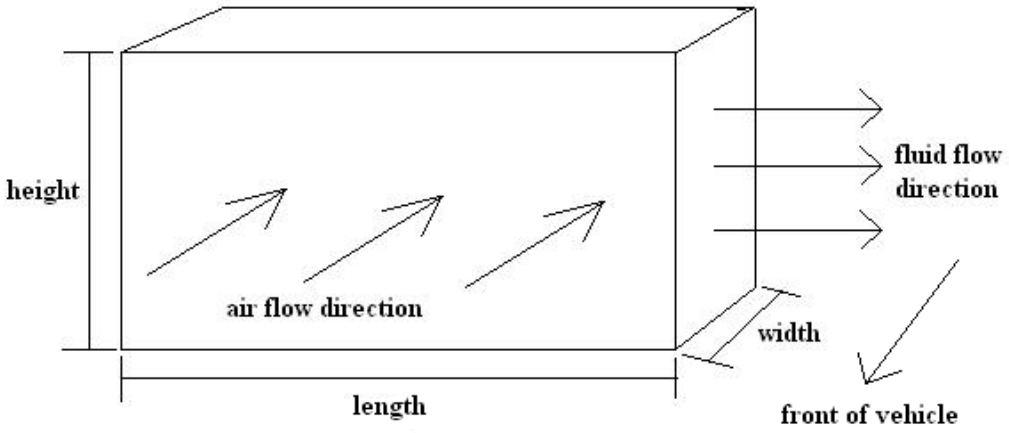

Figure 3.4 - Radiator orientation

Calculating the number of cores in the heat exchanger is based upon the physical size of the heat exchanger, and the size of core. Key parameters for this specific heat exchanger design are described below.

$$D_{h,core} = \frac{4A_{c,core}}{U_{core}} \qquad \text{Hydraulic diameter of core (one for inside and outside)} \qquad (3.23)$$

$$r_{h,core} = \frac{D_{h,core}}{4} \qquad \text{Hydraulic radius of core} \qquad (3.24)$$

$$N_t = \frac{W_{rad} H_{rad}}{X_t X_l}$$ Number of cores in the heat exchanger [36] (3.25)

Where W_{rad} and H_{rad} are the width and height of the radiator. X_t and X_l are the spacing of the cores in the transverse and longitudinal directions, respectively. The following parameters are found for the air and fluid sides of the heat exchanger.

Air side

$$A_{fr,a} = H_{rad} L_{rad}$$ Frontal area (3.26)

$$\alpha = \frac{A}{V_{rad}}$$ Surface area density (3.27)

$$\sigma = \frac{X_t - D_{h,core,out}}{X_t}$$ Free flow area to frontal area (3.28)

$$A_{o,air} = \sigma A_{fr,a}$$ Minimum free flow area (3.29)

Fluid Side

$$A_{fr,f} = W_{rad} H_{rad}$$ Frontal area (3.30)

$$\alpha = \frac{A}{V_{rad}}$$ Surface area density (3.31)

$$\sigma = \frac{\left(\frac{\pi D^2_{h,core,in}}{4}\right)}{X_t X_l}$$ Free flow area to frontal area (3.32)

$$A_{o,f} = \left(\frac{\pi D^2_{h,core,in}}{4}\right) N_t$$ Minimum free flow area (3.33)

In both the air and fluid side calculations, A and V_{rad} represent the total heat transfer surface area and total radiator volume, respectively.

3.2.2 Fins

There are two types of fins that can be used in automotive heat exchangers, which are flat continuous fins and waved fins. Each type of fin has properties which make them advantageous in certain scenarios. An example of waved fins can be used for an inline array of cores, because the manufacturability of this setup is relatively simple and cost effective. Waved fins are harder to implement in staggered arrays because it is harder to assemble in manufacturing, which explains why flat continuous fins are used in staggered arrays. The benefit of using an inline array of cores is that both waved and flat fins can be implemented. As explained in the previous section, this thesis investigates the overall effectiveness of the radiator with waved fins. A cross-sectional view of each type of fin is shown in Figure 3.5 [37].

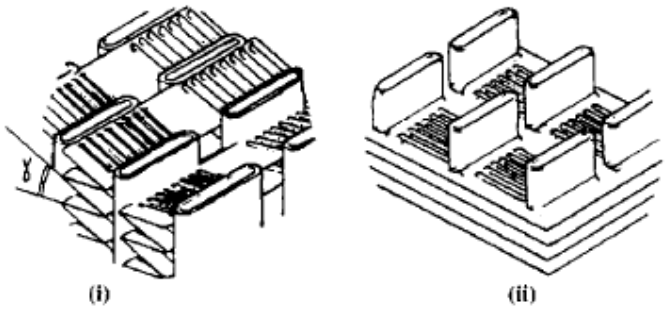

Figure 3.5 - (i) Waved fins and (ii) continuous fins for an inline configuration [37]

For flat continuous fins, the geometry is simplified to a rectangular plate with a specified length, width, height and spacing between fins. To calculate the surface area for a continuous fin, the area on each side is found. The area occupied by the cores is subtracted, then multiplied by the number of fins. For waved fins, the geometry for each fin is shown in Figure 3.6.

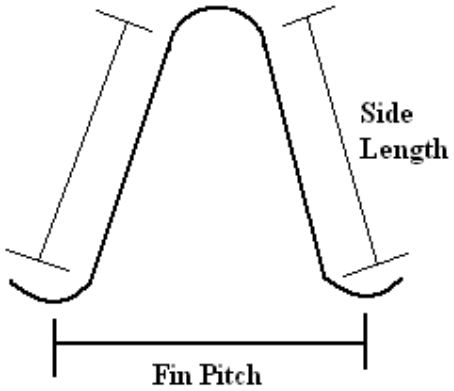

Figure 3.6 - Waved Fin geometry with fin pitch and side length

To calculate the surface area for a waved fin, the total length of the waved fins on one row needs to be identified. To calculate the total length on one row, the length of an individual fin can be approximated by multiplying the side length by two.

$$L_{fin} = 2 \times L_{fin,side} \tag{3.34}$$

The length per fin is then multiplied by the number of fins on one row to determine the total length per row,

$$length/_{row} = L_{fin} \times N_{fin/row} \tag{3.35}$$

To calculate the surface area of one row, it is easier to consider a row of waved fins stretched out to create a large rectangle, because the total length per row has been found and the width of the fin is known. Once the surface area for one row is found, it is then multiplied by the number of fin rows to find the total fin surface area.

3.2.3 Heat Transfer Equations

The following equations are used for the heat transfer analysis of the radiator. The equations are expressed for the air and fluid side [38].

Air side

- Heat capacity rate

$$C_a = \dot{m}_a C_{p,a} \tag{3.36}$$

- Heat transfer coefficient

$$h_a = \frac{j_a G_a C_{p,a}}{\mathrm{Pr}_a^{2/3}} \tag{3.37}$$

$$G_a = \frac{\dot{m}_a}{A_{o,a}} \tag{3.38}$$

$$\mathrm{Re}_a = \frac{G_a D_{h,air}}{\mu_a} \tag{3.39}$$

$$j_a = \frac{0.174}{\mathrm{Re}_a^{0.383}} \tag{3.40}$$

- Fin efficiency

$$n_f = \frac{\tanh(ml)}{ml} \tag{3.41}$$

$$m = \sqrt{\frac{2h_a}{k_{fin}\delta}} \tag{3.42}$$

- Effectiveness

$$n_0 = 1-(1-n_f)\frac{A_{fr,a}}{A} \tag{3.43}$$

- Pressure drop (without expansion and contraction coefficients)

$$\Delta P_a = \frac{P_{in,a}G_a^{\,2}}{P_{in,a}\rho_{in,a}}\left[\begin{array}{l}\left(1-\sigma_a^{\,2}\right)+2\left\{\dfrac{\rho_{in,a}}{\rho_{out,a}}-1\right\}+\left(\dfrac{fW_{rad}\rho_{in,a}}{r_{h,air}}\right)\left(\dfrac{1}{\rho_m}\right)\\ -\left(1-\sigma_a^{\,2}\right)\left(\dfrac{\rho_{in,a}}{\rho_{out,a}}\right)\end{array}\right] \tag{3.44}$$

$$f = \frac{0.3778}{\mathrm{Re}_a^{\,0.3565}} \tag{3.45}$$

$$\frac{1}{\rho_m} = \frac{1}{2}\left(\frac{1}{\rho_{in,a}}+\frac{1}{\rho_{out,a}}\right) \tag{3.46}$$

Fluid side

- Heat capacity rate

$$C_f = \dot{m}_f\, C_{p,f} \tag{3.47}$$

- Heat transfer coefficient

$$h_f = \frac{Nu\times k_{core}}{D_{h,core,in}} \tag{3.48}$$

$$Nu = 0.023\mathrm{Re}_f^{\,0.8}\,\mathrm{Pr}_f^{\,0.3} \tag{3.49}$$

$$\mathrm{Re}_f = \frac{G_f D_{h,core,in}}{\mu_f} \tag{3.50}$$

$$G_f = \frac{\dot{m}_f}{A_{o,f}} \tag{3.51}$$

- Pressure drop on the fluid side

$$\Delta P_f = f \frac{L_{core}}{D_{h,core,in}} \frac{\rho_{in,f} V_{in.f}^{\ 2}}{2} \tag{3.52}$$

$$f = \frac{64}{\mathrm{Re}} \quad \text{(Laminar flow where } 0 < \mathrm{Re} < 3000\text{)} \tag{3.14}$$

$$f = (0.790 \ln \mathrm{Re} - 1.64)^{-2} \quad \text{(Turbulent flow where } 3000 < \mathrm{Re} < 5 \times 10^6\text{)} \tag{3.15}$$

$$V_{in,f} = \frac{\dot{m}_f}{\rho_{in,f} A_{c,core}} \tag{3.53}$$

3.2.4 Heat Exchanger Effectiveness

Heat exchanger effectiveness, ε, is how the thermal performance of a heat exchanger is measured. For any flow arrangement of a heat exchanger, the effectiveness is defined as the actual heat transfer rate from the hot fluid to the cold fluid, over the maximum heat transfer rate possible [36].

$$\varepsilon = \frac{q}{q_{\max}} \tag{3.54}$$

Before the effectiveness can be solved, the actual heat transfer rate, q, must be solved. The heat transfer rate is equal to:

$$q = UA\Delta T \tag{3.55}$$

where U is the overall heat transfer coefficient, A is the overall heat transfer surface area, and ΔT is the change of temperature of the hot fluid entering the heat exchanger

to the cold fluid entering the exchanger. In order to solve q, the overall heat transfer coefficient needs to be calculated as follows,

$$\frac{1}{UA} = \frac{1}{(n_o h_a A)} + \frac{\ln\left(\frac{D_{h,core,out}}{D_{h,core,in}}\right)}{2\pi k_{core} L_{core} N_t} + \frac{1}{(n_o h_f A)} \tag{3.56}$$

The above equation can then be used with Equation (3.55) to solve for q. However, the effectiveness value must still be solved, and for crossflow heat exchangers with unmixed fluids, the effectiveness is defined as:

$$\varepsilon = 1 - \exp\left[\frac{NTU^{0.22}}{C^*}\left\{\exp\left(-C^* NTU^{0.74}\right) - 1\right\}\right] \tag{3.57}$$

where NTU is the number of heat transfer units and C^* is the heat capacity ratio. The equations for both terms are shown as follows.

$$C^* = \frac{C_{\min}}{C_{\max}} = \frac{C_f}{C_a} \tag{3.58}$$

$$NTU = \frac{UA}{C_{\min}} \tag{3.59}$$

The effectiveness can also be found graphically with a calculated NTU and C^* for cross-flow unmixed fluids as shown in Figure 3.7 [36].

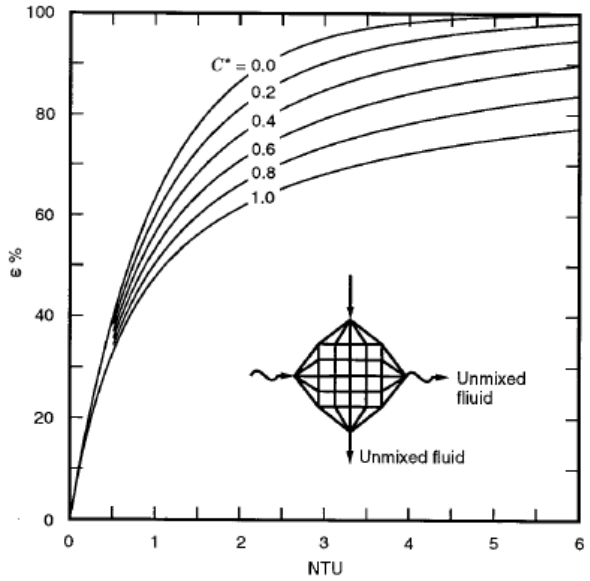

Figure 3.7 - Effectiveness, ε, as a function of NTU and C* [36]

Based on the effectiveness and heat transfer rate, Equation (3.54) can be rearranged to find q_{max}:

$$q_{\max} = \varepsilon \times q \tag{3.60}$$

The maximum heat transfer allows for the calculation of the outlet temperatures of both the air and fluid, which will be needed for the entropy generation analysis.

$$T_{out,a} = T_{in,a} + \frac{q_{\max}}{C_f} \tag{3.61}$$

$$T_{out,f} = T_{in,f} - \frac{q_{\max}}{C_f} \tag{3.62}$$

3.2.5 Heat Exchanger Entropy Generation

Since the radiator handles two fluids, air and liquid, it is necessary to calculate the change of entropy for each fluid. The change of entropy for the air and liquid are then added together to find the total entropy generation for the system. For the change of entropy on the air side, there are losses associated with heat transfer irreversibility and frictional loses [39].

$$\dot{S}_{gen} = -\int_1^2 \frac{\dot{Q}_{cv}}{T} + \dot{m}(s_2 - s_1) \tag{3.63}$$

where $s_e = s_2$ and $s_i = s_1$. Relating the entropy change to the specific heat and temperature change yields:

$$(s_2 - s_1) = \int \frac{du}{T} = \int C \frac{dT}{T} \approx C \ln \frac{T_2}{T_1} \tag{3.64}$$

The above equation is simplified to

$$\Delta S_a = \dot{m}_a c_{p,a} \ln \frac{T_{out,a}}{T_{in,a}} \tag{3.65}$$

Including the frictional and pressure losses, Equation (3.65) becomes

$$\Delta S_a = \dot{m}_a c_{p,a} \ln \frac{T_{out,a}}{T_{in,a}} + \frac{\dot{m}_a (P_{in,a} - P_{out,a})}{\rho_a T_{in,a}} \tag{3.66}$$

Similarly, for the hot fluid, the change of entropy is equal to

$$\Delta S_f = \dot{m}_f c_{p,f} \ln \frac{T_{out,f}}{T_{in,f}} \tag{3.67}$$

Adding the frictional and pressure losses to Equation (3.77) yields

$$\Delta S_f = \dot{m}_f c_{p,f} \ln \frac{T_{out,f}}{T_{in,f}} + \frac{\dot{m}_a (P_{in,f} - P_{out,f})}{\rho_f T_{in,f}} \tag{3.68}$$

Therefore, the overall entropy generation becomes

$$\dot{S}_{gen} = \Delta S_a + \Delta S_f \tag{3.69}$$

In Equation (3.69), ΔS_a will have a positive value while ΔS_f will be negative because the air will be rising in temperature while the fluid will be cooling down. However, the net sum is positive, in accordance with the Second Law.

For the air ΔS_a :

$$\dot{m}_f c_{p,f} \ln \frac{T_{out,f}}{T_{in,f}} > 0 \tag{3.70}$$

For the fluid ΔS_f :

$$\dot{m}_f c_{p,f} \ln \frac{T_{out,f}}{T_{in,f}} < 0 \tag{3.71}$$

For the radiator used in this thesis, Table 3.2 summarizes the initial values that will be used to calculate the results in upcoming chapters.

Table 3.2 - Radiator Initial Parameters

Item	Value
Length (L_{rad})	0.66675m
Height (H_{rad})	0.34925m
Width (W_{rad})	0.03175m
Core length (L_{core})	0.34925m
Core width (W_{core})	0.01295m
Core wall thickness (δ)	$3x10^{4}$m
X_t	0.0101m
X_l	0.0171m
Core material	Aluminum
Fin material	Aluminum
Number of rows	2
Fin length (L_{fin})	0.0163m
Fin thickness (δ_{fin})	$1x10^{4}$m
Fin pitch (Pt_f)	3mm
Air inlet temperature ($T_{in,a}$)	298 K
Fluid - 50/50 Eth. Gyl. ($T_{in,f}$)	323 K
Air inlet pressure ($P_{in,a}$)	101 kPa
Fluid - 50/50 Eth. Gyl. ($P_{in,f}$)	218 kPa
Mass flow rate – air	1.4 kg/s
Mass flow rate – fluid	0.75 kg/s

3.3 Pump

For an ICE, the pump is attached to the engine block and the impeller is connected by a belt to the engine's pulley system, as shown in Figure 3.8 [40] .

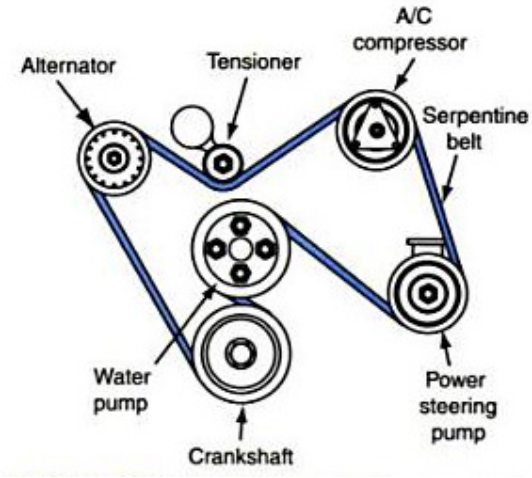

Figure 3.8 - Engine pulley system [40]

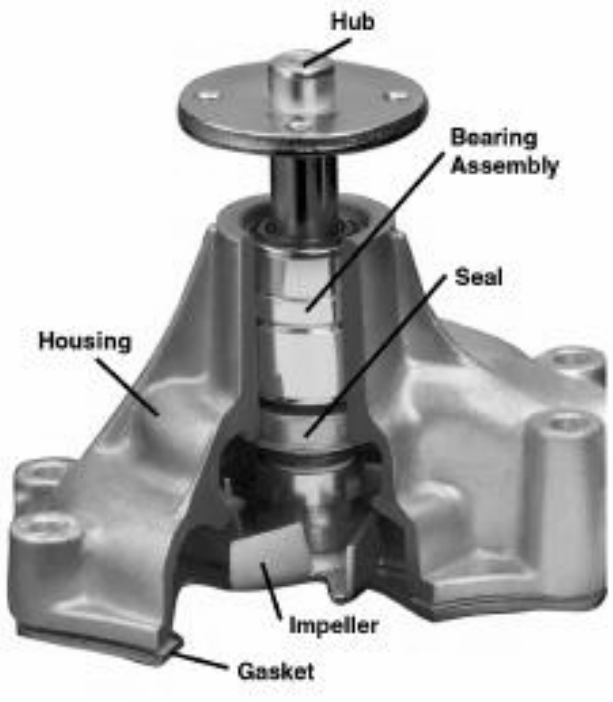

Figure 3.9 - Belt driven water pump [41]

Figure 3.9 [41] above is a cutaway of a typical belt driven automotive water pump. The pump in Figure 3.9 is classified as a centrifugal pump, which is the type investigated in this thesis. The data is typically supplied by the manufacturer in the form of a pump head vs. flow rate graph. Pump head (H_p) refers to the maximum pressure the pump is capable of producing, measured in either feet (ft) or psi. The flow rate (Q_p) is the maximum amount of fluid displaced within a given time, usually given in gallons per minute (GPM). Figure 3.10 [42] shows an example of the graph typically supplied by the manufacturer.

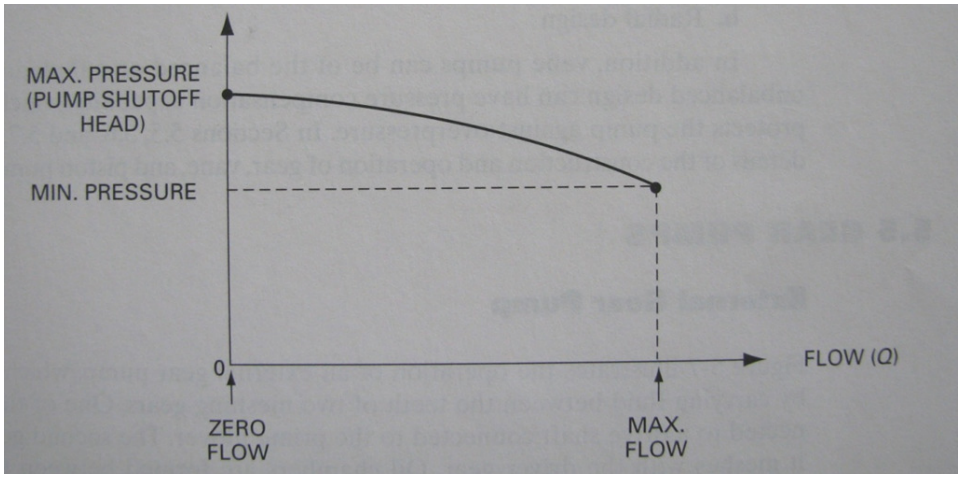

Figure 3.10 - Relationship of pump head and flow rate [42]

The efficiency of the pump (η_{pump}) is also normally given by the manufacturer. This is important because various operating conditions have a direct impact on a pump's durability and lifespan [43]. Pump efficiency can be plotted on the same graph as the head vs. flow rate graph as shown in Figure 3.11 [43].

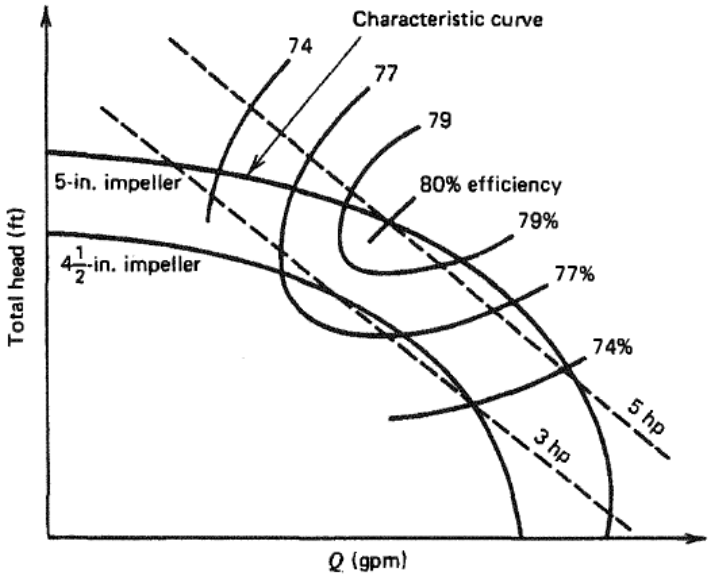

Figure 3.11 - Pump efficiency curves [43]

Figure 3.11 shows for a given impeller diameter, the efficiency and power required to operate the pump under various conditions will change. Pumps typically have an efficiency in the range of 15-90% [43], which is dependent upon the design of the pump. An electronic water pump operates under the same principle as above, except instead of a pulley system turning the impeller, it is controlled by a 12 Volt DC motor. Using an electronic water pump offers certain advantages over a belt driven pump. The main advantage is the pump power is not wasted as the engine operates at higher speeds, hence electronic pumps have a lower flow rate rating.

This thesis will investigate the entropy generation in an electronic water pump with the equations outlined below. All units are initially calculated in English units, with final values converted to metric. The pump analyzed in this thesis is the E389A EMP Electronic 12V Water Pump, manufactured by Stewart Components. The pump data shown in Figures 3.12 and 3.11 are provided by Stewart Components [44].

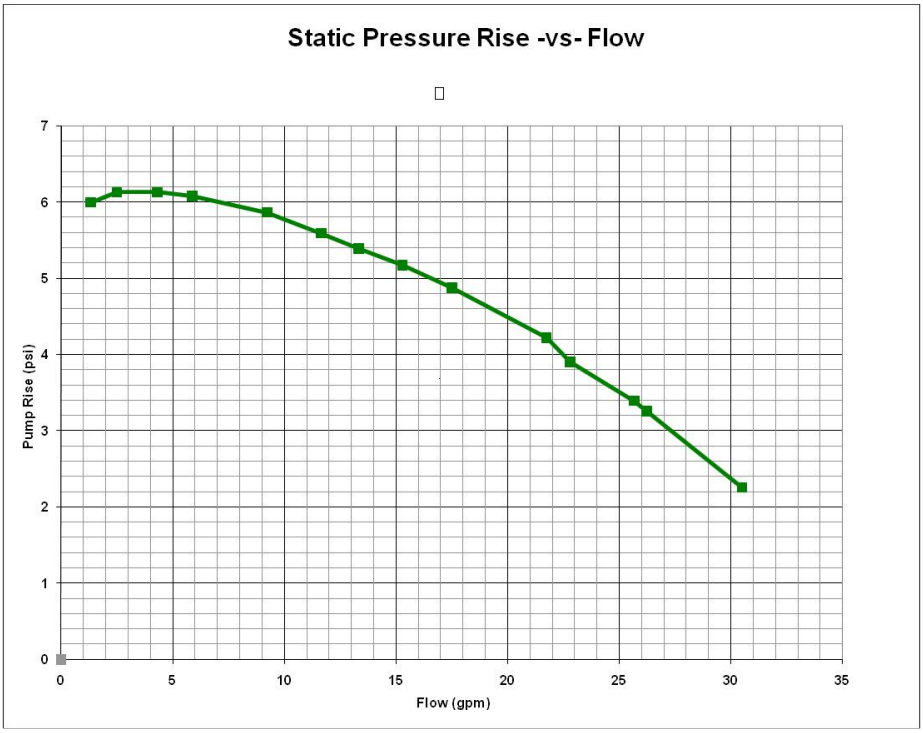

Figure 3.12 - E389A pressure versus flow [44]

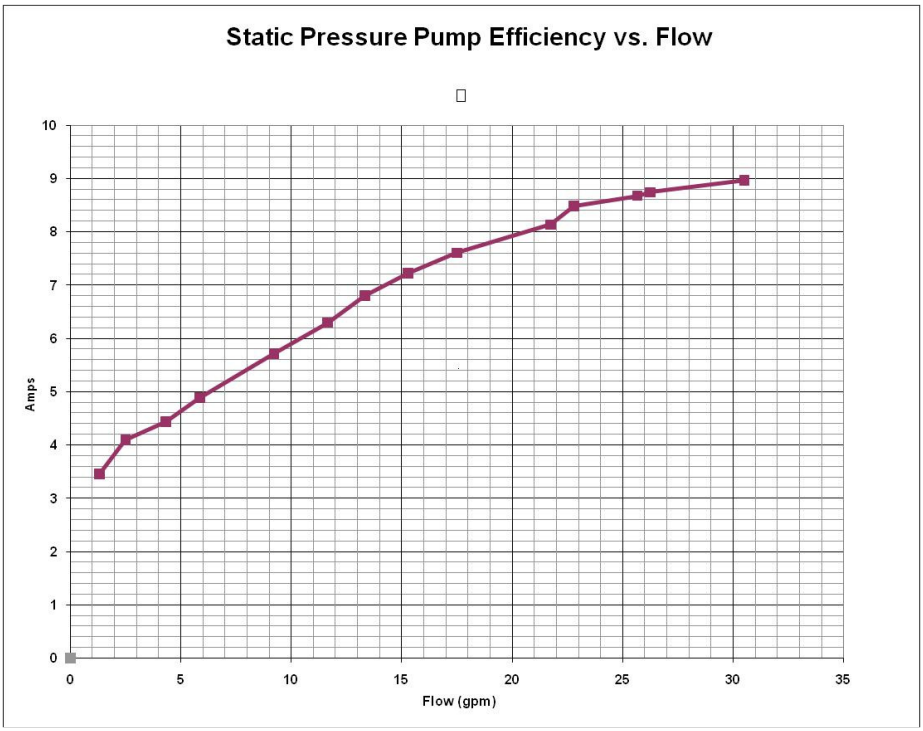

Figure 3.13 - E389A current versus flow [44]

The power can be calculated at any point from the pressure vs. flow curve, using the following equation.

$$Pw_p = \frac{H_p Q_p}{1714} \tag{3.72}$$

where power is found in horsepower (HP), head (H_p) in PSI, and flow (Q_p) in GPM. The efficiency curve is interpolated from the two graphs provided. For electric pumps, the efficiency is defined as:

$$\eta_{pump} = \frac{Pw_p}{Pw_e} \tag{3.73}$$

where Pw_e is the electric power provided by the motor. Since the graph in Figure 3.13 is Amps vs. Flow, this means that the electrical power can be calculated at any flow rate. Electrical power in Watts is defined as:

$$Pw_e = Amps \times Voltage \tag{3.74}$$

For the pump efficiency, the units for the pump power and electrical power must be the same. Horsepower can be converted into Watts using the following conversion:

1 HP ≈ 746 Watts

Using the above equations, the following table and efficiency graphs were created for the E389A pump.

Table 3.3 - Power and Efficiency of E389A Pump

Pump Fluid Power				Pump Electrical Power			
Head (psi)	Flow (GPM)	HP	Watts	Amps	Flow (GPM)	Watts	Efficiency
6	1.2	0.004	3.13	3.45	1.2	41.48	7.55
6.129	2.4	0.009	6.39	4.09	2.4	49.09	13.03
6.129	4.2	0.015	11.19	4.43	4.2	53.20	21.04
6.081	5.9	0.021	15.60	4.88	5.9	58.63	26.62
5.865	9.2	0.031	23.47	5.70	9.2	68.49	34.27
5.591	11.7	0.038	28.45	6.29	11.7	75.52	37.68
5.393	13.2	0.042	30.97	6.79	13.2	81.58	37.96
5.171	15.3	0.046	34.42	7.22	15.3	86.66	39.71
4.876	18.5	0.053	39.24	7.60	18.5	91.24	43.01
4.221	21.8	0.054	40.03	8.13	21.8	97.60	41.01
3.905	22.9	0.052	38.90	8.48	22.9	101.82	38.21
3.393	25.6	0.051	37.79	8.66	25.6	104.01	36.33
3.254	26.1	0.049	36.94	8.74	26.1	104.89	35.22
2.255	30.5	0.040	29.92	8.99	30.5	107.95	27.71

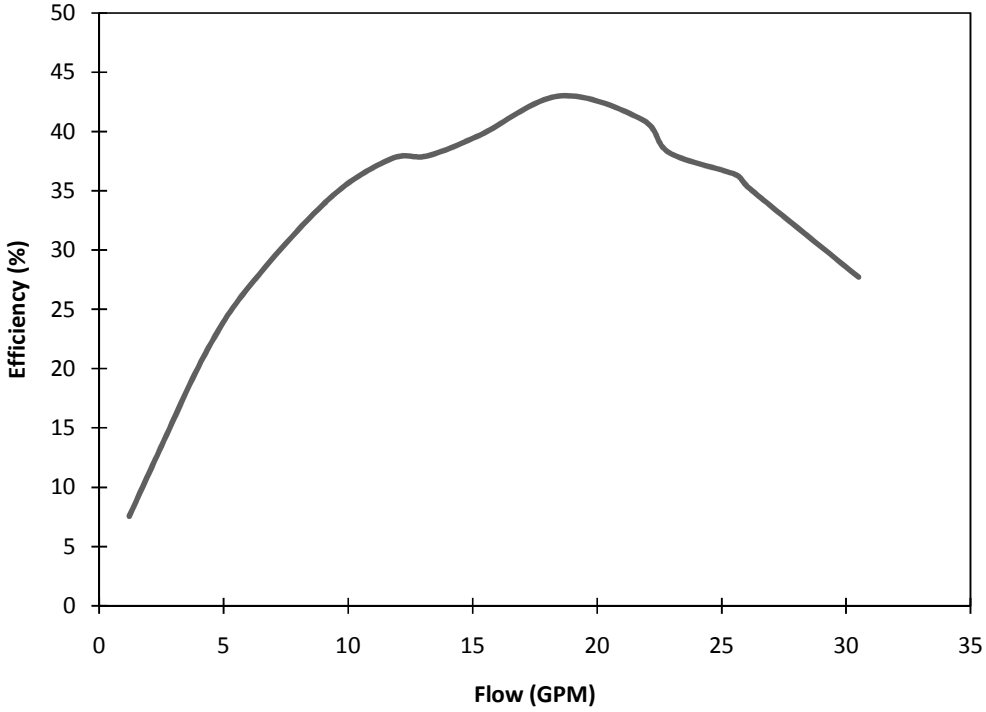

Figure 3.14 - E389A pump efficiency curve

The power and efficiency of the pump are required to calculate the entropy generation. Also, the pressure drop across the pump must be found. For the pump, the pressure drop is the difference between the ideal and real head pressures [31]. The pressure drop across the pump for any flow rate is defined as:

$$\Delta P_{pump} = P_{head,i} - P_{head,r} \tag{3.75}$$

$$\Delta P_{pump} = \frac{Pw_p \times \rho_f}{\dot{m}_f} - \frac{Pw_p \times \rho_f \times \eta_{pump}}{\dot{m}_f} \tag{3.76}$$

To find the entropy generation of the pump,

$$\dot{S}_{gen,p} = \frac{\dot{m}_f \, \Delta P_{pump}}{\rho_f T_{in}} \tag{3.77}$$

3.4 Throttle

Since the throttle is a measure of the losses of all connecting lines with no heat transfer between them, the entropy generation is defined as the frictional losses through a pipe. The equation is defined below:

$$\dot{S}_{gen,t} = \frac{\dot{m}_f \Delta P_t}{\rho_f T_{in}} \tag{3.78}$$

Here ΔP would be the losses in the lines from the outlet of the pump to the inlet of the radiator, which is also equal to the pressure loss within the battery module.

CHAPTER 4 - MODEL VALIDATION

Validation of the models developed in this thesis will be examined in this chapter, by examining the fluid flow in the tubes through the battery module, as well as the heat exchanger design, against published values. This serves to ensure that the model has been developed correctly and assumptions reflect the real world.

4.1 Internal Flow

Since there is fluid flow in the battery module with heat transfer, it is important to verify that the model satisfies the proper entropy generation characteristics as outlined previously by Bejan [21]. Bejan has shown that there is an optimum value in which entropy is generated equally by the losses due to friction and heat transfer. The model by Bejan calculates a minimum S_{gen} for the fluid based upon the Reynolds number (Re), as well as an optimal Re. The Re is specifically directed towards the shape of the conduit. In this thesis, it is a round tube. Bejan's plot is shown in Figure 4.1.

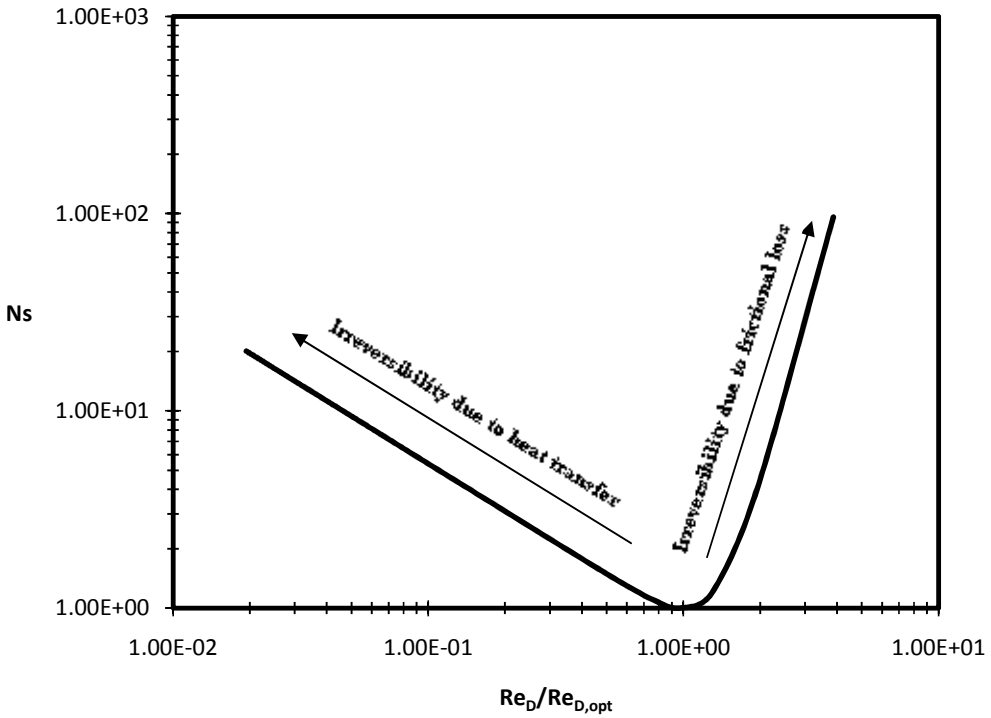

Figure 4.1 - Entropy generation rate in a smooth tube

The non-dimensional entropy generation number (N_s) is found by dividing S_{gen} by $S_{gen,min}$, as outlined by Bejan (21). For the entire battery module, 4 different heat generation values were considered, 50W, 100W, 300W and 400W. These values represent a range of heat generation values that the battery box may experience through various operations. When heat generation values and tubing dimensions are applied to Bejan's model, Figure 4.2 shows the validation of the predicted results for battery module internal flow.

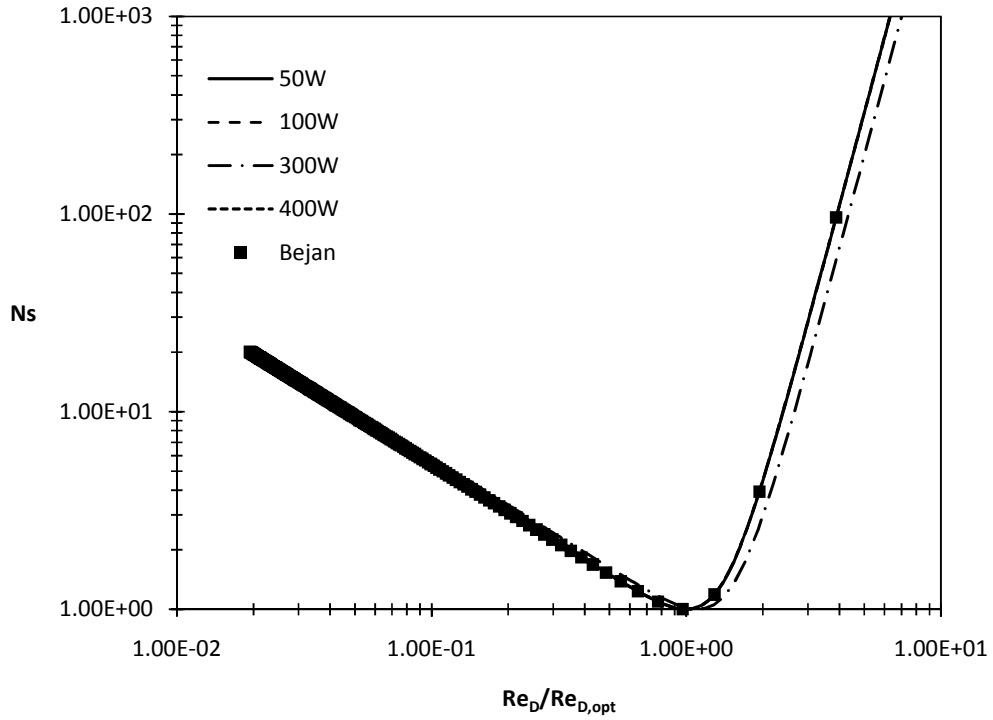

Figure 4.2 - Battery module internal flow verification

From Figures 4.1 and 4.2, it can be seen that the optimum point occurs when the N_s and $Re_D/Re_{D,opt}$ values are 1. Any values greater than 1 on the x-axis mean that the S_{gen} due to frictional losses is higher than the S_{gen} due to heat transfer losses. The opposite is true for values less than 1 on the x-axis. S_{gen} due to heat transfer losses is higher than S_{gen} due to frictional losses.

4.2 Heat Exchanger Operating Conditions

The heat exchanger model was developed from first principle equations outlined for the heat exchanger design. Heat exchangers can be rated by different parameters, such as the effectiveness (ε), number of heat transfer units (NTU), or the heat capacity ratio (C). Past data by Ramesh [36] states that for an automotive radiator, the NTU and effectiveness are NTU ≈ 0.5 and ε ≈ 0.4.

For the heat exchanger model in this thesis, the NTU and ε were verified against the pump operating flow rates using 50/50 of water and ethylene glycol. Table 4.1 shows the results.

Table 4.1 - Heat Exchanger Operating Values

Pump Flowrate (kg/s)	Effectiveness	NTU
0.08	0.34	0.42
0.16	0.34	0.43
0.29	0.35	0.45
0.39	0.35	0.46
0.61	0.36	0.49
0.78	0.36	0.5
0.88	0.36	0.52
1.02	0.36	0.53
1.23	0.36	0.53
1.45	0.36	0.57
1.52	0.36	0.58
1.70	0.36	0.6
1.74	0.36	0.6
2.03	0.37	0.63
Average	**0.36**	**0.52**

From Table 4.1, the average values for the effectiveness and NTU is agree well with past data by Ramesh [36].

4.3 Heat Exchanger Pressure Drops

Since the heat exchanger cools two fluids which are moving at different flow rates, it is important to ensure that both fluids are flowing within reasonable limits. Measuring the pressure drop of both fluids is one way to examine the fluid flow, since the pressure is dependent on flow channel dimensions, velocity and temperature. Oliet et al. [45] conducted a parametric study of an automotive radiator and part of the study included the pressure drop of the air and liquid. Oliet et al. [45] developed a

radiator model differently than the one developed in this thesis. To verify against the past data of Oliet et al., the results will be normalized for comparison purposes. The pressure was normalized for Oliet's data, as well as the data generated in this thesis. The radiator dimensions and operation temperatures in the Oliet study were applied to the radiator in this thesis, and it produced the following results

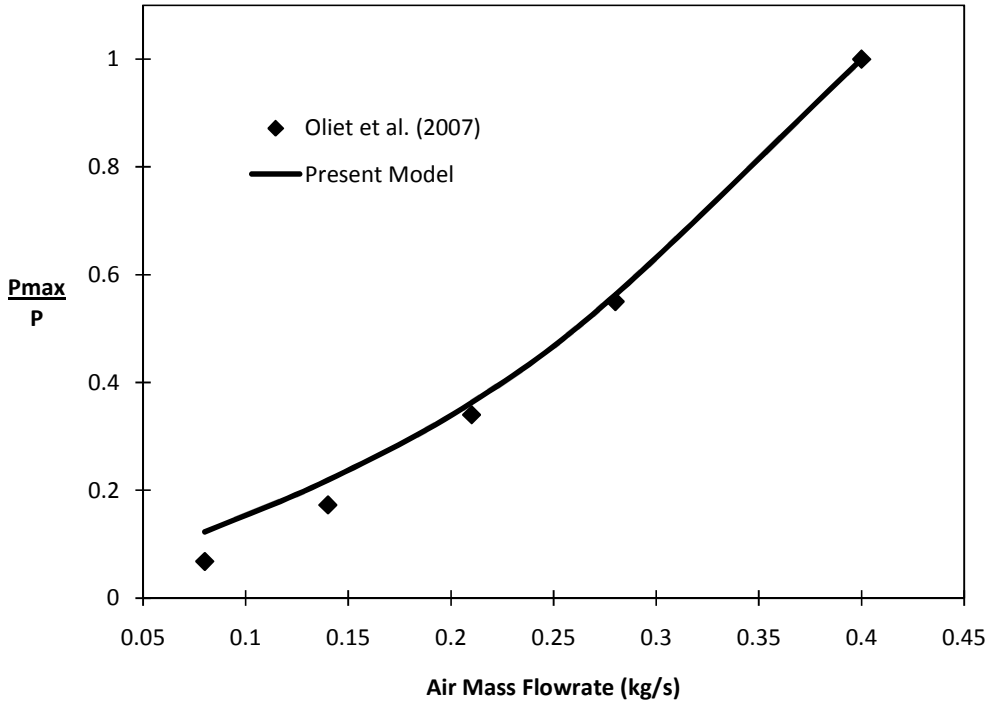

Figure 4.3 - Pressure drop across the air side of the radiator

The maximum pressure in each model was divided by each individual pressure in Figure 4.3 to normalize the data, while the air mass flow rate was the same in each model.

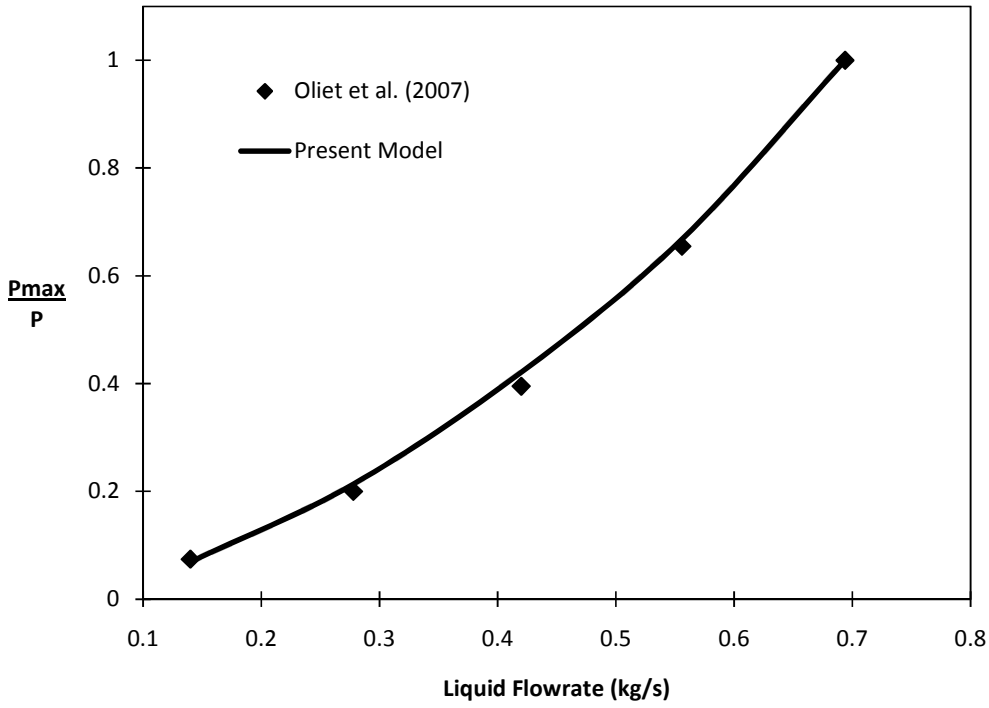

Figure 4.4 - Pressure drop across the liquid side of the radiator

Both Figures 4.3 and Figure 4.4 show that the normalized pressure vs. flow rates has generated similar results compared to Oliet's data. This suggests that the heat exchanger model developed in this thesis has been implemented correctly.

4.4 Heat Transfer Analysis between Battery and Tube

While this thesis has assumed a Q value reflecting various operating conditions, it is important to note that in real world applications, the Q value depends on the electrical input and the temperature of the cell. The following model aims to show that the Q values assumed in this thesis are reasonable and the temperature difference between

the cell and moving fluid is also reasonable. All calculations based in this section are detailed in the Appendix.

4.4.1 Natural Convection Model

Examining the model as a flat horizontal plate with a heat source will show the effects of natural convection in the air gap between the cells. Figure 4.5 is an illustration of the convection model.

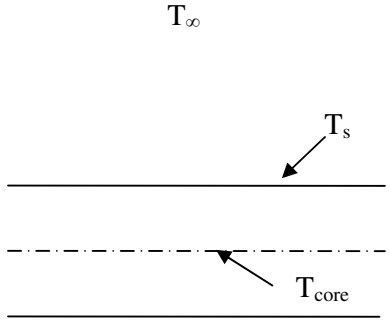

Figure 4.5 - Natural convection model

For a cell operating condition of 80A, with a resistance of 0.43mΩ, the heat generated is equal to the heat dissipated.

$$P = \dot{q} \tag{4.1}$$

$$I^2 R = h_{overall} A(T_s - T_\infty) \tag{4.2}$$

The core temperature of the cell (T_{core}) can be found by:

$$T_{core} = \frac{\dot{q} L^2}{2k_{cell}} + T_s \tag{4.3}$$

where L is the distance from the core to the surface and k_{cell} is equal to 1 W/mK. Solving for T_{core} shows the temperature difference between the core and surface is approximately 4.53°C. Looking at the model as a relationship between flat plates with small spaces, the following relationship is determined:

$$\frac{k_{eff}}{k} = C(Gr\,\mathrm{Pr})^n \left(\frac{L}{\delta}\right)^m \tag{4.3}$$

$$Gr = \frac{g\beta(T_1 - T_2)\delta^3}{v^2} \tag{4.4}$$

where β is the film temperature and δ is the characteristic length. The Prantl number (Pr) and kinematic viscosity (v) are found at the film temperature. Solving Equation (4.3),

$$\frac{k_{eff}}{k} = 1$$

This implies that the effects due to convection are negligible and conduction is dominant [46].

4.4.2 Heat Transfer Model

This section will examine the heat transfer between the cell and fluid inside the tube by creating a parallel resistance network. Figure 4.6 shows a cross sectional view of the tube placed between two cells.

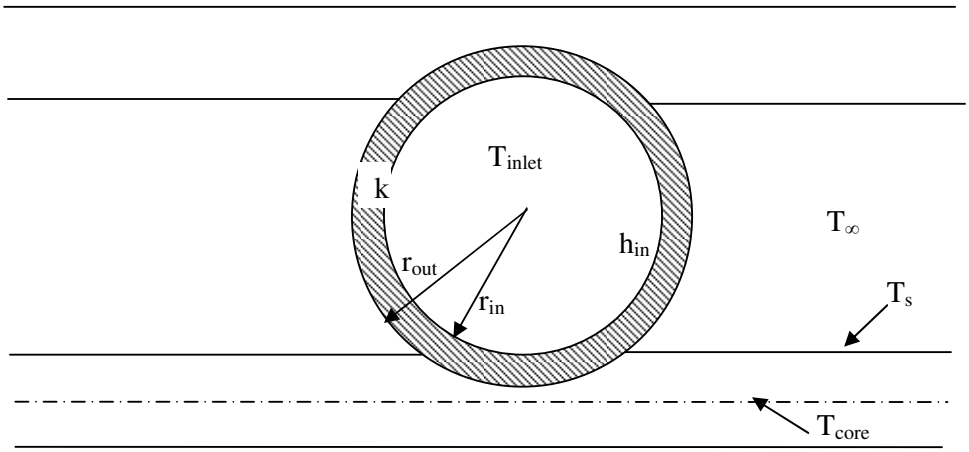

Figure 4.6 - Tube and cell configuration

For the tube placed between two cells, key parameters will need to be calculated, including, the percentage of the tube exposed in the air gap, the percentage of the tube in contact with the cell, and the heat transfer coefficient (h_{in}).

4.4.3 Conduction Model with Air Gap

The conduction model and network with an air gap are represented in Figure 4.7 and Figure 4.8.

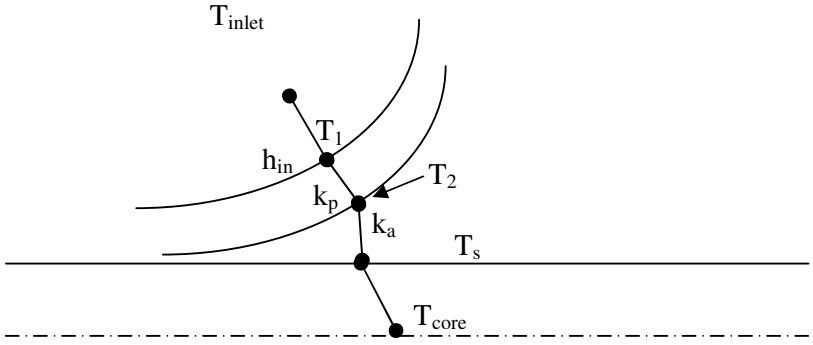

Figure 4.7 - Conduction model with air gap

Figure 4.8 - Resistance network with air gap

From Figure 4.8, the total resistance can be found by:

$$R_{total1} = \frac{1}{h_{in}A} + \left[\frac{\ln\left(\frac{r_{out}}{r_{in}}\right)}{2\pi L_{tube}k} \times (air\%) \right] + \left(\frac{\delta}{kA} \times air\% \right) \tag{4.5}$$

Solving Equation (4.5) yields a resistance of 3.44 K/W.

4.4.4 Conduction Model

The conduction model is shown in Figure 4.9 and the resistance network is shown in Figure 4.10.

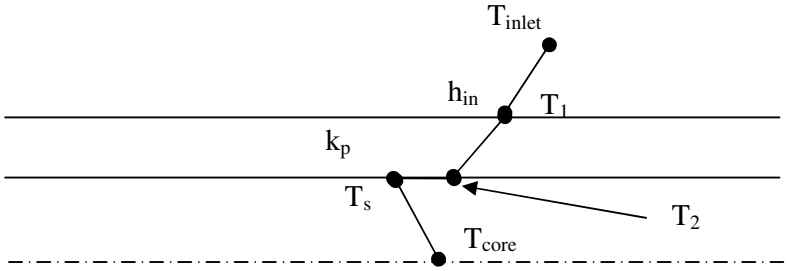

Figure 4.9 - Conduction model

Figure 4.10 - Conduction resistance network

The contact resistance between T_2 and T_s is defined in [47] as:

$$R_c = \frac{0.565 H_{mic} \frac{s_r}{s_s}}{k_s P A_a} \tag{4.6}$$

The total resistance for the conduction model is equal to

$$R_{total2} = \frac{1}{h_{in} A} + \left(\frac{\ln\left(\frac{r_{out}}{r_{in}}\right)}{2\pi L_{tube} k} \times (contact\%) \right) + R_c \tag{4.7}$$

Solving Equation (4.7) yields a resistance of 37.51 K/W.

4.4.5 Temperature Difference of Fluid and Cell

With the resistance values calculated, the temperature difference between the cell and fluid in the tube can be found, as follows.

$$\dot{q} = \frac{(T_s - T_{inlet})}{R_{overall}} \tag{4.8}$$

where $R_{overall}$ is the combined values of R_{total1} and R_{total2}:

$$R_{overall} = \frac{R_{total1} R_{total2}}{R_{total1} + R_{total2}} \tag{4.9}$$

Rearranging Equation (4.8) to solve for (T_s-T_{inlet}), the change in temperature between the cell and fluid becomes 13.2^{o}C. Throughout the analysis in this section, the high value of the contact resistance (R_c) contributes to the ΔT of the cell and fluid temperature. If the contact resistance is reduced, by increasing the contact force by a factor of 10, the change in temperature is reduced to 9.6^{o}C. If the use of thermal paste is included between the tube and surface of the cell, the change in temperature is further reduced to 7.3^{o}C. This suggests the heat transfer effects between the cell and fluid are within reasonable limits, with the temperature ranging between 7-13^{o}C.

CHAPTER 5 - RESULTS AND DISCUSSIONS

5.1 Effects of Frictional Losses

This section presents the results of the entropy generation in each component, as well as the total entropy generated in the system. To understand why entropy based analysis is useful, Figure 5.1 shows how the entropy generation changes due to frictional losses. Figure 5.1 shows the battery module results that incorporate both heat transfer and frictional losses.

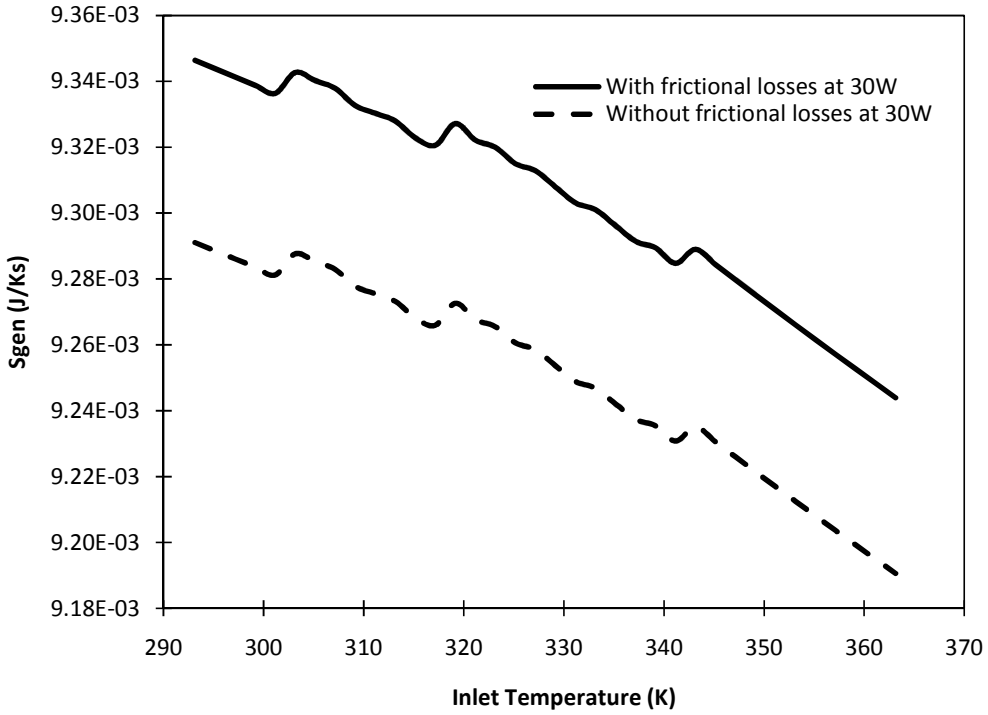

Figure 5.1 - Comparison of S_{gen} with and without frictional losses (30W)

In Figure 5.1, the frictional loss in the system adds to the overall entropy generation. In this case, there is a 0.6% difference between the two scenarios. This thesis will include the frictional losses where applicable, as friction should not be

neglected. Some of the graphs shown in this chapter will display a non-dimensional entropy generation number, which is obtained by the following equation

$$Ns = \frac{\dot{S}_{gen}}{\dot{m}C_p} \tag{5.1}$$

5.2 Battery Module Results

For the battery module, there are operating variables that can be changed in the analysis. One of the design variables analyzed was the diameter of the tubing within the battery module, as shown in Figure 5.2.

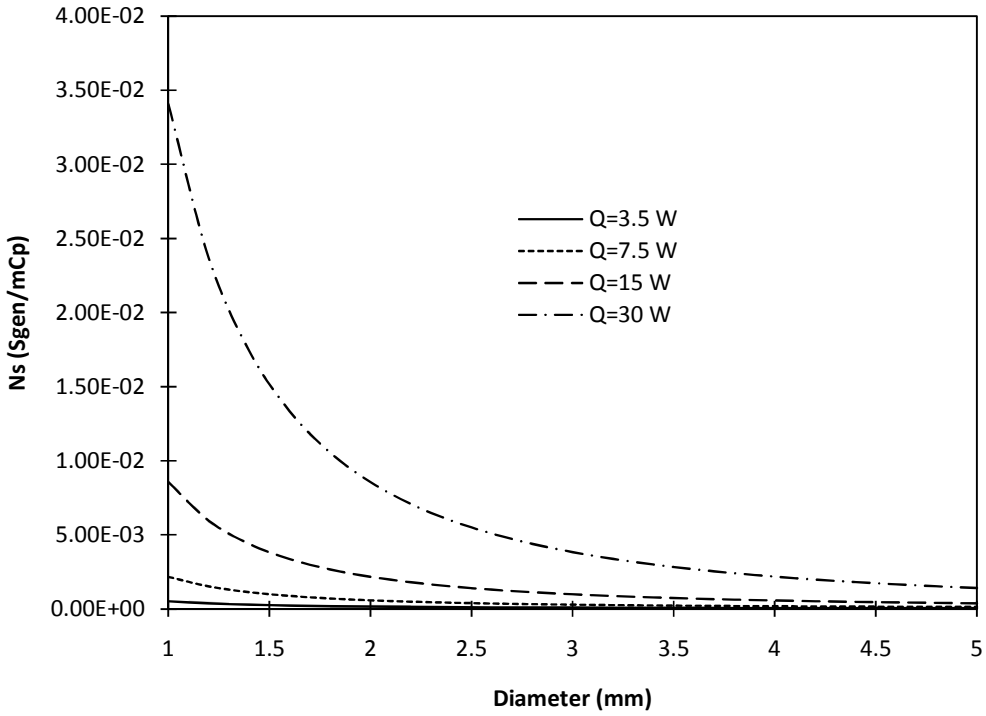

Figure 5.2 - Entropy generation at varying tube diameters

As explained in previous chapters, the battery module is tested at 4 different heat generation values, which are not the overall battery heat generation values, but the heat generation associated to each layer of tubing. The graph in Figure 5.2 shows a decreasing non-dimensional entropy generation number (Ns) for a larger tube diameter. The trend is the same for each of the heat generation values. It shows that a larger tube diameter leads to a lower the entropy generation. The reason for this trend is that the decrease in entropy generation is related to both the heat transfer and frictional losses in the system. From the S_{gen} equation, for the battery module outlined in previous chapters, it can be seen that when the heat generation (Q) increases, the overall entropy generation increases as well. This is one of the main reasons why there is a large difference in values between 3.5W and 30W of heat generation. For the frictional losses, when the tubing diameter increases, the mass flow rate will increase, and the change in pressure will decrease. The pump flow rate was held constant for this case, but in actual operation, the change in mass flow rate and pressure within the module will change the operating point for the pump. The decrease in pressure is larger than the increase in mass flow rate. Therefore, the effects of the frictional losses become smaller with an increased tube diameter. The other design variable is the inlet temperature entering the battery module, with the results shown in Figure 5.3.

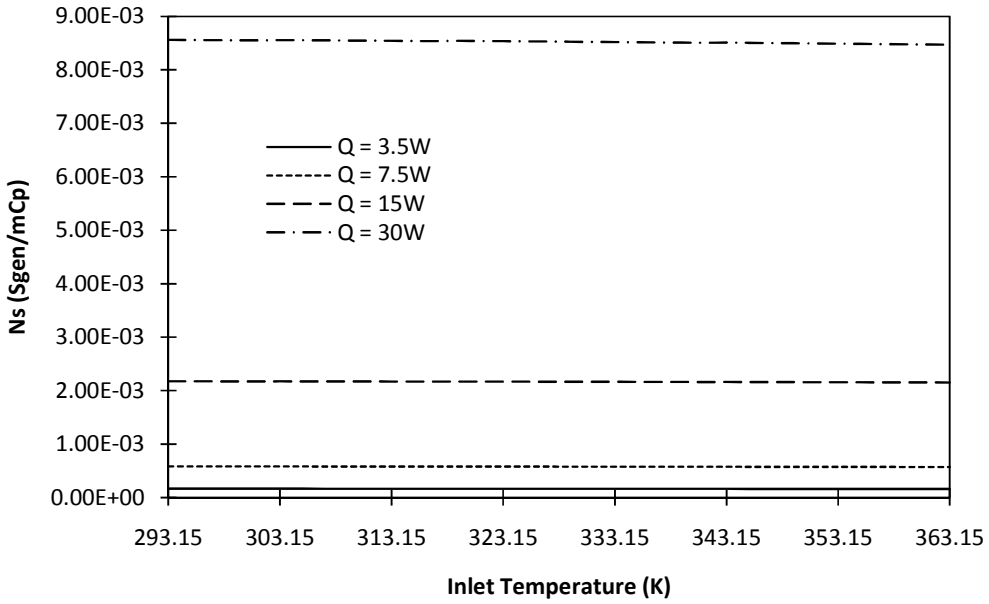

Figure 5.3 - Entropy generation in relation to the inlet temperature

The same heat generation values have been used. In Figure 5.3, it appears there is little or no change in the entropy generation regardless, of the inlet temperature. Looking at the entropy generation equation, the only variable that is changing is the change of temperature (ΔT). As the inlet temperature increases, the ability of the flowing fluid to reject heat generated by the battery is affected. Placing each of the heat generation values on separate graphs shows a different trend than result shown in Figure 5.3. Figures 5.4 to 5.7 are the individual graphs for the different heat generation values.

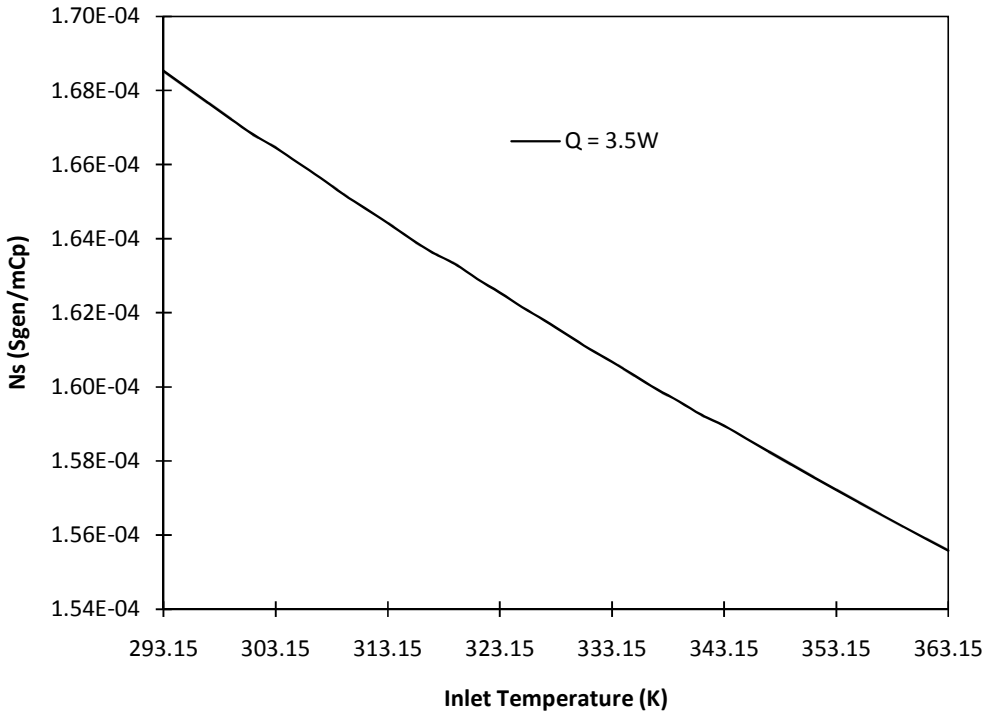

Figure 5.4 - Entropy generation in relation to the inlet temperature at 3.5W

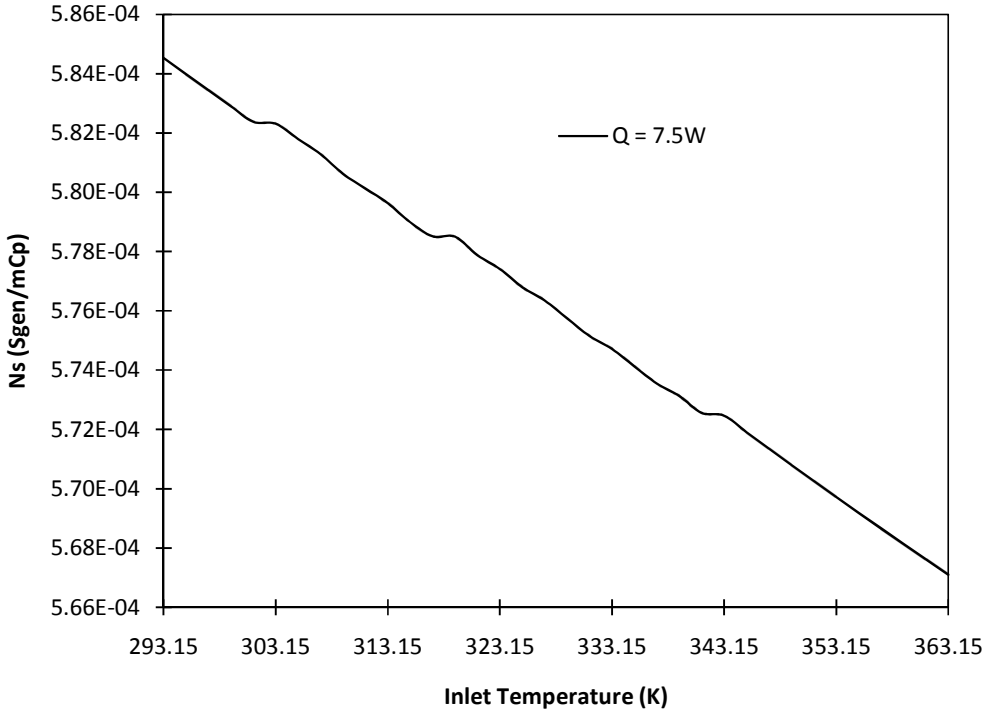

Figure 5.5 - Entropy generation in relation to the inlet temperature at 7.5W

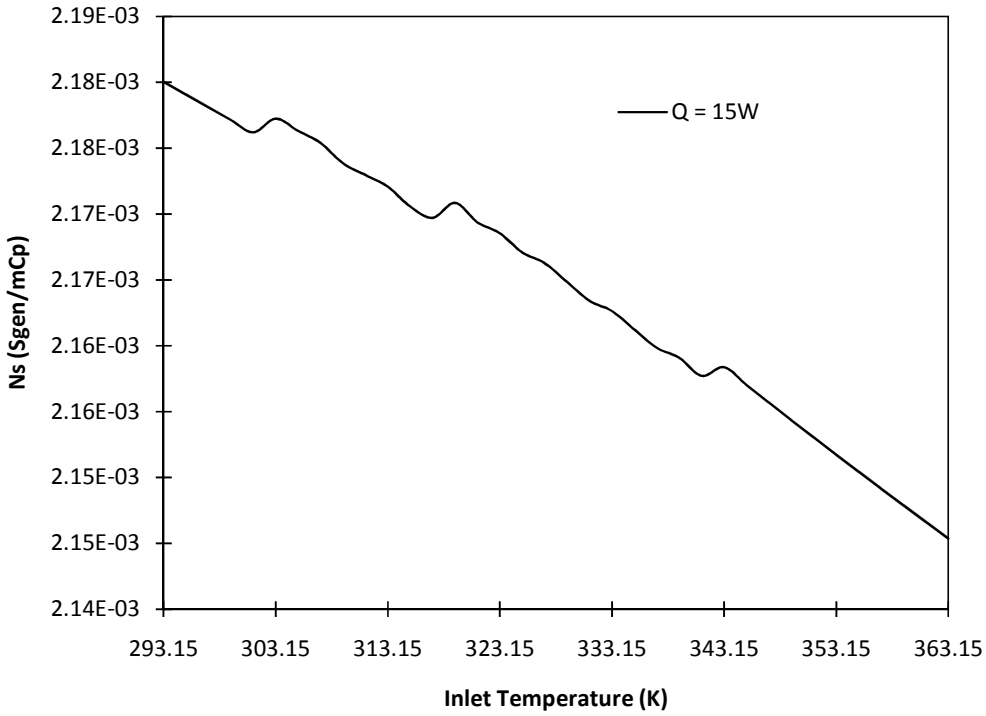

Figure 5.6 - Entropy generation in relation to the inlet temperature at 15W

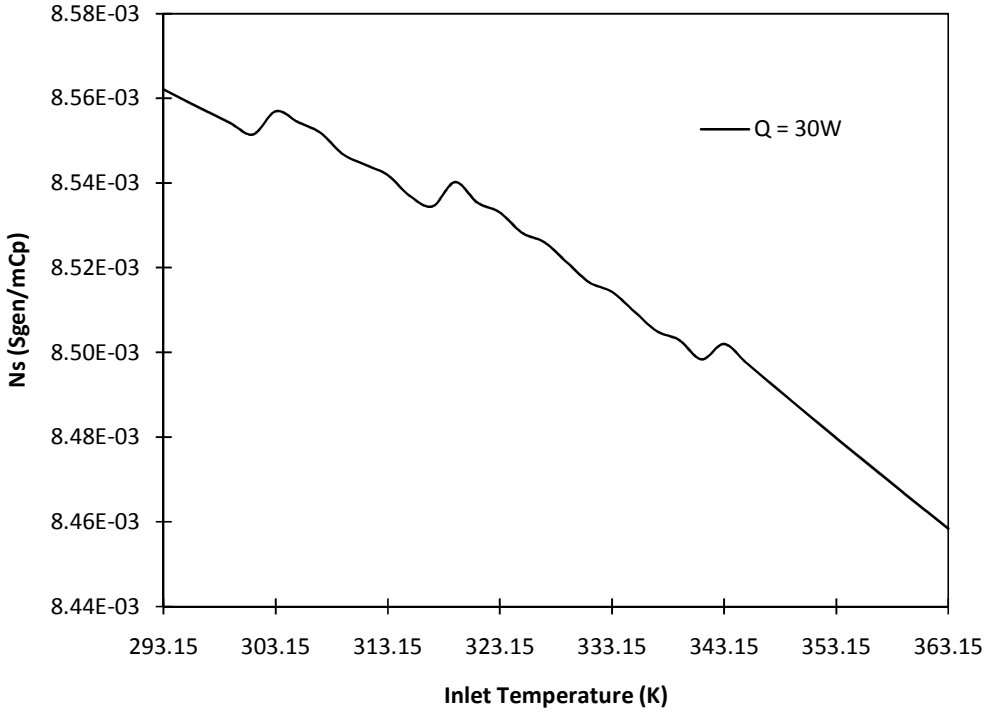

Figure 5.7 - Entropy generation in relation to the inlet temperature at 30W

From the previous figures, it can be seen that when the inlet temperature changes, there is indeed a change in entropy generation, although slight. As the inlet temperature increases, Ns decrease, due to the drop in pressure and mass flow rate with increased temperature. The lower values for pressure and mass flow rate lead to a lower value of the frictional entropy generation; however in relative terms these effects are unimportant.

A consideration for HEV and EV design is the climate in which the vehicles will operate. The ambient temperature does have an effect on the entropy generation in the battery module. The entropy generation equation does take into account the ambient temperature. For the results, the inlet temperature of the battery module was held at a constant value in each scenario.

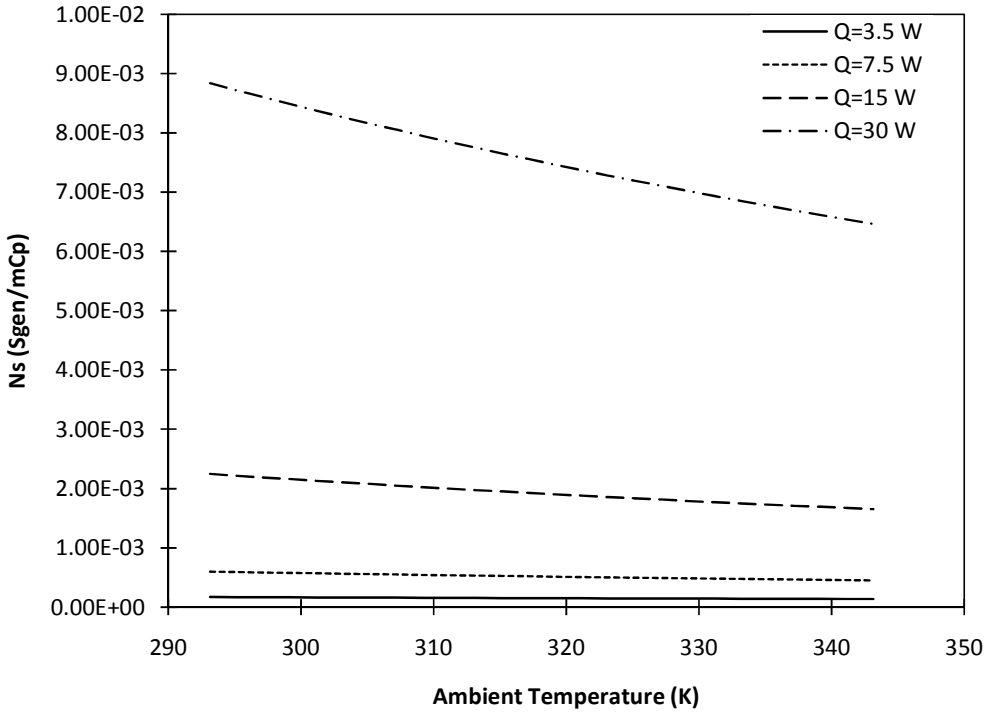

Figure 5.8 - Entropy generation in relation to the ambient temperature

As shown in Figure 5.8, the entropy generation decreases for a higher ambient temperature. Although the ambient temperature cannot be controlled, it is important to consider for vehicles in different climate conditions.

5.3 Heat Exchanger Results

The heat exchanger is integral for keeping the fluid temperature in the battery pack at acceptable levels. There are many types amounts of heat exchanger configurations. However, for this thesis, the heat exchanger reflects an average sized automotive radiator. Parameters were modified within the size of the selected radiator. Figure 5.9 shows how the number of radiator cores affects the entropy generation.

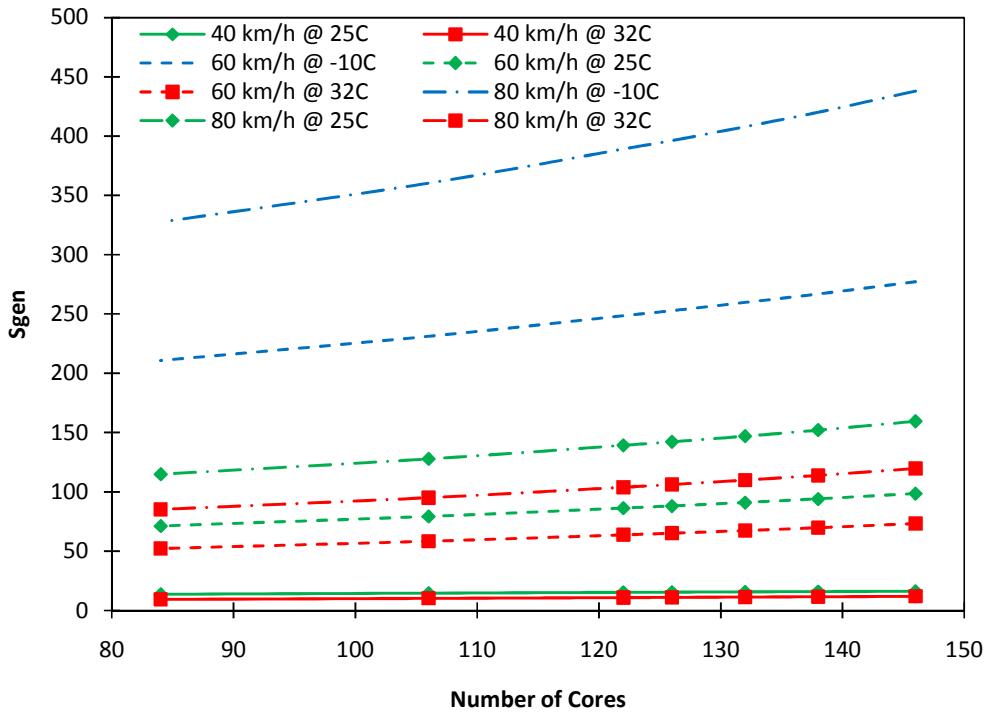

Figure 5.9 - Entropy generation in the heat exchanger with varying cores

The conditions in Figure 5.9 are explained below.

- Three vehicle speeds tested:
  - 40km/h – residential operating speed
  - 60km/h – urban operating speed
  - 80km/h – rural operating speed
- Three air climate conditions:
  - -10C – winter climate
  - 25C – warm summer climate
  - 32C – hot climate

The conditions above are solely for the inlet air conditions into the heat exchanger (temperature and flow rate). The fluid conditions were held constant at the upper temperature limit of the battery cells, which is 50C as a worst case scenario. Varying the number of cores, while keeping the dimensions of the heat exchanger unchanged, will change the fin geometry as well. The model developed in this thesis dynamically changes the geometry of the fins, which is important since the heat transfer surface area of the heat exchanger is affected when certain geometric parameters are changed.

In Figure 5.9, the trend shows that when entropy generation increases, the number of cores is increased. The variation in temperatures at -10C is greater than other operating conditions. It is the larger temperature difference which affects the entropy generation, as shown in the heat exchanger entropy equations. For the trend of increasing entropy, it is based on how the geometry changes with the change of cores. As the number of cores increases, the core mass velocity increases on both the air and liquid sides, which has a direct impact on the change in pressure. The change

in pressure on both sides increase. However, there is a larger increase on the air side than the liquid. When calculating the change in entropy on each side of the heat exchanger, the increase in ΔP causes the total change in entropy to increase, which therefore causes S_{gen} to increase as well.

5.4 Pump

Since the pump is assumed to be adiabatic, the only factor contributing to the entropy generation is the frictional losses. Figure 5.10 shows the results at varying inlet temperatures and flow rates.

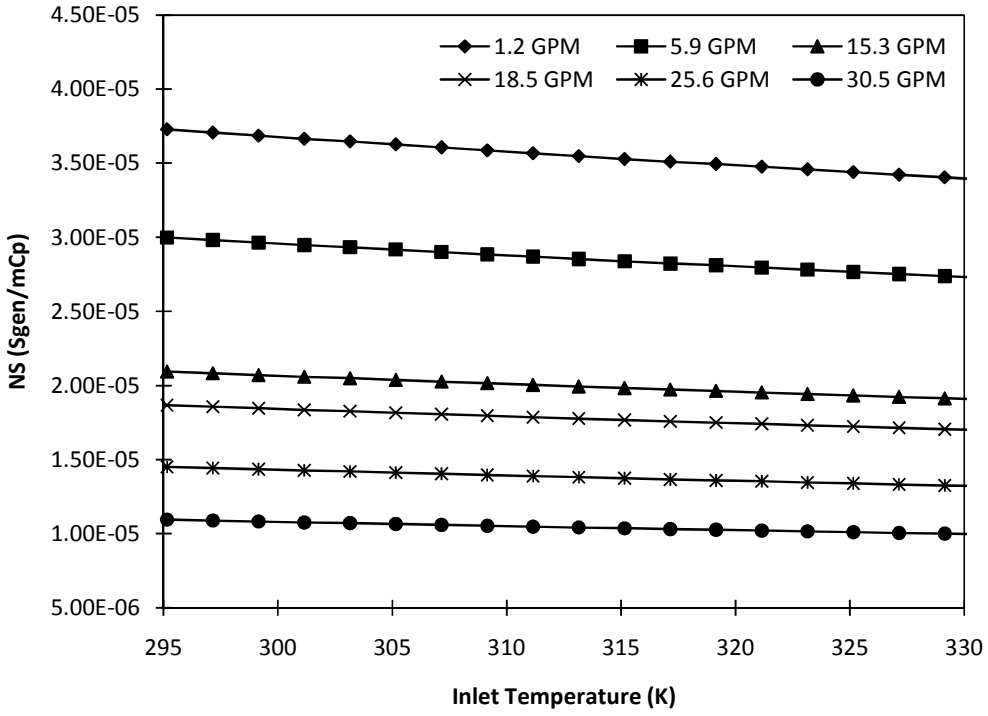

Figure 5.10 - Entropy generation with varying inlet fluid temperatures

Various pump flow rates were examined in Figure 5.10. These were selected from Figure 3.13. The upper and lower flow rates were selected, along with the flow

rate at a peak efficiency, and a few other points in between. Like the battery module, the inlet temperature into the pump was varied and the results show that the entropy generation decreases for each flow rate, when the temperature of the fluid increases. In the entropy generation equation for the pump, the only contributing factors are the mass flow rate, pressure differential, density of the fluid at the given inlet temperature, and the inlet temperature. However, it is the pressure differential which contributes most to the trends seen in Figure 5.10. From Equation (3.76), for the pressure differential, it is the power produced by the pump, mass flow rate of the fluid, and the efficiency of the pump at the selected flow rate, which affects the change in pressure. As the flow rates increase, the power increases and the efficiency will rise and fall as shown in Figure 3.13. In Equation (3.76), the rising efficiency values and higher power values cause the final ΔP to drop when the flow rate increases. As ΔP decreases for a fixed power and efficiency, the flow rate increases. The other parameter that can be varied is the mass flow rate of the pump. Figure 5.11 shows the results.

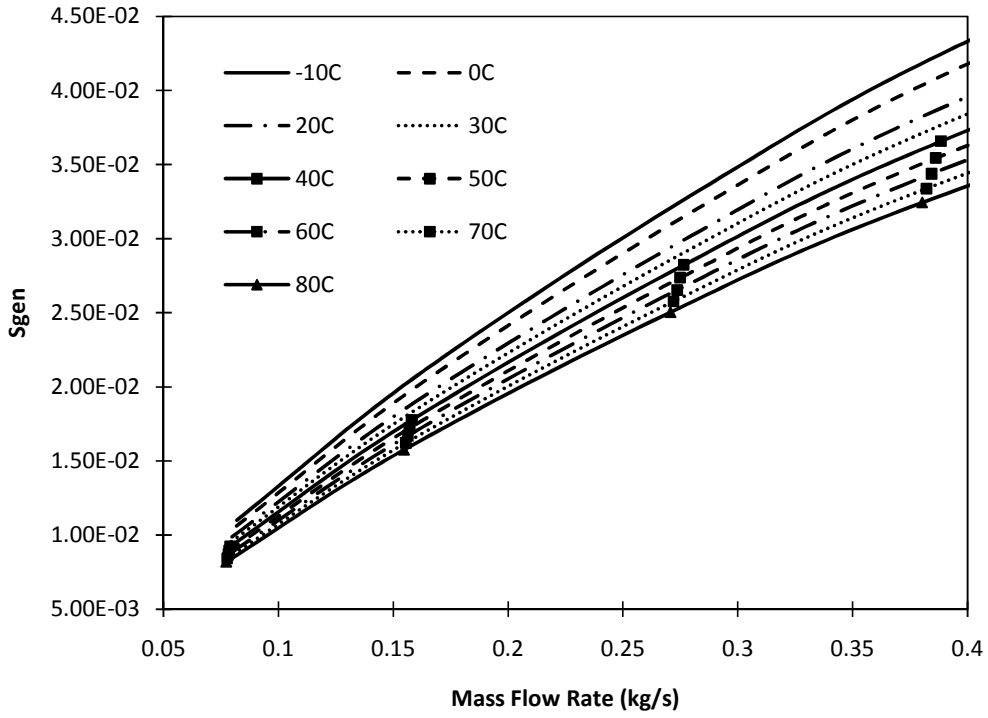

Figure 5.11 - Varying pump flow rates at various operating temperatures

The various fluid operating temperatures were chosen to illustrate how the entropy generation changed based on temperature. This graph is different from Fig. 5.10 because Fig. 5.10 corresponds to entropy generation when the pump is operating at a consistent flow rate and varying temperature. Figure 5.11 shows how the variation in flow rate affects entropy generation at different operating temperatures. Figure 5.11 shows the resemblance with Figure 3.14, the pump efficiency curve. The contributing factor is again the pressure differential, which drops as the efficiency of the pump increases. When the graph in Figure 5.11 reaches its peak then decreases, this is the point where the pump reaches a maximum efficiency, followed by a decrease in efficiency. Regardless of the fluid temperature, the lowest amount of entropy is generated when the pump is operating at low flow rates.

5.5 Throttle

The throttle will represent the hoses/lines connecting the components together. For the results in this section, a constant pressure differential throughout the throttle, with the flow rate and temperature varying,, will be assumed, Figure 5.12 shows the results.

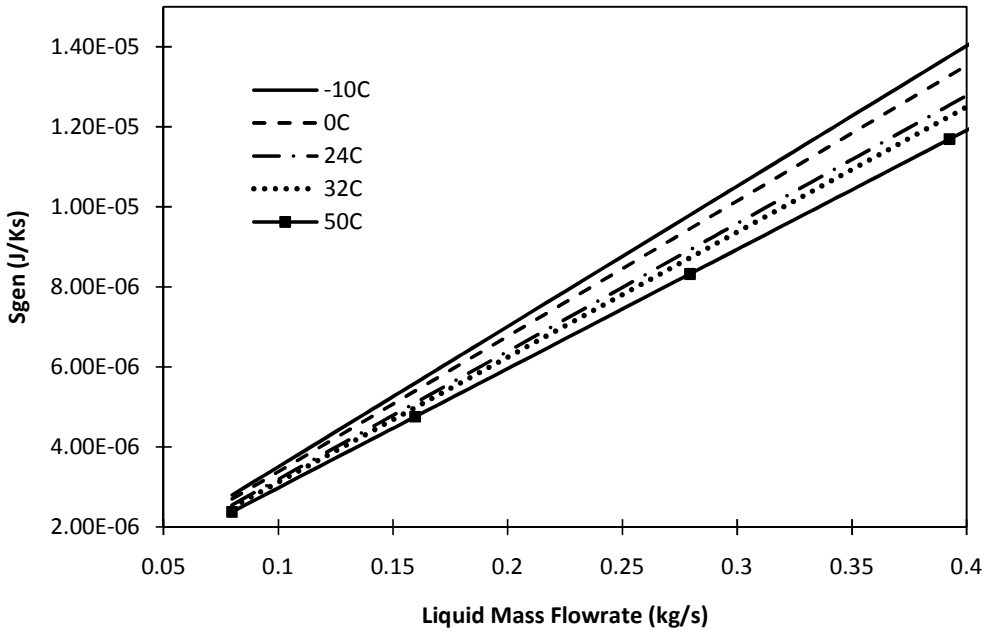

Figure 5.12 - Entropy generation in the throttle

The mass flow range is the operating range of the pump and the temperature range. It simulates the highest operating temperature of the batteries (50C) and colder fluid temperatures, which the throttle may briefly experience during cold weather startup. Figure 5.12 shows how the entropy generation varies as a function of flow rate and temperature.

5.6 Total System Entropy Analysis

All components have been analyzed individually. The entropy generation of each component can now be combined to find the total system entropy generation. By analyzing the entropy generation within the entire system, potential improvements within the system can be identified. Entropy generation for the individual components show how thermal and friction irreversibilities lead to reduced energy performance of components and the system overall. The conditions and parameters leading to the location of the lowest entropy generation have practical significance by indicating how various design changes can be made to improve system performance. It is important to have the lowest total entropy generation because, this reduces the amount of exergy destruction, or loss of available energy in the system, according to Equation (1.1). By minimizing exergy destruction, this leads to lower parasitic system losses and more effective heat transfer within the maximizing the amount of work being produced by the system. When calculating the total system entropy generation, one component is changed while the other three components are held constant. The battery module is the first component to be changed in this section, while the pump, radiator and throttle parameters are held constant. Figure 5.13 shows the battery module at varying inlet temperatures.

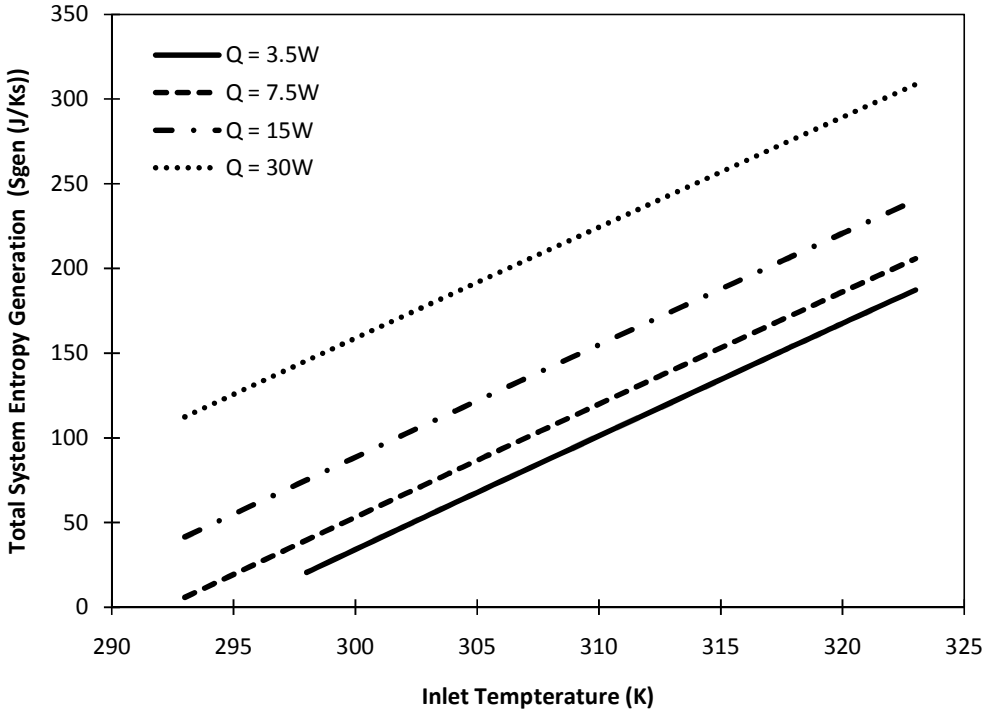

Figure 5.13 - Total system S_{gen} with varying battery module inlet temperatures

The diameter of the tubing is 2mm. The original length of the tubing within the battery module was left unchanged. The pump is operating at a constant flow rate of 18.5 GPM, which also yields the maximum efficiency and lowest entropy generation in the pump. The change in pressure within the throttle reflects the pressure increase to the system by the pump. The heat exchanger was unchanged from the initial model design, and the air flow rate into the radiator reflects a vehicle travelling at 60km/h.

From Figure 5.13, the total entropy generation of the system increases as the inlet temperature of the fluid into the battery module increases. The reason is due to the higher ΔT in the heat transfer process. However, the heat exchanger is the component that is contributing the most entropy generation within the system.

Entropy generation by the pump and throttle have little effect on the final value of the total system entropy generation. Figures 5.14 to 5.17 show how the system entropy generation changes with varying tube length. The tube diameter remains at 2mm, with the inlet fluid temperature at 50C.

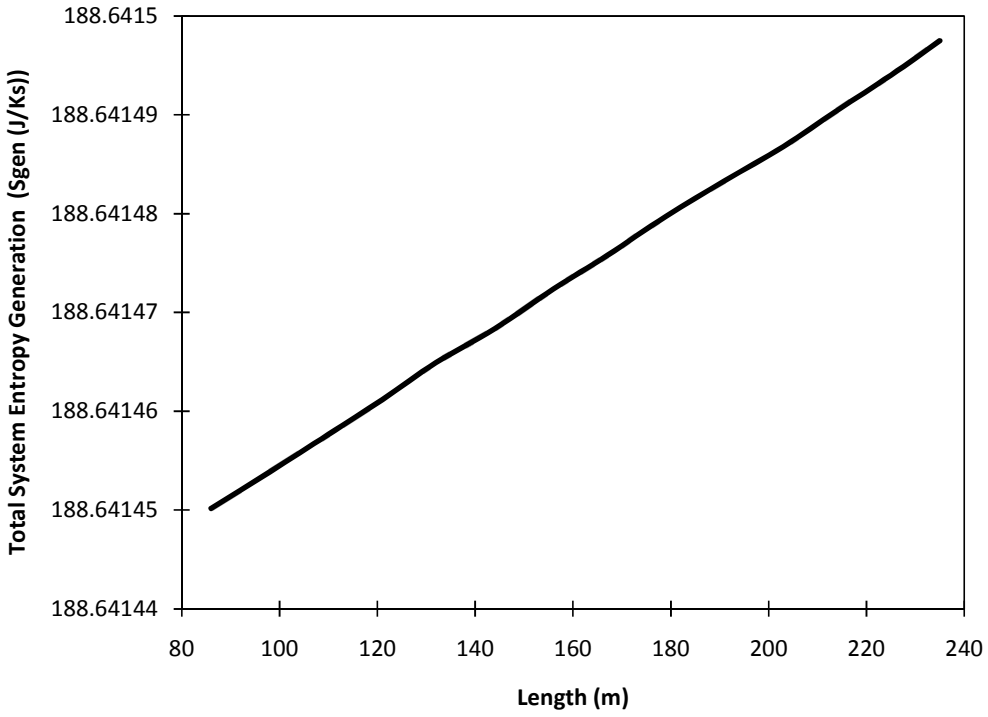

Figure 5.14 - Total system S_{gen} with varying tube length at 3.5W

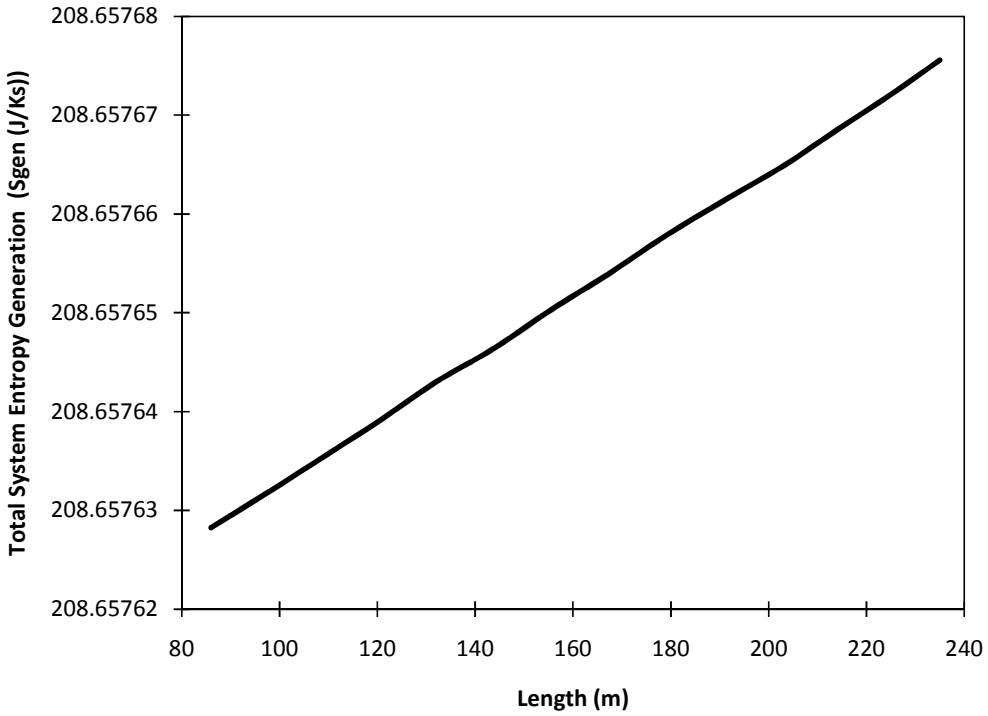

Figure 5.15 - Total system S_{gen} with varying tube length at 7.5W

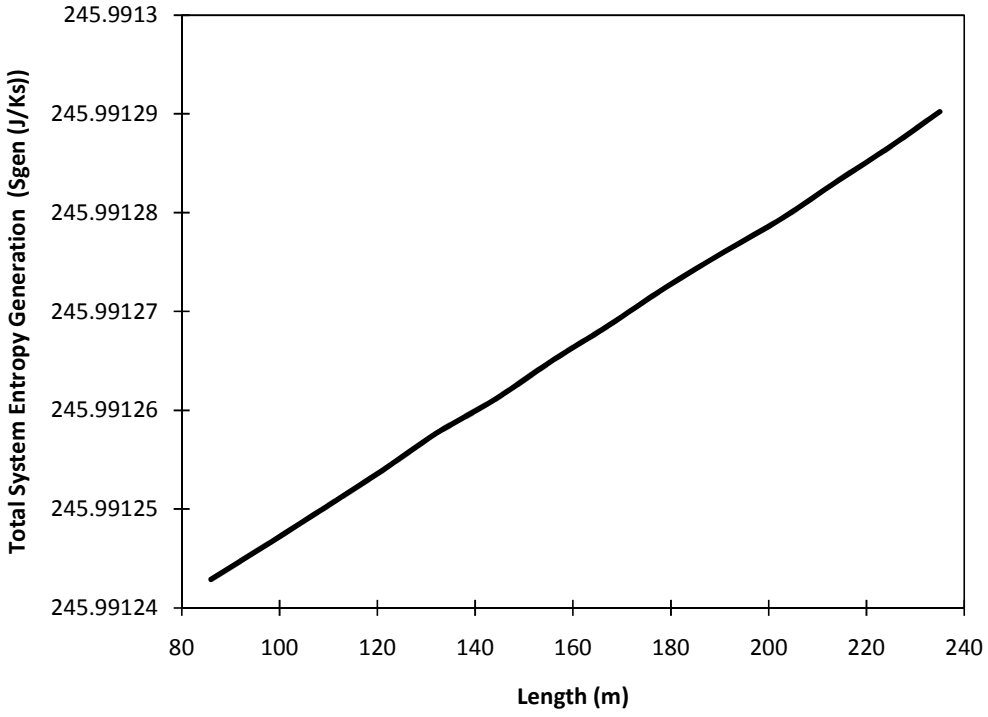

Figure 5.16 - Total system S_{gen} with varying tube length at 15W

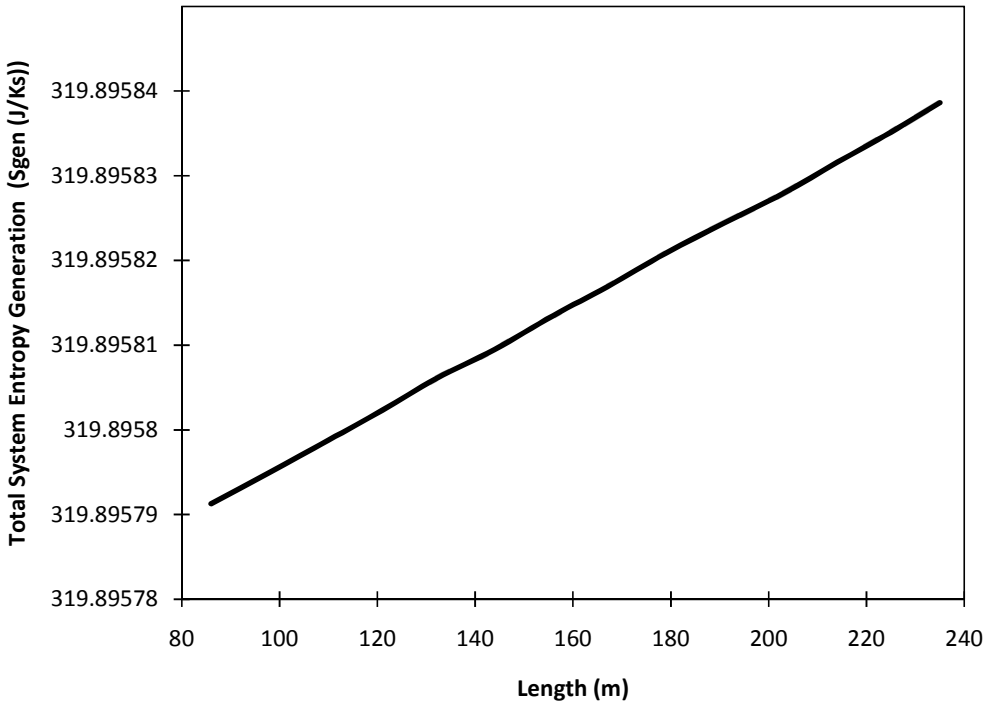

Figure 5.17 - Total system S_{gen} with varying tube length at 30W

The pump was held at a constant flow rate of 18.5 GPM, and the heat exchanger was not changed from the original model. The total system entropy generation increases as the total tubing length increases, and the heat exchanger is again the highest contributor to entropy generation. Looking at Figure 5.14, the lowest entropy generation is 188.64145 W/mK, while the highest value is 188.6415 W/mK. That is only an increase of 0.00005 W/mK over a substantial amount of tubing. This trend is continued through Figures 5.15 to 5.17, where the entropy generation increase is plotted. One of the factors that contribute to this trend is that the length of tubing does not affect the heat transfer portion of the entropy generation equation for the battery module. The length is only a factor in the frictional losses within the battery module. It was discussed previously that the frictional losses are not as high as the heat transfer losses, but still important. In the case of the varying

tube length, the change of frictional losses within the battery module was not enough to dramatically alter the total system entropy generation.

Another variable that was modified within the battery module for the total system analysis was the diameter of the tubing. The operating conditions of the other components remain the same as described previously. With the change in diameter, the length of tubing changes in accordance to the diameter. However, the tube thickness remains the same. Figure 5.18 shows the results of the modified tube diameter.

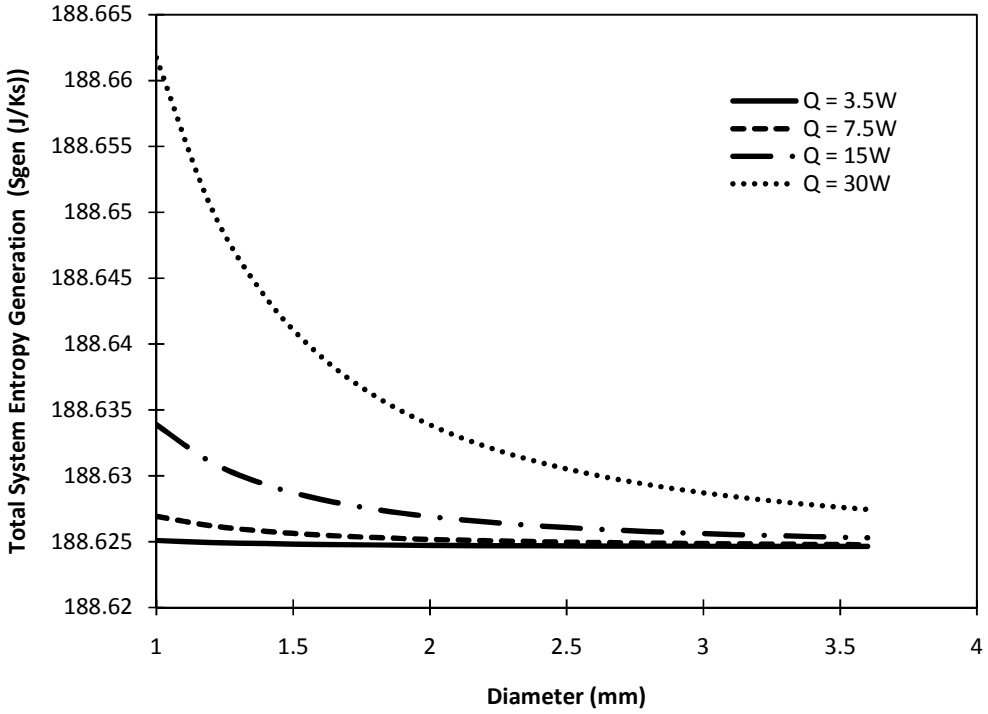

Figure 5.18 - Total system S_{gen} with varying battery module tube diameter

The overall trend in Figure 5.18 is that for each heat generation range, the total system entropy generation decreases, as the diameter of tubing within the battery

module increases. The examination of this trend is linked to both the heat transfer and frictional losses in the entropy generation equation. As the diameter increases, it reduces the ΔT of the heat transfer, and this creates a lower entropy generation due to the heat transfer effects. For the frictional losses, when the diameter is increased, the mass flow rate increases, which creates higher entropy losses due to friction. However, the reduced entropy generated on the heat transfer side is less than the entropy gained due to frictional losses, therefore creating a lower entropy generation for the battery module, when the heat transfer and frictional losses are added together. Like the previous figures which showed a minimal increase in entropy generation due to tube length, there is a minimal decrease in entropy generation as the diameter increases.

Further results reflect changes made to the heat exchanger. The first change to the heat exchanger will be the number of cores. It will be the same core values used for the individual component analysis. Figure 5.19 shows the total system entropy generation, for modified heat exchanger cores.

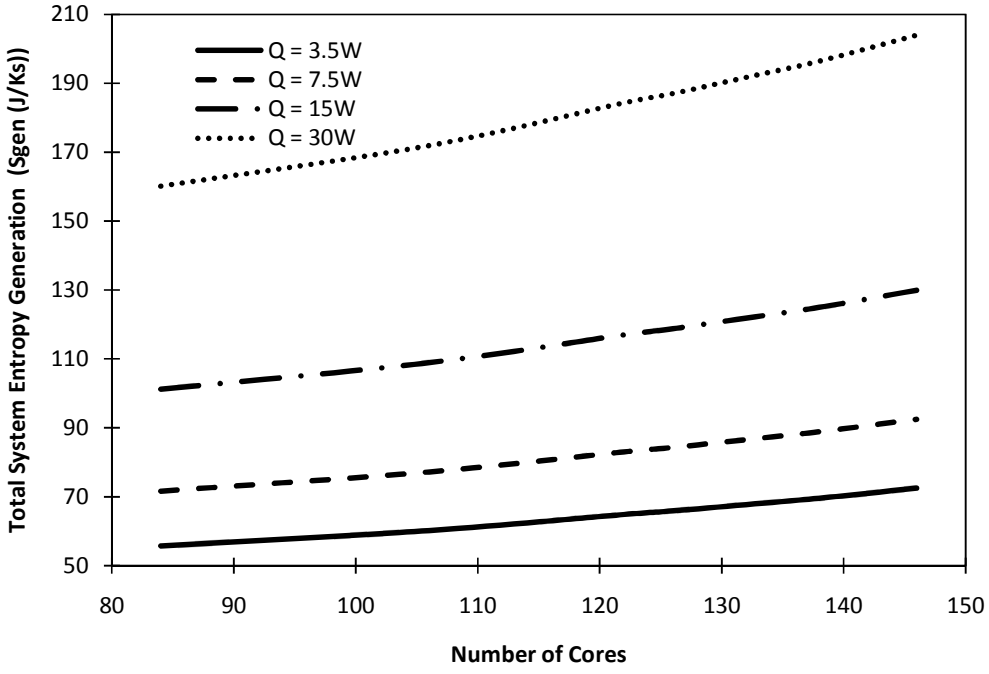

Figure 5.19 - Total system S_{gen} with varying radiator cores

Like Figure 5.9, when the number of cores increases, the entropy generated increases as well. It is the increase in the core mass velocity which causes ΔP on both sides of the heat exchanger to increase, thus increase the entropy generated. The vehicle was assumed to be travelling at 60km/h.

Another modification of the system was a varied mass flow rate through the heat exchanger. When the mass flow through the radiator was modified, the mass flow rate through the battery module, pump and throttle were changed as well, to satisfy conservation of mass. A specific range of the pump's flow rate was used. Figure 5.20 shows the results.

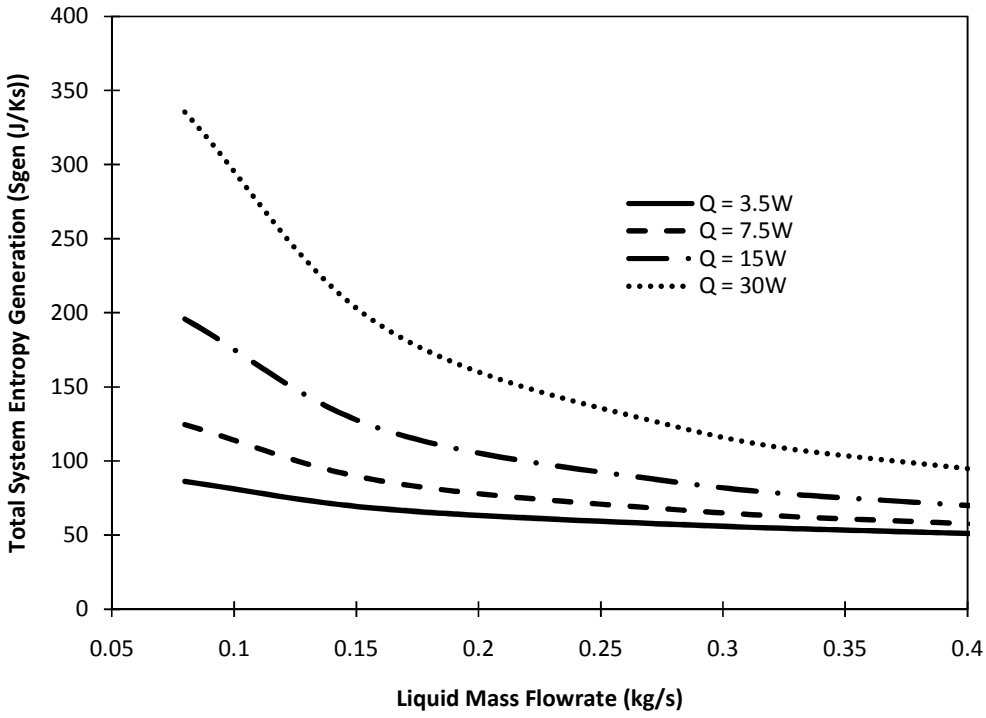

Figure 5.20 - Total system S_{gen} with varying mass flow rate

Figure 5.20 shows a substantial drop in entropy generation when the flow rate is increased. The entropy generation for each component with increasing mass flow rate needs to be explained, to understand the reduction in total system entropy generation. As the mass flow rate increases, the entropy generation for the battery module, pump, and throttle increase. As explained earlier, it is the heat exchanger that contributes most to entropy generation in the entire system, as the increases in entropy to the other three components is not as significant. Within the heat exchanger, as the mass flow rate increases, the overall heat transfer coefficient, U, increases, which leads to an increase of heat transfer within the radiator. With the increase in U and Q, the air temperature increases as it passes through the heat exchanger, removing more heat from the system and the liquid temperature drops further. The value for ΔS_a increases but ΔS_f becomes more negative. It's the more

negative ΔS_f that causes a decrease in entropy generation in the heat exchanger, and therefore a drop in entropy generation for the overall system.

CHAPTER 6 - CONCLUSIONS AND RECOMMENDATIONS FOR FUTURE RESEARCH

6.1 Conclusions

In this thesis, a thermal management system was analyzed to improve liquid cooling of battery modules in HEVs and EVs. By reducing the entropy generation, the irreversibilities and power needed to overcome frictional losses can be minimized. Heat transfer and frictional irreversibilities lead to additional power consumed to operate the liquid cooling. So their combined minimization through entropy generation can lead to higher system efficiency.

The following main conclusions were obtained from this thesis.

- A new entropy-based method was developed for an indirect liquid cooled battery thermal management system. The equations allow for a flexible design with flat battery cells that are being implemented in the UOIT EcoCAR. They can also be adapted to future production vehicles.
- A heat exchanger model was developed based on the geometry of an existing automotive radiator, and results were verified against published data.
- An electric automotive water pump was selected, as it can be incorporated well into an EV cooling system.
- A Second Law analysis of system components accounted for the heat transfer and frictional losses of the system. Although frictional losses have not been the focus of study in the past, in this thesis it was demonstrated that there exist a difference including the frictional losses in the system.

- Parameters were tested in each individual component which experienced both a decrease and increase in entropy generation when variables were changed. The heat exchanger contributed the most entropy generation in the entire system, due to the range of temperature changes of the two working fluids.
- When trying to achieve the lowest possible entropy within a system, it may not be possible because the operating condition of lowest entropy generation may not be practical. Thus, the results are used to identify the direction of decreasing entropy generation, to which the design is directed.
- The heat exchanger model allows for a Second Law analysis and provides useful insight to the radiator geometry. Heat exchanger parameters can be varied to enhance heat transfer effectiveness by analyzing the entropy generation results.
- The new model developed in this thesis is theoretical, as a liquid cooled battery system for automotive purposes is not commonly used. This model can aid in the design process of HEVs and EVs by examining potential improvements within the cooling system, thus creating a more efficient system. Liquid cooled BTMS need more development to ensure the best systems are built with high quality at reasonable costs.

6.2 Recommendations for Future Research

Liquid cooled battery management systems are a relatively new technology and require more research before they can implemented on production vehicles. The Second Law analysis in this thesis is a starting point for optimizing the cooling system's performance. Recommendations for future Research are presented below.

- While the model in this thesis is theoretical, an experimental working prototype should be built to help further validate the theoretical model. The prototype would need to have pressure and temperature sensors at several points throughout the system, as well as a programmable battery cycler to simulate loads.
- Analysis of a larger battery module should be conducted, as this thesis only examined a single representative cell. A larger battery system will have cell stacks oriented in different directions. This will involve a more complex system of tubing.
- Allowances must be made for external heat influx, which is often the dominant mechanism of heat source.

REFERENCES

1. Key World Energy Statistics. International Energy Agency, Retrieved January 24, 2009, from http://www.iea.org/textbase/nppdf/free/2008/key_stats_2008.pdf.

2. Environmental Protection Agency, (2008). Air Pollution. National Air Quality - Status and Trends through 2007, Retrieved March 10, 2009, from http://www.epa.gov/air/airtrends/2008/report/AirPollution.pdf.

3. Hirsch, R.L., Bezdek, R., & Wendling, R. U.S. Department of Energy, (2005). Peaking of world oil production: impact, mitigation, & risk management, from http://www.netl.doe.gov/publications/others/pdf/Oil_Peaking_NETL.pdf.

4. Argonne National Laboratory, Initials. USDOE, (2007). Just the Basics: how do hevs work? Argonne, IL, 10289.

5. Fuhs, A. (2009). Hybrid vehicles and the future of personal transportation. Boca Raton, FL: Taylor & Francis Group, LLC.

6. Husain, I. (2005). Electric and hybrid vehicle design fundamentals. Boca Raton, FL: Taylor & Francis Group, LLC.

7. Ehsani, M., Gao, Y., & Emadi, A. (2010). Modern electric, hybrid electric, and fuel cell vehicles: fundamentals, theory, and design 2nd ed.. Boca Raton, FL: Taylor & Francis Group, LLC.

8. Pesaran, A. (2001). Thermal Performance of EV and HEV Battery Modules and Packs. Proceedings of the Advanced automotive battery conference Golden, Colorado: National Renewable Energy Laboratory.

9. Kim, G.H., & Pesaran, A. (2006). Battery thermal management system design modeling. Proceedings of the International battery, hybrid and fuel cell electric vehicle conference and exhibition (evs-22) Yokohama, Japan: National Renewable Energy Laboratory.

10. Pesaran, A. (2007). Battery requirements for plug-in hybrid electric vehicles – analysis and rationale. Proceedings of the Sustainability: the future of transportation Anaheim, CA: National Renewable Energy Laboratory. NREL/PR-540-42469.

11. Kelly, K.J., & Rajagopalan, A. (2001). Benchmarking of OEM hybrid electric vehicles at NREL. National Renewable Energy Laboratory, (NREL/TP-540-31086). Golden, CO.

12. Sonntag, R., Borgnakke, C., & Wylen, G. (2003). Fundamentals of thermodynamics. Hoboken, NJ. John Wiley & Sons Inc.

13. Zhao, L., & Lui, L.H. (2010). Entropy generation analysis of electro-osmotic flow in open-end and closed-end micro-channels. International Journal of Thermal Sciences, 49, 418–427.

14. Jankowski, T.A. (2009). Minimizing entropy generation in internal flows by adjusting the shape of the cross-section. International Journal of Heat and Mass Transfer, 52, 3439–3445.

15. Oliveski, R.C., Macagnan, M.H., & Copetti, J.B. (2009). Entropy generation and natural convection in rectangular cavities. Applied Thermal Engineering, 29, 1417–1425.

16. Sahiti, N., Krasniqi, F., Fejzullahu, Xh., Bunjaku, J., & Muriqi, A. (2008). Entropy generation minimization of a double-pipe pin fin heat exchanger. Applied Thermal Engineering, 28, 2337–2344.

17. Demirel, Y., & Al-Ali, H.H. (1997). Thermodynamic analysis of convective heat transfer in a packed duct with asymmetrical wall temperatures. International Journal of Heat and Mass Transfer, 40(5), 1145-1153.

18. Hooman, K., Gurgenci, H., & Merrikh, A.A. (2007). Heat transfer and entropy generation optimization of forced convection in porous-saturated ducts of rectangular cross-section. International Journal of Heat and Mass Transfer, 50, 2051–2059.

19. Yang, WJ, Furukawa, T., & Torii, S. (2008). Optimal package design of stacks of convection-cooled printed circuit boards using entropy generation minimization method. International Journal of Heat and Mass Transfer, 51, 4038–4046.

20. Demirel, Y., & Kahraman, R. (1999). Entropy generation in a packed duct with wall heat flux. International Journal of Heat and Mass Transfer, 42, 2337-2344.

21. Bejan, A. (1996). Entropy generation minimization. Boca Raton, FL. CRC Press.

22. Bejan, A., & Siems, D.L. (2001). The Need for exergy analysis and thermodynamic optimization in aircraft development. Exergy International Journal, 1(1), 14–24.

23. Amati, V., Bruno, C., Simone, D., & Sciubba, E. (2008). Exergy analysis of hypersonic propulsion systems: performance comparison of two different scramjet configurations at cruise conditions. Energy, 33, 116–129.

24. Ordonez, J.C., & Bejan, A. (2003). Minimum power requirement for environmental control of aircraft. Energy, 28, 1183–1202.

25. Perez-Grande, I., & Leo, T.J. (2002). Optimization of a commercial aircraft environmental control system. Applied Thermal Engineering, 22, 1885–1904.

26. Paulus, D.M., & Gaggioli, R.A. (2003). The Exergy of lift and aircraft exergy flow diagrams. International Journal of Thermodynamics, 6(4), 149-156.

27. Rohrauer, G., Maduro, M. (2008). UOIT EcoCAR Year 1 - Report 1, Oshawa, ON.

28. Rohrauer, G., Maduro, M. (2008). UOIT EcoCAR Year 1- Report 2. Oshawa, ON.

29. Rohrauer, G., Maduro, M. (2008). UOIT EcoCAR Year 1 - Report 4. Oshawa, ON.

30. Rohrauer, G., Maduro, M. (2008). UOIT EcoCAR Year 1 - Report 5. Oshawa, ON.

31. Li, H., & Figliola, R.S. (2004). Optimization of an automotive cooling system based on exergy analysis. Society of Automotive Engineering, 2004-01-3541.

32. Crowe, C., Elger, D., & Roberson, J. (2006). Engineering fluid mechanics. Hoboken, NJ. Wiley Science.

33. Munson, B.R., Young, D.F, & Okiishi, T.H. (2002). Fundamentals of fluid mechanics 4th ed. Hoboken, NJ: John Wiley & Sons Inc.

34. Çengel, Y. (2006). Heat and mass transfer. New York, NY. McGraw-Hill Science/Engineering/Math. p.46.

35. Bejan, A., Tsatsaronis, G., & Moran, M. (1996). Thermal design and optimization. Hoboken, NJ. Wiley-Interscience., pg.283.

36. Shah, R., & Sekulić, D. (2003). Fundamentals of heat exchanger design. Hoboken, NJ. Wiley & Sons Inc.

37. Kuppan, T., & Kemp, I. (2007). Heat exchanger design handbook. New York, NY. Marcel Dekker.

38. Charyulu, D.G., Singh, G., & Sharma, J.K. (1999). Performance evaluation of a radiator in a diesel engine - a case study. Applied Thermal Engineering, 19, 625-639.

39. Çengel, Y., & Turner, R. (2005). Fundamentals of thermal-fluid sciences. New York, NY. McGraw-Hill.

40. Schwaller, A. (2004). Total automotive technology. Clifton Park, NY. Thomson Delmar Learning.

41. AA1Car Auto Diagnosis Repair Help, , Initials. (Photographer). (2007). Water pump cutaway. [Web]. Retrieved from http://www.aa1car.com/library/water_pump_cutaway.jpg.

42. Esposito, A. (2008). Fluid power with applications. Upper Saddle River, NJ. Pearson Prentice Hall.

43. Turner, W., & Doty, S. (2009). Energy management handbook. Linburn GA. The Fairmont Press, Inc.

44. Stewart Components Inc, 2009, Company Document. Escanaba, MI.

45. Oliet, C., Oliva, A., Castro, J., & Perez-Segarra, C.D. (2007). Parametric studies on automotive radiators. Applied Thermal Engineering, 27, 2033–2043.

46. Holman, J.P. (1986). *Heat transfer*. Singapore: McGraw-Hill Book Co.

47. Bahrami, M., Yovanovich, M.M., & Marotta, E.E. (2006). Thermal joint resistance of polymer-metal rough interfaces. *Journal of Electronic Packaging*, *128*, 23-29.

APPENDIX

Initial Values

I = 80A

Cell dimensions:

L = 445mm

W = 292mm

H = 16mm

k_{cell} = 1 W/mK

$$P = \dot{q}$$

$$I^2 R = h_{overall} A(T_s - T_\infty)$$

$$(80Amps)^2\left(\frac{0.43}{1000}\right) = h(0.445m \times 0.292m)(T_s - T_\infty)$$

$$2.75W = 0.13h\Delta T$$

$$\dot{q} = \frac{2.75W}{(0.016m)(0.445m)(0.292m)} = 1132\frac{W}{m^3}$$

$$(T_{core} - T_s) = \frac{\dot{q}L^2}{2k_{cell}}$$

$$(T_{core} - T_s) = \frac{1132\frac{W}{m^3}(0.008m)^2}{2\left(1\frac{W}{mK}\right)}$$

$$(T_{core} - T_s) = 4.5K$$

Therefore, the core temperature is 4.5°C hotter than the cell surface temperature

Using flat horizontal plate with small separation (δ):

Let the film temperature be 303K.

Air properties @ 303K

v = 1.608x10^{-5} m^2/s, Pr = 0.728, k = 0.02588 W/mK, β = 1/T = 1/303

Let δ = 2.3x10^{-3}m

$$\frac{k_{eff}}{k} = C(Gr\,\mathrm{Pr})^n \left(\frac{L}{\delta}\right)^m$$

$$Gr = \frac{g\beta(T_1 - T_2)\delta^3}{v^2} = \frac{9.81\frac{m}{s^2}\left(\frac{1}{303K}\right)\Delta T(2.3\times10^{-3}m)^3}{\left(1.608\times10^{-5}\frac{m^2}{s}\right)^2}$$

$$Gr = 1.80\Delta T$$
$$Gr\,\mathrm{Pr} = 1.80\Delta T(0.728)$$
$$Gr\,\mathrm{Pr} = 1.31\Delta T$$

Since GrPr < 1700, this means that

$$\frac{k_{eff}}{k} = 1$$

To calculate the fraction of tubing in contact with the cells (both top and bottom cells), the distance between cells is taken as 1.05mm. With an inside tube diameter of 2mm and wall thickness of 0.3mm, this gives an outside tube diameter of 2.3mm. The fraction of tubing in contact with the cells is calculated by the total angle that is touching the cell surface.

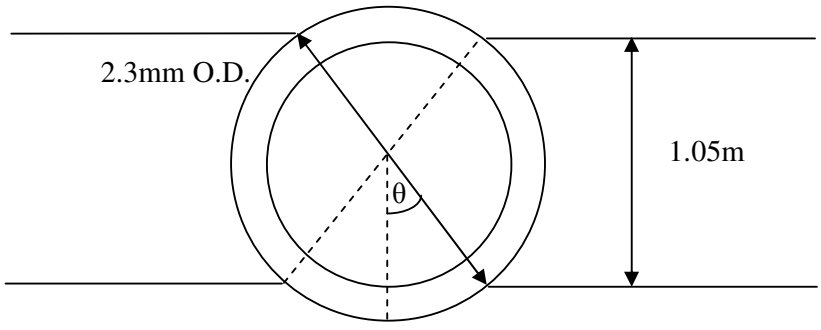

To calculate θ:

$$r_{out}\cos\theta = 1.05mm$$
$$\theta = 24.5^o$$

Therefore, the fraction of tube in contact with the cell surfaces is:

$$fraction = \frac{4(24.5)}{360} = 0.27$$

Assuming laminar flow through the tube, the heat transfer coefficient is:

$$h = \frac{3.66k}{D_{in}} = \frac{3.66(0.42)}{0.002} = 768.6\frac{W}{m^2K}$$

Solving R_{total1},

$$R_{total1} = \frac{1}{h_{in}A} + \left[\frac{\ln\left(\frac{r_{out}}{r_{in}}\right)}{2\pi L_{tube}k} \times (air\%)\right] + \left(\frac{\delta}{kA} \times air\%\right)$$

$$R_{total1} = \frac{1}{768.6\pi(0.002m)(5m)(0.73)} + \left(\frac{\ln\frac{0.00115}{0.001}}{2\pi(0.42)(5m)(0.73)}\right) + \frac{2.3\times10^{-3}m}{\pi(0.02588)(0.0023m)(5m)(0.73)}$$

$$R_{total1} = 0.0567 + 0.0145 + 3.3697$$

$$R_{total1} = 3.441\frac{K}{W}$$

Solving for R_{total2},

$$R_{total2} = \frac{1}{h_{in}A} + \left[\frac{\ln\left(\frac{r_{out}}{r_{in}}\right)}{2\pi L_{tube}k} \times (contact\%)\right] + R_c$$

$$R_c = \frac{0.565H_{mic}\frac{s_r}{s_s}}{k_s P A_a}$$

$$P = \frac{(5kg)(9.81)}{(5m\times0.002m)} = 4905\frac{N}{m^2}$$

$$R_{total2} = \frac{1}{768.6\pi(0.002m)(5m)(0.27)} + \left(\frac{\ln \frac{0.00115}{0.001}}{2\pi(0.42)(5m)(0.27)} \right) + \frac{0.565(0.13\times10^{9})\left(\frac{1.92\times10^{-6}}{0.24}\right)}{(0.321)(4905Pa)(5m)(0.002)}$$

$$R_{total2} = 0.1534 + 0.0392 + 37.32$$

$$R_{total2} = 37.513\frac{K}{W}$$

To find the overall resistance, R_{total1} and R_{total2} are calculated as resistors in parallel.

$$R_{overall} = \frac{R_{total1}R_{total2}}{R_{total1} + R_{total2}} = \frac{(3.441)(37.513)}{3.441 + 37.513}$$

$$R_{overall} = 3.152\frac{K}{W}$$

Solving for the change in temperature between the surface and fluid,

$$\dot{q} = \frac{T_s - T_{inlet}}{R_{overall}} = 2.75W$$

$$(T_s - T_{inlet}) = \left(2.75W\right)\left(3.152\frac{K}{W}\right) = 8.67K$$

Adding the ΔT between the core and surface and the ΔT between the surface and fluid yields an overall change in temperature of

$$(T_{core} - T_S) + (T_s - T_{inlet}) = 4.53 + 8.67$$

$$(T_{core} - T_{inlet}) = 13.2K$$

Thus, the contact resistance dominates the overall resistance in the system. By applying 10 times the amount of force, the contact resistance can be lowered, in turn decreasing the overall temperature difference.

Increasing the applied force

To change the applied force, the pressure in the contact resistance needs to be increased. Assume the mass on the tube is changed from 5kg to 50kg. This represents about a stack of 10 cells. Recalculating with the new mass, the results are as follows.

$$P = \frac{(50kg)(9.81)}{(5m \times 0.002m)} = 49050 \frac{N}{m^2}$$

$$R_{total2} = \frac{1}{768.6\pi(0.002m)(5m)(0.27)} + \left(\frac{\ln \frac{0.00115}{0.001}}{2\pi(0.42)(5m)(0.27)} \right) + \frac{0.565(0.13 \times 10^9)\left(\frac{1.92 \times 10^{-6}}{0.24} \right)}{(0.321)(49050Pa)(5m)(0.002)}$$

$$R_{total2} = 0.1534 + 0.0392 + 3.73$$

$$R_{total2} = 3.92 \frac{K}{W}$$

$$R_{overall} = \frac{R_{total1} R_{total2}}{R_{total1} + R_{total2}} = \frac{(3.441)(3.92)}{3.441 + 3.92}$$

$$R_{overall} = 1.83 \frac{K}{W}$$

$$\dot{q} = \frac{T_s - T_{inlet}}{R_{overall}} = 2.75W$$

$$(T_s - T_{inlet}) = (2.75W)\left(1.83 \frac{K}{W}\right) = 5.05K$$

$$(T_{core} - T_S) + (T_s - T_{inlet}) = 4.53 + 5.05$$

$$(T_{core} - T_{inlet}) = 9.6K$$

If thermal paste is introduced between the surface of the cell and tube, this means that the contact resistance becomes a conduction resistance. If the film thickness is assumed to be 70μm and the conductivity of the thermal paste is 4 W/mK, the change in overall temperature is outlined below using 50kg of mass.

Surface area covered by thermal paste

$$S.A. = \pi(contact\%)D \times L$$
$$S.A. = \pi(0.27)(0.002m)(5m)0.00848m^2$$

R_c in R_{total2} is replaced with R_{tp} (thermal paste resistance).

$$R_{tp} = \frac{\delta_{tp}}{k_{tp}A}$$
$$R_{tp} = \frac{70\times10^{-6}m}{4\times0.00848} = 0.00206\frac{K}{W}$$

Therefore, the new R_{total2} and R_{total} is

$$R_{total2} = 0.1534 + 0.0392 + 0.00206$$
$$R_{total2} = 0.195\frac{K}{W}$$
$$R_{overall} = \frac{R_{total1}R_{total2}}{R_{total1} + R_{total2}} = \frac{(3.441)(0.195)}{3.441 + 0.195}$$
$$R_{overall} = 0.998\frac{K}{W}$$

The overall temperature change with thermal paste is equal to

$$(T_{core} - T_{inlet}) = (2.75W)\left(0.998\frac{K}{W}\right) + 4.53 = 7.3K$$